

Syracuse University

SURFACE

Dissertations - ALL

SURFACE

August 2018

Rheology and Collective Behavior in Living Tissue

Michael David Czajkowski
Syracuse University

Follow this and additional works at: <https://surface.syr.edu/etd>



Part of the [Physical Sciences and Mathematics Commons](#)

Recommended Citation

Czajkowski, Michael David, "Rheology and Collective Behavior in Living Tissue" (2018). *Dissertations - ALL*. 914.

<https://surface.syr.edu/etd/914>

This Dissertation is brought to you for free and open access by the SURFACE at SURFACE. It has been accepted for inclusion in Dissertations - ALL by an authorized administrator of SURFACE. For more information, please contact surface@syr.edu.

Abstract

Recent experiments and simulations have indicated that confluent epithelial layers, where there are no gaps or overlaps between the cells, can transition from a soft fluid-like state to a solid-like state, with dynamics that share many features with glass transitions. While a coherent picture has begun to form connecting the microscopic mechanisms that drive this transition with macroscopic observables, much less is known of its consequences in biological processes. Do tissues tune themselves to a fluid state in order to promote collective motion? Has evolution made use of the ability of tissues to tune themselves between fluid and solid states in programming the complex steps leading from the embryo to the organism? Here we describe our recent efforts to answer such questions using continuum and mesoscopic models. Employing the biophysical vertex model, active cells in confluent tissue are described as polygons with shape-based energies. Recent work has shown that this class of models yields a solid-liquid transition of tissue with evidence of glassy dynamics near the transition line. Here, we extend one such model to include the influence of cell division and cell death. With careful numerical studies, we refute a recent claim that the presence of such division and death will always fluidify the tissue. In the second part of the thesis, we develop a novel hydrodynamic model of confluent motile tissues that couples a structural order parameter for tissue rigidity to cell polarization. Using this continuum model we identify a new mechanism for pattern formation in confluent tissues via rigidity sensing that we name “morphotaxis”. We find that a single “morphotactic” parameter controls whether a tissue will remain homogeneous or will develop patterns such as asters and bands.

Rheology and Collective Behavior in Living Tissue

by

Michael D. Czajkowski

B.A., SUNY Geneseo, 2011

Dissertation

Submitted in partial fulfillment of the requirements for the degree of
Doctor of Philosophy in Physics.

Syracuse University
August 2018

Copyright © Michael D. Czajkowski 2018

All Rights Reserved

Acknowledgements

I would like to thank my advisors for introducing me to the richness and the endless possibilities of soft matter physics, for educating me in countless ways and for supporting this wonderful community. Without you none of this would be possible. I would also like to thank my parents for providing a neverending source of love and support and my friends for thinking with me along the way. I hope I am able to return the favor.

Contents

1	Introduction	1
1.1	Motivation	1
1.1.1	Dense Tissues	2
1.2	Active Matter	3
1.2.1	Polar Active Particles	4
1.2.2	Active Hydrodynamics for the Vicsek Model	7
1.2.3	Apolar and Isotropic Active Forces	10
1.3	Dense Biological Tissues	12
1.3.1	Epithelial Tissues and the Vertex Model	13
2	The Active Vertex Model	19
2.1	Introduction	19
2.2	The Vertex Model with Motility	20
2.3	Rheological States of the Model	26
3	Glassy States in Confluent Tissues with Mitosis and Apoptosis	30
3.1	Tissue Simulations with Cell Division and Cell Death	32
3.1.1	Simulation of mitosis and apoptosis events	33
3.2	Tissue rheology in the presence of mitosis and apoptosis	35
3.3	Simple null model for interaction between τ_δ and $\tau_{\alpha 0}$	36
3.4	Flow and fluidization from individual mitosis and apoptosis events	38

3.4.1	Toy Models for Cell Displacements	39
3.4.2	Single event data guides a scaling collapse	43
4	Continuum Modeling of Tissues	45
4.1	A mean-field model for 2D shape anisotropy	50
4.1.1	The Shape Tensor	51
4.1.2	Mean-field theory	52
4.2	Hydrodynamic theory of cellular shape	54
4.2.1	Hydrodynamics of Shape in Non-Motile Tissues	57
4.2.2	Hydrodynamics of Shape in Motile Tissues	58
4.2.3	Homogeneous Steady States	61
4.2.4	Simplified 1d Model	62
4.2.5	Linear Stability Analysis	63
4.2.6	Numerical simulations	67
5	Discussion	70
A	Appendices	76
A.1	Anisotropic Perturbation of the Shape Tensor	76
A.2	Linear Stability Analysis	79
A.2.1	Stability of stationary (non-polarized) states	80
A.2.2	Stability of Stationary Solid	81
A.2.3	Stability of Stationary Fluid	83
A.2.4	Stability of Flocking Fluid	84
	Bibliography	87
	Vitae	107

List of Figures

1.1	Depiction of the fundamental ingredients for the formation of a flock. On the left, a self-propelled item may sense and interact with the direction of motion of its neighbors. At high enough density and low enough noise, this behavior may lead to spontaneous emergence of collective motion as depicted in the publication of Vicsek <i>et. al.</i> [147] (Center). This may explain the onset of “gregarious” behavior in locusts [23] (Right) as well as other flocking organisms. Locust photo adapted from the work of Ariel <i>et. al.</i> [3]	6
1.2	Illustration of the Vertex Model reduction of a 3-dimensional epithelial tissue cells to a simple 2-dimensional representation of cells as polygons which tile space.	14
1.3	Diagram of neighbor exchange during a T1-Transition in the Vertex Model .	15
2.1	Illustration of the vectors and geometric components involved in evaluating the forces on vertex μ due to the shape energy and the motility of cell a . . .	23
2.2	A T1 topological rearrangement in our AVM simulations identifies an edge with length $l_0 < l_c$, rewires the network connections appropriately, rotates by $\pi/2$, and extends the edge length to a factor λ times its original length. . . .	25

2.3	Quantification of phase behavior in the Active Vertex Model (AVM) with $D_r = 1$ and $N_{cells} = 300$. In (b), the timescale $\tau_{\alpha 0}$ of the decay of the overlap function grows beyond the length of simulations as the vertex model tuning parameter s_0 is decreased while $v_0 = 0.05$ is held fixed. In (b), the mean square displacement of cell centers for the same phase points indicates this increasing timescale is associated with subdiffusive caging behavior. In (c), $\tau_{\alpha 0}$ is shown on a logarithmic colorscale for a representative set of points in the $s_0 - v_0$ plane. Black stars indicate phase points where $\tau_{\alpha 0}$ is too long to be resolved with our data. The inset shows the implementation of motile forces prescribed by Eq. (2.7).	27
2.4	Colormap of phase behavior quantified with the normalized effective diffusion. Black stars indicate points where $\frac{D_{eff}}{D_0} < 10^{-3}$. The red line shows the boundary of the region where $q > 3.82$, which indicates a connection between sub-diffusive behavior and cell shape similar to that seen in the SPV.	28
3.1	The process for a single mitosis event in our model is shown sequentially in (a-c). Starting again with the initial cell in (a), the model steps for apoptosis are shown sequentially in (d-f).	34
3.2	Rheological measures of tissues with mitosis and apoptosis for $v_0 = 0.05$ and $D_r = 1$. In (a), the measured overlap decay τ_α as a function of s_0 and the cell cycling rate k_δ is displayed as a colormap, indicating generically that k_δ tends to fluidize the tissue. In (b) and (c), mean square displacement and overlap curves are plotted for constant $s_0 = 3.83$ over a series of k_δ and show that the dynamics approach the expected values from the “bare” AVM at small enough k_δ . In (d) and (e) are a similar series of curves for a constant $k_\delta = 1.6e - 5$ over a series of s_0 values. Here, the approach towards a universal behavior (expected at the lowest values of s_0) only becomes clear at long times.	37

3.3	<p>Affine and non-affine displacements quantified in response to a single mitosis/apoptosis event for $N_{cells} = 5000$. In (a) and (b), arrows show the affine displacements in response to a mitosis and apoptosis, respectively, for a tissue with $s_0 = 3.6$, $v_0 = 0.05$. Colormap indicates the magnitude of these affine vectors with grid spacing 1.5. In (c), the magnitude of affine displacements averaged over angles is plotted as a function of distance from a mitosis event. The purple dot-dashed line shows the agreement with the expected scaling of $1/r$ for a series of s_0 values. In (d), the values for the $\delta u_{(m,a)}(r)$ per Eq. 3.10 are plotted similarly, revealing a finite region of non-affine displacements. The inset in (d) shows the same non-affine data without the long distance behavior removed, showing a plateau to a finite value.</p>	40
3.4	<p>In (a) data for τ_α vs. τ_δ for a series of $\tau_{\alpha 0}$ does not collapse with simple rescaling using $\tau_{\alpha 0}$. In (b), the same data comes closer to collapse by additionally normalizing τ_δ using an averaged scale of motion ($C_2(\tau_{\alpha 0})$) extracted from single event apoptosis and mitosis data. Dotted lines represent the same data plotted for a constant C_2. A universal curve for the crossover between mitosis/apoptosis dominated behavior and motility-dominated behavior is suggested.</p>	43
4.1	<p>Diagrams illustrating various shape-related behaviors in epithelial tissues. a From left to right: isotropic cell shapes (solid/jammed state), anisotropic cell shapes (fluid), nematic order of anisotropic cell shapes. b and c together display the <i>morphotaxis</i> properties of the tissue. b: Cells may sense local gradients in shape, corresponding to gradients in tissue rigidity, and thereby polarize and migrate towards (left) or away from (right) the more anisotropic cells. c: Sinks of polarized motile forces may induce an increase (left) or a decrease (right) in the local cell anisotropy.</p>	48

4.2	Schematic phase diagram comparing negative (left) and positive(right) <i>morphotaxis</i> parameters for a shape-based hydrodynamic model where convergent polarization tends to decrease local cell shape anisotropy. The “target shape” axis captures the average cell’s preferred perimeter to area ratio, while the “shape-driven flocking” axis quantifies the degree to which elongated cell shapes promote polarization. The left panel corresponds to tissues in which cells tend to migrate toward fluid-like regions with more shape anisotropy, and the behavior is largely homogeneous. The right panel describes tissues where cells polarize toward solid-like regions of tissue with lower shape anisotropy, and the tissue exhibits patterns like asters or bands in a large region of the phase space.	49
4.3	Left: The Vertex Model representation of cells in a confluent monolayer. Right: The vectors which are used to create the cellular shape tensor.	51
4.4	Mean-Field tissue energy as a function of shape-anisotropy for various values of the target shape-index s_0 . As this shape index is increased past $s_0^* \approx 3.81$ the energy develops two minima and the anisotropy \bar{m} becomes finite, as shown in the inset.	54

4.5	Phase diagrams and simulation results in the $s_0 - a$ plane. As in the legend, blue circles represent simulations in which the fields relax to their homogeneous steady state solution. Orange squares represent simulations in which patterns are found to emerge. Here we compare the cases $\nu = -1$ (Top-Left) and $\nu = 1$ (Top-Right) to show the qualitative change induced by this plithotactic parameter. Bottom: Snapshots of different types of emergent patterns from tissue simulations. Colorbars represent the magnitude of local anisotropy (m) while red arrows represent local cell polarization (\mathbf{p}). (A): Sparse aster-like islands of anisotropic cells emerge near the onset of instability in the solid phase. (B): shows an example of “solid” islands arising in the flocking fluid phase due to a splay instability and preventing collective motion. (C) shows the elongated structures resultant from banding instability for $\nu = 1$ while (D) shows the qualitatively different band structures for $\nu = -1$	69
A.1	The mean value \bar{m} of the order-parameter obtained by minimizing the single-cell free energy derived using different geometric perturbations of the energy of a regular pentagon.	77
A.2	Dispersion relation of the eigenvalue $z_+^{solid}(k)$ in the stationary solid phase as a function of k . Lines correspond to points in the $\nu = 1$ phase diagram from Fig.4.5. The blue curve then corresponds to a stable homogeneous state, while yellow and green represent unstable states.	82

Chapter 1

Introduction

1.1 Motivation

Quantifying cell dynamics is crucial in both understanding and manipulating biological processes. In dense tissues, it is often useful to think of the tissue as a “living material” and interactions between cells, such as steric repulsion and reorientation can give rise to interesting macroscopic behaviors, such as coordinated cell migration. Interestingly, a comprehensive theory of tissue rheology (e.g., whether a group of cells will behave like an elastic solid or like a fluid) is lacking. Such a theory would provide a deeper understanding of morphogenetic processes, cancer metastasis, wound healing, and more. These biological phenomena may have non-trivial dependence on time-scales, internal mechanical properties, and “activity” [28, 16, 101].

The idea that rheology and force play roles in the development and maintenance of organisms is far from new [139]. Related questions of the biological importance of crowding [80, 1], manipulation with optical force [135], and the precise role of force in development [64, 83] have been under investigation over the past century, to the tune of numerous great successes. More recently, the field of “Active Matter” has emerged within statistical physics to provide new insight into biological processes. This new field has grown out of the observation that

varieties of living and driven matter consume energy and thereby obey a different set of basic symmetries and principles. Guided by this insight, it is possible that future investigations may find application in materials science and drug delivery.

More recent biological manipulation techniques have been employed to isolate the effect of tissue boundaries [101, 110, 66], probe spatially dependent forces and rheology [38, 119, 65], and may even allow highly sensitive spatiotemporal activation of motility, contractility, proliferation, and apoptosis [48, 142]. These have been developed in tandem with the growing world of experimental imaging methods such as Particle Image Velocimetry (PIV) [100], Traction Force Microscopy (TFM) [130], FRET [99, 118, 141, 159], light-sheet microscopy [71, 56, 148] and many more [92, 50, 151]. These have permitted new insight into the complex interplay between internal cellular functions and tissue dynamics. While helping to constrain theory and simulations, these insights also open up new realms for exploration in tissue mechanics.

1.1.1 Dense Tissues

A substantial fraction of cell types form dense, confluent tissues. One important example is the epithelial layer. In these tissues, which are typically one to a few cell layers in thickness, each cell is tightly adherent to its neighbors forming a network of cell-cell interfaces. Although the cell nucleus and other structures can contribute to the mechanical properties of cells, in many epithelial layers it seems that the mechanical properties are well-approximated by the network of interfaces. This self-regulated network may produce non-trivial rheological properties as revealed by experiments over the past decade [36, 2, 49, 11]. Among the observed phenomena is the transition to a “glassy” state in which cells become caged by their neighbors [112, 2]. However, unlike conventional glasses, cells within tissues may generate additional dynamics such as directed motile forces and cell division. How might these biological effects influence mechanical tissue properties such as glassiness? How might tissue rigidity then feed back and guide the biological processes? This is the focus of our work.

1.2 Active Matter

“Active Matter” describes a set of materials in which the individual agents convert free energy into kinetic motions and stresses. This motion is typically generated at the scale of a single agent. Agents may be grouped into two categories based on the process which generates the motion: synthetic and biological. For the broad zoo of synthetic active matter agents such as Janus particles, camphor rafts and magnetic rollers [90, 32, 98, 54, 91, 22, 153] the driving process is relatively simple, idealized, and reliable. However, for biological agents such as a flying bird, swimming sperm or a crawling cell, motion is typically driven by an internal metabolic process. This metabolism, and the conversion of the internal energy into motion is typically regulated by a large number of internal biological factors. To describe this active process with complete resolution would require an impossibly large number of variables. Just as in the case of a molecular gas, such a complete description is neither feasible nor productive. Instead, one typically constructs a simplified effective model. In the case of active matter, this comes as an effective “active force” acting on the i -th constituent. The equation of motion for the position of the i -th unit located at position $\mathbf{r}_i(t)$ then takes the form

$$m\ddot{\mathbf{r}}_i = \mathbf{F}_i^{fric} + \mathbf{F}_i^{act} + \mathbf{F}_i^{int} + \mathbf{F}_i^{noise}, \quad (1.1)$$

where \mathbf{F}_i^{fric} is a dissipative force that comes from frictional interactions with a substrate or the environment, \mathbf{F}_i^{int} may come from mechanical interactions with other system constituents, and \mathbf{F}_i^{noise} arises from fluctuations (e.g., thermal forces). The active force \mathbf{F}_i^{act} represents an explicitly out-of-equilibrium driving force, such as cells exerting traction forces on a substrate to move. In this way, the complex process which produces motion (e.g. how a bird flies) is grouped into a small number of parameters and we focus instead on the properties of the group (e.g. the collective dynamics of the flock). Just as in standard statistical mechanics, Eq. (1.1) is considered a “microscopic model” as it describes the motion of individual system “particles”. The defining microscopic parameters of this *effective* model are

assumed, case by case, to take a form which is reasonable in the appropriate limits (e.g. colloidal matter displaying Brownian motion in the absence of interactions). As Eq. (1.1) typically preserves neither energy conservation nor momentum conservation, it is one of the pivotal observations of active matter that this lack of microscopic symmetry can control which macroscopic states may be expected. In the following we both review types of active forces and methods for understanding their influence on macroscopic system properties.

1.2.1 Polar Active Particles

Equation (1.1) above, is an example of the form that Newton’s second law might take for an active “agent” or particle within a particle-based model. The first, and in some senses the simplest particle-based model was developed by Craig Reynolds [108] for animated films. This same model was later analyzed in-depth for phase behavior by Vicsek *et. al.* [147]. The Vicsek model of microscopic flocking consists of idealized “boids” which are prescribed to move at a fixed speed. Boid is a shortened term for “bird-oid” that was introduced by Reynolds [108] to describe bird-like active agents. It was by considering the possibility that these velocity *directions* might interact that Vicsek *et. al.* were able to observe and quantify the basic ingredients required for the formation of a flock. While informative and foundational, the Vicsek model treated time as discrete and the process of alignment as instantaneous. We therefore present here a more general continuous-time version of the model which includes all the same ingredients as the original Vicsek model and is reflective of the contemporary modes of study and simulation.

Vicsek: Activity and Alignment In the Vicsek model (and many other contemporary models) activity comes in the form of a *propulsive* force of constant magnitude f_0 . In the overdamped limit of motion, where friction with the substrate dominates, the active particles will have a fixed speed $v_0 = f_0/\gamma$ where γ is the coefficient of friction. The motion of the

i -th agent with position \mathbf{r}_i is then follows the equation of motion

$$\partial_t \mathbf{r}_i = v_0 \hat{n}(\theta_i). \quad (1.2)$$

Here, θ_i is an angle defining the orientation of self propulsion, and $\hat{n}(\theta_i)$ is a unit vector in this direction. In this and a large fraction of active matter models, it is this direction of motion θ_i that is the free dynamical variable of interest. This angle evolves in time with the following equation of motion:

$$\dot{\theta}_i = \frac{\phi_i - \theta_i}{\tau_a} + \eta_i(t), \quad (1.3)$$

which includes an interaction whereby agents will update their propulsion over a timescale τ_a to align with a locally defined direction (angle) ϕ_i . This angle is traditionally taken to be the average direction of motion in the neighborhood of particle i . This average can be defined geometrically (e.g. by a cutoff distance) or topologically (e.g. by a Voronoi tessellation).

The second term corresponds to a rotational noise, which captures fluctuations in the angle of polarization. This noise reflects any process that causes the agent orientation to fluctuate. In the simplest and most common form, the noise is assumed to be white and gaussian and it is defined by

$$\langle \eta_i(t) \rangle = 0, \quad \langle \eta_i(t) \eta_j(t') \rangle = 2D_r \delta_{ij} \delta(t - t'), \quad (1.4)$$

where D_r is the rotational diffusion rate. To be a bit more precise, D_r is half of the variance of this noise distribution.

Vicsek: Flocking We now note that this noise term helps to define a timescale which may be defined as $\tau_r \equiv 1/D_r$. This timescale is in competition with the timescale of alignment τ_a to determine the qualitative behavior of the system. For small τ_r noise disrupts the velocity quickly compared to the alignment and system agents are disordered, propelling themselves in random directions. However, as τ_r is increased the system undergoes a transition to a



Figure 1.1: Depiction of the fundamental ingredients for the formation of a flock. On the left, a self-propelled item may sense and interact with the direction of motion of its neighbors. At high enough density and low enough noise, this behavior may lead to spontaneous emergence of collective motion as depicted in the publication of Vicsek *et. al.* [147] (Center). This may explain the onset of “gregarious” behavior in locusts [23] (Right) as well as other flocking organisms. Locust photo adapted from the work of Ariel *et. al.* [3]

flocking state where all the agents have coordinated their propulsive forces to travel in a common direction. This transition can be quantified by an order parameter

$$P = \left| \frac{1}{N} \sum_i^N \hat{n}(\theta_i) \right|, \quad (1.5)$$

which is zero when the propulsion directions are disordered (isotropic) and non-zero when these orientations become aligned (polar flock).

At first glance one might expect that the important features of flocking are determined simply by the timescales τ_a and τ_r . However, these timescales can only give a complete picture of flocking behavior for active agents which may align with their neighbors over arbitrary distances. Such a “topological” model of flocking is appropriate for some particular scenarios such as starling flocks [5] and confluent tissues, where interactions appear to depend on the number of neighbors regardless of the geometric distance. In other systems, such as the swarming of locusts [23], metric distance plays a role along with τ_a and τ_r in determining the flocking behavior. The original Vicsek Model included the simplest version of such an

effect, as shown in the left side of Fig. 1.1, whereby agents will only align if they are within some radius of one another. Simulations of this model can numerically confirm the intuition that higher density is required for flocking to arise, and that at these high densities the behavior is indeed determined by a competition between the timescales τ_a and τ_r . A deeper quantitative understanding is gained through coarse graining, as described in section 1.2.2.

Note also that our discussion of the Vicsek model thus far has not considered the influence of mechanical contact interactions. In flocking scenarios in the animal kingdom, this is often reasonable. For systems of birds, wildebeest and fish, flocking has more to do with information travel via sensory perception than with actual physical forcing. The timescale τ_a in these cases is then dependent on the vision and reflexes of the animal. The direction of the propulsive force then need not be distinguished from the direction of actual motion. For instance, it is unlikely to observe a wildebeest traveling along with a stampede while turned sideways. However, this argument does not extend to the scale of cellular matter where cells have been observed exerting persistent crawling forces perpendicular to their actual motion [66]. At this scale, direct physical contact and forces between the cells are expected to play a strong role in determining the system behavior.

Simulations of active matter with mechanical interactions have been studied in many contexts. At low noise and zero alignment, a clustering phenomena termed “motility-induced phase separation” may be observed [137, 39, 19, 96], while at strong alignment flocking is observed to compete with jamming to determine system behavior [52, 44]. In such regimes, coarse-graining is generally unfeasable and analytic results connecting microscopic parameters to macroscopic observables have progressed slowly, due in large part to the inherent complexity and non-linearities of high-density matter.

1.2.2 Active Hydrodynamics for the Vicsek Model

Just as in the case of traditional condensed matter physics, we do not always desire to keep track of all these microscopic (agent) degrees of freedom. In analyzing the statistical

behavior of large active systems, hydrodynamic equations become useful. Macroscopic properties of concern may be gleaned far more easily from such equations, when they exist. In fact, the first analysis of large-flock statistics consisted of a hydrodynamic analysis [144]. This work ignited much of the active-matter research in the past 20 years. Aside from the countless applications in biology, these models exhibit the special quality of allowing spontaneous breaking of a continuous symmetry in two dimensions. A “flocked” state, with microscopic constituents agreeing on a non-zero average velocity, requires these constituents to choose this motion direction. This type of symmetry-breaking was previously considered forbidden in two and fewer dimensions by the Mermin-Wagner theorem [86]. The inherently non-equilibrium nature of the system breaks this restriction. This active movement of constituents allows for faster dissipation of fluctuations emerging from noise, thereby stabilizing the broken-symmetry state. While the initial analysis of Vicsek suggested that the transition to a flocking state is continuous, a more careful later analysis revealed the transition to be discontinuous [47]. Analytic explorations will therefore carry the additional complications associated with first-order transitions.

Coarse-Graining Approach

In order to construct the relevant hydrodynamic equations of interest, one might imagine beginning with analysis of the microscopic model. In many cases, the methods of conventional statistical physics may be employed to “coarse-grain” the model. This method produces equations for the long-wavelength dynamics of some number of relevant fields. In the case of flocking, the minimal field of concern is an averaged velocity \vec{v} analogous to the Navier-Stokes equation in classical fluids. This velocity may be coupled to additional fields (i.e. density, synchronization etc.) for more complex dynamical models. This approach is advantageous because the continuum equations are expressed in terms of the microscopic parameters, which lends insight for experimental manipulation.

In these active systems, the typical coarse-graining method starts with either a Smolu-

chowski, Fokker-Planck, or Boltzmann equation to describe the evolution of microscopic probability densities [15, 74, 10, 156]. Additional assumptions of molecular chaos and closure then allow isolation of the long-distance, slow dynamics which are expected to dominate at the macroscopic level. Employing these methods, Bertin *et. al.* [15] were able to verify the qualitative conclusions of the Vicsek model. This molecular chaos assumption is typically only valid in dilute (low-density) systems, resulting in the complications when trying to coarse grain medium- and high-density dynamics. These complications arise similarly in high density inactive matter. In these regimes, researchers turn to alternative methods.

Phenomenological Approach

In many cases, hydrodynamic equations may be written down on the basis of symmetry and conservation laws instead of derived through coarse graining. In the simplest case, this process allows one to consider the first time derivative of a field, and relate this to all possible terms allowed by the symmetry of the problem. Of course, there are infinite terms allowed, and it is the assumption that long-wavelength dynamics will control system behavior which allows an expansion in gradients to be truncated. This method is employed by Toner and Tu [144] in their initial analysis of flocking hydrodynamics. In this classic formulation, the local number density obeys the simple conservation law

$$\partial_t \rho = -\nabla \cdot (\rho \mathbf{v}), \quad (1.6)$$

while the collective velocity \mathbf{v} is found to obey a generalization of the Navier-Stokes equation

$$\begin{aligned} \partial_t \mathbf{v} + \lambda_1 (\mathbf{v} \cdot \nabla) \mathbf{v} + \lambda_2 (\nabla \cdot \mathbf{v}) \mathbf{v} + \lambda_3 \nabla v^2 \\ = -\alpha \mathbf{v} - \beta v^2 \mathbf{v} - \nabla P + D_B \nabla (\nabla \cdot \mathbf{v}) + D_T \nabla^2 \mathbf{v} + D_2 (\mathbf{v} \cdot \nabla)^2 \mathbf{v} + \mathbf{f}. \end{aligned} \quad (1.7)$$

This model includes the handicap that each coefficient is generally an unknown function of $(\rho, |\mathbf{v}|)$. Despite this, a stability analysis may be performed which indicates the existence

of a stable, flocked state. Although there is no direct connection between microscopic and macroscopic parameters, this method is not restricted by assumptions of low-density. Results from coarse graining efforts have shown that α may be approximated as a linear function of density near the transition. This is an important feature of the model as the transition to a flocked state may then be *density-driven*. A simple analysis of homogeneous, steady-state solutions shows the emergence of a non-zero vector field $v_0^2 = \alpha/\beta$ as α changes sign. For a flocking model, this is a reasonable feature. That increasing the density leads to more alignment, and thus to the emergence of flocking, is expected microscopically. In this case the density takes the role of a tuning parameter, and the transition to a flocked state may be achieved by increasing this density past a critical value ρ^* .

1.2.3 Apolar and Isotropic Active Forces

Activity at the local level is generally produced by a force dipole. Thus far we have considered systems where the dipole is produced by virtue of direct mechanical interaction with a substrate (e.g., the surface which cells may crawl *across*). In many cases the substrate will quickly dissipate the extra energy from these active forces, and can therefore be ignored. In these cases, only half of this force dipole is considered, which then takes the form of a directed propulsion. However, for a large class of active matter systems, the entire active dipole must be considered. For many of these active systems, the force dipole arises from agent-agent interactions rather than agent-substrate interactions. In these cases, rather than producing a directed polar motion, local energy consumption produces an active stress. We briefly review some characteristic examples of this which are important in understanding the dynamics of biological tissues.

At the subcellular scale, mechanics are governed largely by the dynamics of semiflexible polymer proteins called actin [149]. This network of proteins experiences local forces due to the influence of a molecular “motor” called myosin [140, 67]. In place of directed migration, this local active stress serves to produce local contractions and extensions of the

protein scaffold. Similar behavior is found for the effect of kinesin motors on assemblies of microtubules [150, 113], another cytoskeletal ingredient which plays a key role in cell division and has become another workhorse for active matter investigations. Questions of how these microscopic forces lead to e.g. macroscopic Actomyosin contractility [73] as well as what separates extensile from contractile behavior in microtubules [40] are still under investigation.

Even at the tissue scale, the contractile effects of myosin may play a role in rearrangements and organization of cells. Here, the key ingredients of tissue remodeling are contained in T1 transitions, as depicted in Fig. 1.3 and explained in more depth in section 1.3.1. These transitions [106, 12], and general morphogenetic processes [61, 129] may be controlled by the regulated activity of myosin motors clustered along the cell-cell interfaces. The myosins contract the actin network which is mechanically coupled to the cell wall, thereby producing an interfacial tension. These tensions may then actively produce t1 transitions which directly influence tissue structure and may even render it fluid [70].

Within this category of apolar active matter, another ubiquitous source of activity comes from proliferation and death in living cultures. These effects of the cell cycle are expected, by many predictions, to render previously rigid biological tissues and cell aggregates effectively fluidized [105, 81, 76]. This is rather intuitive in the limit of fast cell cycling, as the constant adding and removing of cell material must eventually produce motion. These stochastic events have been predicted [109] and experimentally shown [60] to play the role of a temperature in bacterial biofilms. That is, the fluctuations in the height of the biofilm are controlled by the rates of the cell lifecycles in a manner reminiscent of equilibrium thermal matter. It is worth noting that such a comparison with thermal matter is not generic to active matter systems, and at times is explicitly forbidden [124].

1.3 Dense Biological Tissues

Developed organisms may be viewed as highly coordinated assemblies of specialized cells and extracellular materials. A large fraction of these cells exist in regions of high number density. In many tissues with little extracellular matrix, cells are in close mechanical contact with their neighbors and thereby their boundaries form a sustained network structure. These mechanical networks may display order, as in the case of both striated and smooth muscle, the cornea, and the developed fly wing [38, 72], or disorder as in the cases of skin and bone and vasculature. It is therefore not surprising that soft matter physicists have become increasingly interested in understanding phase transitions and rheology in these biological materials. Indeed, the animal and plant kingdoms would seem to then provide an endless variety of tissues for systematic study.

However, physicists who have ventured into the study of biological tissues thus far have focused much of their attention on the dynamical processes of development. Fully developed animal species do not start out their life cycle resembling the finished product. The vast majority will divide from a single cell into a ball of cells which are in many ways indistinguishable from one another. It is the process of *morphogenesis* which specializes and positions these cells to begin functioning as an organism. Such a process generically comes in numerous stages, each of which require tremendous coordination between different spatial regions. How then does this ball of cells undergo this morphogenetic process so robustly? How is it possible that mistakes and variances along the way lead chiefly to variations in appearance rather than catastrophic failure? Much of this question is addressed by studies in chemical dynamics of morphogens. Morphogens are signaling molecules which cells may produce to both prompt and self-regulate these developmental processes. As noted first by Turing's reaction-diffusion model [146, 68], such self-regulation of chemical concentrations may lead to the formation of highly reproducible patterns. Naturally, the robust emergent length scales produced by these dynamics may therefore be the root of success in developmental processes.

While the above picture may seem sufficient to explain some of the robustness of development, there are many processes of invagination and migration [36, 77, 88, 53, 63] which appear mechanical in nature. It is entirely possible for morphogens to regulate and produce mechanical force via e.g. myosin phosphorylation [61]. Much of the recent work in developmental biophysics has produced many examples where these self-generated forces form a necessary ingredient towards building the organism [36, 88, 84, 61, 77]. Despite these insights, the field is far from a full picture of when and where such forces are programmed, and what role is played by mechanics along the way. After all, tissues are complex materials, and the dynamic response to an internally produced force depends on the mechanical properties of said material. To develop a more complete understanding of development may not only lead to a better understanding of biology, but may also naturally lead to advancements in the field of self-assembly.

1.3.1 Epithelial Tissues and the Vertex Model

Along the detailed process of development, quasi two-dimensional sheets of cells form. Typically one or a few cell diameters in thickness, these tissues will rearrange, invaginate, and morph, eventually forming the surfaces of organs and separating functions within the organism. These epithelial sheets have therefore become a central topic of investigation in the morphogenetic community.

In the plane of an epithelial monolayer, the geometry of the close-packing of cells largely determines the mechanical interactions between them. Using intermembrane proteins such as the variety of cadherins, cells adhere tightly to their neighbors, effectively forming a single shared cell-cell interface. Within the cell, these interfaces are coupled to a complex network of semiflexible polymers and proteins called the cell cortex. As described in section 1.2.3, the combination of the polymers such as microtubules and actin with molecular motors such as myosin and kinesin produce forces in the cell. These active networks near the cell wall generically apply a tension to the cell-cell interface. While other effective forces are at play

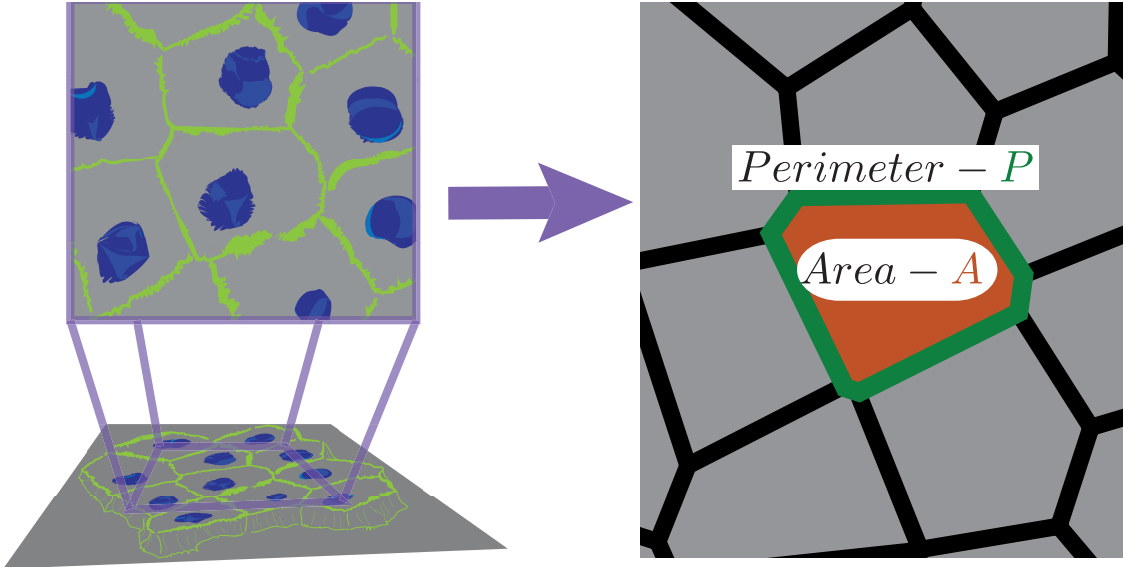


Figure 1.2: Illustration of the Vertex Model reduction of a 3-dimensional epithelial tissue cells to a simple 2-dimensional representation of cells as polygons which tile space.

in determining the fate of the network, these geometric tensions dominate the mechanics and form the basis of vertex models.

While the vertex model has been implemented in many distinct ways, each assumes that the dominant mechanical energies experienced by a cell are determined by the geometry of the network of cell boundaries. In these models, cells in quasi 2-d monolayers are reduced to polyhedra. These polyhedra are described by a height h perpendicular to the monolayer and by polygonal tiles in the plane of the monolayer, each described by an area A and perimeter P . In our model, and many other current models in the field, the energy of the a -th cell is then defined via

$$E_a = \kappa_A(A_a - A_0)^2 + \kappa_P(P_a - P_0)^2, \quad (1.8)$$

or equivalently

$$E_a = \kappa_A(h_a - h_0)^2 + \kappa_P P_a^2 - 2\kappa_P P_0 P_a + E_0. \quad (1.9)$$

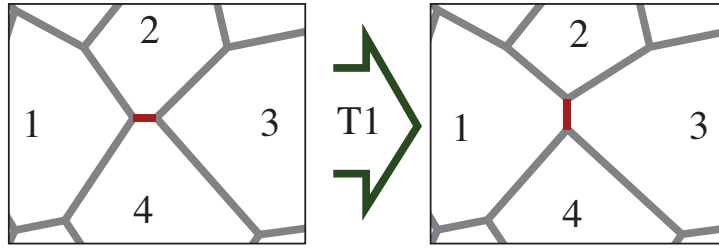


Figure 1.3: Diagram of neighbor exchange during a T1-Transition in the Vertex Model

In Eq. 1.9, the terms are expanded in a more intuitive format. The first term on the right hand side captures the resistance to height fluctuations. Assuming volume incompressibility and small height fluctuations, one can rewrite this as a quadratic term in area, as shown in Eq. 1.8. The third term in Eq. 1.9 captures the tension produced by the cortical actin network and counteracted by cell-cell adhesive molecules. The second term is quadratic in P_a , and has at least two possible origins. One possibility is active elastic contractility in the acto-myosin network. A second possibility comes from the fact that cortical tension and cell adhesions each draw from a finite pool of molecules, giving rise to a restoring force at large interface lengths. The final term in Eq. 1.9 which shifts the energy with no influence on the dynamics, allows the expression to be reduced to the quadratic expression in Eq. 1.8. Note that this energy is, of course, what one would get using A, P as the relevant generalized coordinates while considering small oscillations about some preferred state. However, this term-by-term expansion adds credence to the validity of the energy as well as some intuition for how these parameters might be manipulated experimentally.

For the polygonal cells in this model, motion across finite distances is inherently topological. Any motion of cells over distances larger than the cell diameter requires changes in nearest neighbors, which are represented by the facet edges. In a tissue comprised of three-fold vertices, T1 transitions are both required and sufficient to enable migration. A T1 topological swap concerns a cluster of 4 objects and rearranges neighbors as shown in Fig.[1.3].

While many realizations of this vertex model have found great success in tissue modeling [55, 38, 126], we focus now on cell dynamics. In [17], these T1 swaps are viewed as energetic barriers to cell motion, whose statistics are then quantified. A scaling collapse of the energy barrier data reveals the existence of a jamming transition which is tuned by a dimensionless *shape-index* $s_0 = P_0/\sqrt{A_0}$ [16]. As the value of s_0 is increased beyond a special value of s_0^* , the height of T1-energy barriers (along with the tissue shear modulus) decreases to zero. Above $s_0^* \sim 3.81$, the tissue has zero effective shear modulus and may be considered fluid. Below this value, the tissue retains a finite shear modulus and is therefore jammed. Note here that we use s_0 instead of p_0 to reserve the variable p for other use later in the manuscript.

Aside from the natural biological importance of this result, a notable feature is the *density-independence* of the transition. Typical jamming transitions are tuned by a density or packing fraction of constituents. However, in this case the tuning parameter s_0 may be increased linearly via P_0 without changing the average area occupied by each cell.

While we have presented thus far a characteristic example of a vertex model, in practice a variety have been implemented. Not surprisingly, some of these variations come from modifications of the energy Eq. (1.8) and forces, while others modify the underlying degrees of freedom used to represent the cell. In the iteration described here, typically referred to as “the Vertex Model”, the cell-cell interfaces are straight lines traced between vertices. These vertices, which are then the degrees of freedom of the model, are typically shared by three cells. The voronoi model is similar [18, 133, 134, 85], except that the polygon configuration is restricted to be a voronoi tiling, and the degrees of freedom become the voronoi centers. Other notable variations include the cellular potts model [46, 59] which models space as a grid and determines which cell each grid point “belongs to” at each time step. There are also a number of phase-field models, which model each cell as a field with an intensity which interact everywhere in space [121, 120, 160].

Each of these models carries certain benefits and disadvantages. For instance the phase field model allows more detailed description of emergence of activity from the underlying

actin gel and of the diffusion of signaling molecules. However, the phase field model is more computationally expensive, making it difficult to simulate large tissues for long periods of time. The cellular Potts model can be quite quick, while sacrificing some accuracy of cell shape description. In practice, the choice of model comes with a balance of these pros and cons depending on the phenomenon of interest.

While the model may be chosen to balance convenience and accuracy, one hopes that the observed behavior will be independent of the choice. Recent work suggests this is largely, though not always, true. Merkel and collaborators [85] have found that 3D Voronoi and 2D vertex models exhibit very similar transitions. However, Sussman and Merkel [133] identified a particular 2D Voronoi model where the energy minimized states always remain rigid, displaying no evident transition. This suggests that some care must be taken when defining the degrees of freedom in these models.

Motile Tissues As noted previously, the tensions and pressures derived from the tissue geometry are not the only factors at play. Cells are additionally known to exert tractions through adhesions to their substrate and thereby propel themselves to migrate across the layer. It is then natural to wonder what happens to this rigidity transition if the cells become self-propelled objects. Such an exploration was first accomplished by Bi *et. al.* [18] using a Voronoi model for tissue. In their model, mechanical forces from the shape energy (Eq. (1.8)) and directed motile forces are applied to the Voronoi centers of the cells. Examining the mean square displacements of these cells, they find an intuitive picture where cells may break out of their cages and migrate through the tissue by either increasing their motility v_0 or increasing the effective adhesion s_0 past a special value $s_0^*(v_0)$.

The same investigation uncovered a rather surprising additional signature of this transition in the cell shape. It turns out that the measured shape index $q = \langle P/\sqrt{A} \rangle$ transitions from $q \sim 3.81$ to $q > 3.81$ at just the same point that the cells fluidize. This represents a transition to a glassy state which is quantified by a simple structural order parameter. This

is notable, as a structural order parameter generally does not exist for glass transitions [123].

These many different markers of a transition of tissues from a solid-like to a fluid-like state are inspiring. Hope is rising that these simple results may lead to better understanding of the role of mechanical interactions and control in biological functions. There has already been experimental evidence [94] that this cell shape based transition may not only control cell migration in real tissues, but that this same transition may be connected to the pathological behavior of asthma. However, real cell colonies, even *in vitro*, remain considerably more complex than the simple picture that our vertex model has constructed. For one, epithelial cells die and proliferate in a manner which is, in some cases, dependent on the strain that they experience [128]. These cell division and cell death events produce stresses and are sure to play a role in the dynamics of tissue cells [111, 114]. In addition, experiments have identified examples of collective motion arising in bulk tissues [43, 75]. While much work is underway toward the understanding of these and other varied phenomena [44, 143, 57, 21, 25, 81, 82], unanswered questions still abound.

Chapter 2

The Active Vertex Model

2.1 Introduction

Forces generated by cell motility in real epithelial tissues play important roles in the development and function of organisms [102, 79, 145, 43, 44]. Similarly, directed active forces in dense matter are expected to play a role in determining rheology [52, 14, 13]. As discussed in Chapter 1, simulations and experiments have both found that such activity may control whether the cells are able to migrate in the tissue both with [44] and without [18] the influence of alignment.

Numerical studies of the influence of motility in tissue rheology have been conducted in particulate models [52] the Potts model [59, 26] and the Self-Propelled Voronoi (SPV) model [18, 44]. These investigations have generally indicated that motile forces tend to promote fluidity and enhance diffusion. The investigation by Bi *et. al.* [18] reveals a transition line separating rigid, glass-like states, where cells are trapped in cages for long times, from fluid-like states where cells frequently exchange neighbors. Notably, this same investigation revealed that this transition is described by an order parameter based on cell shapes. Some experimental evidence has already started to confirm a dimensionless “shape index” may be sufficient to predict whether cells will migrate through real tissues [94].

The numerical investigation which revealed this transition was performed using the SPV model. In the SPV, cells are described as irregular polygons obtained from a Voronoi tiling of the plane. While this description has numerical advantages for the study of topological transitions, a recent study by Sussman and Merkel has indicated that in two dimensions the Voronoi tiling constraint may have a substantial impact on tissue rigidity [133]. To understand the impact of these constraints on the transition to a fluid state, we have constructed a novel model for a motile tissue that preserves the freedom of cell shape. To our knowledge, the “Active Vertex Model” presented herein has not been explored in any previous work. Therefore, we include here a more detailed description of the model, as well as quantification of the solid-like and fluid-like states.

2.2 The Vertex Model with Motility

In the Vertex Model [38, 126, 55, 17] cells are modeled as irregular polygons tiling the plane, but in contrast to Voronoi models, the degrees of freedom are the positions of the vertices of the spatial tiling. Previous studies using this model have typically involved searching for geometric states which minimize the tissue energy,

$$E_{VM} = \sum_a E_a = \sum_a \kappa_A [(A_a - A_0)^2 + \kappa_P (P_a - P_0)^2] , \quad (2.1)$$

where the sum runs over all cells a and κ_A and κ_P are elastic moduli. As discussed in Section. 1.3.1, this energy drives cell area A_a toward a preferred value A_0 and perimeter P_a toward a preferred value P_0 . Although the simplest implementation of an Active Vertex Model would be to allow each vertex to be self-propelled, we would like to model the behavior of a polarized motile cell moving coherently along a specific direction. Therefore, we extend this model to include self propulsion of cell a in the direction

$$\hat{\mathbf{n}}(\theta_a) = \cos(\theta_a)\hat{\mathbf{x}} + \sin(\theta_a)\hat{\mathbf{y}} , \quad (2.2)$$

where the cell propulsion angle θ_a is governed by

$$\partial_t \theta_a = \eta_r, \quad (2.3)$$

with η_r being a white gaussian noise defined by

$$\langle \eta_R(t) \rangle = 0 \quad (2.4)$$

and

$$\langle \eta_R(t_1) \eta_r(t_2) \rangle = 2D_r \delta(t_1 - t_2). \quad (2.5)$$

Assuming that cell motion takes place in the overdamped limit, vertex μ will then follow an equation of motion,

$$\partial_t \mathbf{r}^\mu = -\frac{1}{\gamma} \frac{\partial}{\partial \mathbf{r}^\mu} E_{AVM}, \quad (2.6)$$

where γ is the substrate friction. The total effective energy,

$$E_{AVM} = \sum_{\text{cells}-a} [E_a - \gamma v_0 \hat{\mathbf{n}}(\theta_a) \cdot \mathbf{r}^a], \quad (2.7)$$

now captures both the cellular self-propulsion forces (of magnitude v_0) in addition to the standard shape energy terms from Eq. 2.1. The geometric center (centroid) \mathbf{r}^a of cell a defined by

$$\mathbf{r}^a = \frac{1}{6A_a} \sum_{\nu} (\mathbf{r}^{\nu} + \mathbf{r}^{\nu+1}) (\mathbf{r}^{\nu} \times \mathbf{r}^{\nu+1}) \cdot \hat{\mathbf{k}}, \quad (2.8)$$

captures the center of mass of a polygon of uniform mass density. Here, the sum goes counterclockwise over the N_a vertices on cell a and $\mathbf{r}^{N_a+1} = \mathbf{r}^1$. The polygon area may be expressed in similar terms as

$$A_a = \frac{1}{2} \sum_{\nu} (\mathbf{r}^{\nu} \times \mathbf{r}^{\nu+1}) \cdot \hat{\mathbf{k}}. \quad (2.9)$$

While it is uncommon to think of such a self-propulsion force as coming from an energy, writing things in this way permits an analogy with the Voronoi model. In the SPV, the degrees of freedom are the Voronoi centers and we might imagine constructing the same energy Eq. 2.7, using these Voronoi centers as the $\{\mathbf{r}^a\}$. It is easy to see that using these as the degrees of freedom in the overdamped equation of motion

$$\begin{aligned}\partial_t \mathbf{r}^a &= -\frac{1}{\gamma} \frac{\partial}{\partial \mathbf{r}^a} E \\ &= v_0 \hat{\mathbf{n}}(\theta_a) - \frac{1}{\gamma} \frac{\partial}{\partial \mathbf{r}^a} E_{shape},\end{aligned}\tag{2.10}$$

indeed leads to the standard SPV dynamics [18, 155, 9]. We are therefore using the closest energetic analog of SPV.

The force (and therefore motion) on each vertex can be calculated by carrying out the derivatives in Eq. 2.6. Each vertex in this model is connected to 3 cells and each cell energy will contribute separate terms to the net motion of the vertex. If vertex μ is connected to cells a , b and c , then the motion breaks down into

$$\begin{aligned}\partial_t \mathbf{r}^\mu &= -\frac{1}{\gamma} \left(\frac{\partial}{\partial \mathbf{r}^\mu} E_a + \frac{\partial}{\partial \mathbf{r}^\mu} E_b + \frac{\partial}{\partial \mathbf{r}^\mu} E_c \right) \\ &\quad + v_0 \left(\frac{\partial(\hat{\mathbf{n}}(\theta_a) \cdot \mathbf{r}^a)}{\partial \mathbf{r}^\mu} + \frac{\partial(\hat{\mathbf{n}}(\theta_b) \cdot \mathbf{r}^b)}{\partial \mathbf{r}^\mu} + \frac{\partial(\hat{\mathbf{n}}(\theta_c) \cdot \mathbf{r}^c)}{\partial \mathbf{r}^\mu} \right).\end{aligned}\tag{2.11}$$

For simplicity, we may focus on the contributions from cell a . As has been identified in previous work [155], the shape energy produces tension-based and pressure-based forces on each vertex. The shape-based force on vertex μ from cell a reads

$$\frac{\partial}{\partial \mathbf{r}^\mu} E_a = -\frac{\Pi_a}{2} (\hat{\mathbf{n}}^{ab} l^{\mu\gamma} + \hat{\mathbf{n}}^{ac} l^{\mu\lambda}) - T_a (\hat{\mathbf{I}}^{\mu\gamma} + \hat{\mathbf{I}}^{\mu\lambda}),\tag{2.12}$$

where γ and λ index the vertices of cell a which neighbor μ , $l^{\mu\gamma}$ ($l^{\mu\lambda}$) and $\hat{\mathbf{I}}^{\mu\gamma}$ ($\hat{\mathbf{I}}^{\mu\lambda}$) are the length and direction of the edge connecting vertex μ to vertex γ (λ) and the unit vector $\hat{\mathbf{n}}^{ab}$ ($\hat{\mathbf{n}}^{ac}$) points across the edge shared by cell a and cell b (c) as in Fig 2.1. The tension and

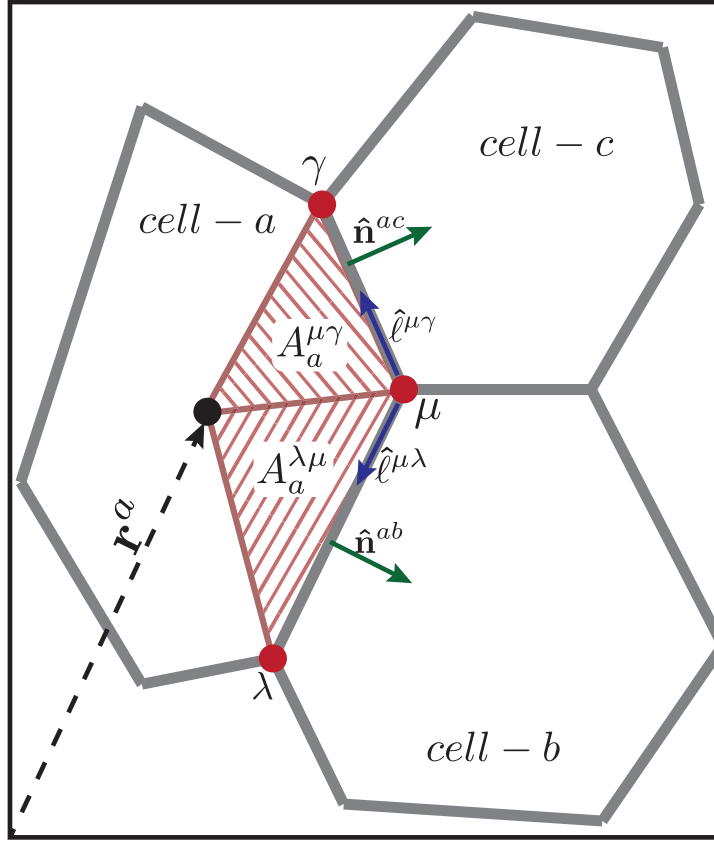


Figure 2.1: Illustration of the vectors and geometric components involved in evaluating the forces on vertex μ due to the shape energy and the motility of cell a

pressure of cell a are respectively

$$T_a = \frac{\partial E_{shape}}{\partial P_a} \quad \Pi_a = -\frac{\partial E_{shape}}{\partial A_a}. \quad (2.13)$$

Similar to the above, we take the appropriate derivatives to understand the self propulsion forces which act on the vertices. Again, we will consider only the contributions from cell a .

The derivative will take the form

$$\frac{\partial(\hat{\mathbf{n}}(\theta_a) \cdot \mathbf{r}^a)}{\partial \mathbf{r}^\mu} = \frac{\partial \mathbf{r}^a}{\partial \mathbf{r}^\mu} \cdot \hat{\mathbf{n}}(\theta_a) \quad (2.14)$$

With these expressions, taking the derivative in Eq. 2.14 is tedious but straightforward. The

derivative becomes

$$\begin{aligned}
\frac{\partial r_j^a}{\partial r_i^\mu} &= \frac{1}{6A_a} \left[\delta_{ij}(\mathbf{r}^\lambda \times \mathbf{r}^\mu) \cdot \hat{\mathbf{k}} + \delta_{ij}(\mathbf{r}^\mu \times \mathbf{r}^\gamma) \cdot \hat{\mathbf{k}} \right. \\
&\quad + (r_j^\lambda + r_j^\mu)R(\pi/2)_{ik}r_k^\lambda + (r_j^\mu + r_j^\gamma)R(-\pi/2)_{ik}r_k^\gamma \\
&\quad \left. - 3(R(\pi/2)_{ik}r_k^\lambda + R(-\pi/2)_{ik}r_k^\gamma)r_j^a \right], \tag{2.15}
\end{aligned}$$

where

$$R_{ij}(\theta) = \begin{bmatrix} \cos(\theta) & -\sin(\theta) \\ \sin(\theta) & \cos(\theta) \end{bmatrix} \tag{2.16}$$

is an active vector rotation by an angle θ , i, j index cartesian components in the $x - y$ plane and Einstein summation convention is assumed for repeated indices. While the expression in Eq. 2.15 is a bit unwieldy, we note that it is translationally invariant and may consider it in a more convenient coordinate system which has its origin at \mathbf{r}_a . Using this, we find the force on vertex μ due to the motility of cell a as

$$\begin{aligned}
\mathbf{f}_i^{\mu(a)} &= v_0 \hat{n}(\theta_a)_j \frac{\partial r_j^a}{\partial r_i^\mu} \\
&= \frac{v_0 \hat{n}(\theta_a)_i}{3A_a} [A_a^{\lambda\mu} + A_a^{\mu\gamma}] \\
&\quad + \frac{v_0}{6A_a} \left[R(\pi/2)_{ik} \tilde{r}_k^\lambda \hat{n}(\theta_a)_j (\tilde{r}_j^\lambda + \tilde{r}_j^\mu) \right. \\
&\quad \left. + R(-\pi/2)_{ik} \tilde{r}_k^\gamma \hat{n}(\theta_a)_j (\tilde{r}_j^\mu + \tilde{r}_j^\gamma) \right], \tag{2.17}
\end{aligned}$$

where $A_a^{\lambda\mu}$ and $A_a^{\mu\gamma}$ are the area of triangles with vertices $\{\mathbf{r}^a, \mathbf{r}^\lambda, \mathbf{r}^\mu\}$ and $\{\mathbf{r}^a, \mathbf{r}^\mu, \mathbf{r}^\gamma\}$ respectively, as shown in Fig. 2.1. While this expression does not lend itself to insight, we can see on inspection that the first terms will move the vertex in the direction of $\hat{\mathbf{n}}(\theta_a)$. The second terms in the large square brackets will roughly serve to shrink the length of interfaces at the back of the cell, while expanding the length of interfaces at the front.

While these forces determine the continuous time-evolution of the vertices, there can be

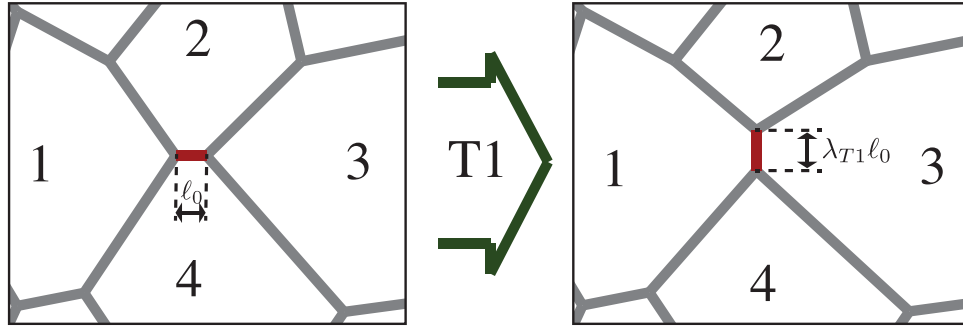


Figure 2.2: A T1 topological rearrangement in our AVM simulations identifies an edge with length $l_0 < l_c$, rewires the network connections appropriately, rotates by $\pi/2$, and extends the edge length to a factor λ times its original length.

no finite migration of cells through the tissue until topological rearrangements are allowed. We therefore include a protocol for T1 rearrangements (as shown in Fig 2.2) which are sufficient to explore the space of cellular topological configurations at constant density. In practice, the edge lengths are periodically checked after a time t_{T1} for values lower than a threshold l_c . These edges are topologically rearranged so that the two cells which share the edge are no longer in contact. The edge is then rotated by $\pi/2$ and the length extended by a factor λ_{T1} . The value of $t_{T1} = 0.05$ used here is chosen for speed of simulation, while the rescaling factor $\lambda_{T1} = 2$ is chosen to avoid “T1-traps” whereby the same transition may repeat itself regardless of energetic favorability. the cutoff length $l_c = 0.04$ is chosen small enough to make the transition appear continuous but also large enough so that a vertex may “find” the desired T1. The parameters l_c , λ_{T1} and t_{T1} have been separately varied within reasonable ranges and the impact on the dynamics appears insubstantial.

We note again that this form of the Active Vertex Model is chosen to minimize the differences with the Self-Propelled Voronoi model. The differences are limited to the following: (1) the Active Vertex Model has more degrees of freedom, avoiding the shape constraints of Voronoi tessellations, (2) T1 rearrangements in the AVM must be done by hand, while in the SPV they come about naturally and (3) motility in the AVM is designed to propel the

centroid of the cell, whereas the SPV this is replaced by the Voronoi center.

Simulations of the AVM are developed and run using the “cellGPU” codebase [132].

2.3 Rheological States of the Model

Since this model for confluent tissue dynamics has not been explored in any previous work, we first simulate and search for glassy states. We quantify the rheological state of the system by using two familiar metrics: the mean square displacement and the self-overlap function. The self-overlap function is defined as

$$\mathcal{O}(t) = \frac{1}{N_{cells}} \sum_a \Theta(b - |\mathbf{r}^a(t) - \mathbf{r}^a(0)|) , \quad (2.18)$$

where Θ is the heaviside function and b represents the size of a typical cage in natural units and is set to 0.5 for the purposes of this work. All distances are measured in units of $1/\sqrt{\rho}$, where ρ is the system number density. The function \mathcal{O} has a value of 1 at $t = 0$ and will decay toward zero as cells travel past this caging distance b . The structural relaxation time $\tau_{\alpha 0}$ is estimated as the point at which the self-overlap decays below $1/e \sim 0.368$ of its initial value and is an estimate of the uncaging time. The results of averaging this timescale over 10 systems of $N_{cells} = 300$, displayed in Fig. 2.3, are in line with expectations from previous work in the Self-Propelled [18] and Thermal [134] Voronoi models. Less motile tissues at lower s_0 (higher cortical tension) are indeed glassy and have long relaxation times. The tissue may be effectively fluidized by either increasing v_0 (higher effective temperature) or increasing s_0 (higher cell-cell adhesion).

The uncaging time, as estimated by $\tau_{\alpha 0}$, is useful for quantifying the system dynamics. However, this metric of rheology combines information about the competition between mechanical and motile forces with the inherent timescale of the motile dynamics. In other words, cells may be slow to escape their cages either because they have a small intrinsic speed v_0 , or because they are unable to surmount the energy barriers. We would therefore like to

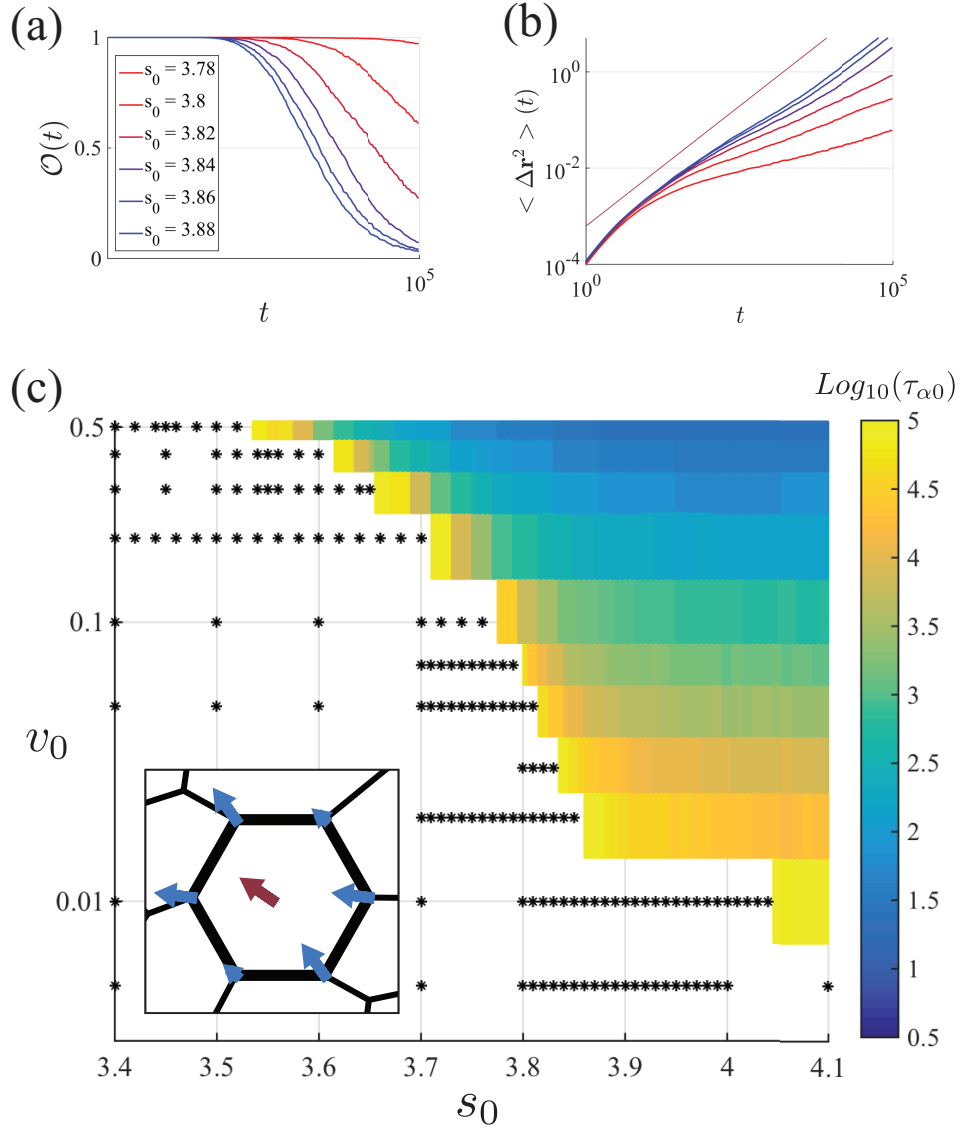


Figure 2.3: Quantification of phase behavior in the Active Vertex Model (AVM) with $D_r = 1$ and $N_{cells} = 300$. In (b), the timescale $\tau_{\alpha 0}$ of the decay of the overlap function grows beyond the length of simulations as the vertex model tuning parameter s_0 is decreased while $v_0 = 0.05$ is held fixed. In (b), the mean square displacement of cell centers for the same phase points indicates this increasing timescale is associated with subdiffusive caging behavior. In (c), $\tau_{\alpha 0}$ is shown on a logarithmic colorscale for a representative set of points in the $s_0 - v_0$ plane. Black stars indicate phase points where $\tau_{\alpha 0}$ is too long to be resolved with our data. The inset shows the implementation of motile forces prescribed by Eq. (2.7).

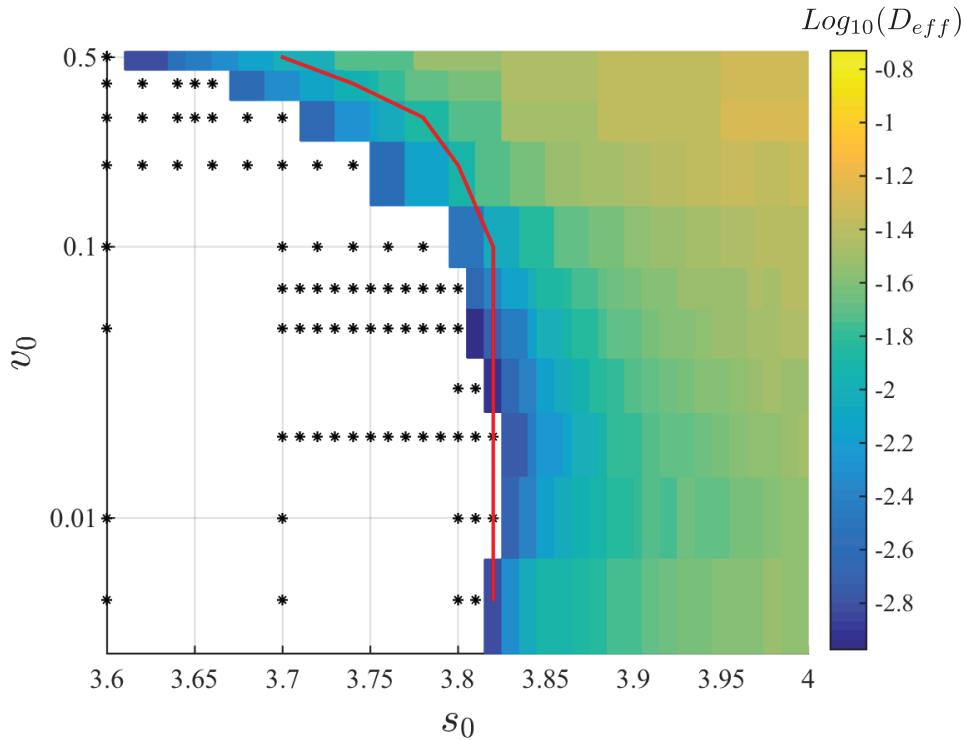


Figure 2.4: Colormap of phase behavior quantified with the normalized effective diffusion. Black stars indicate points where $\frac{D_{\text{eff}}}{D_0} < 10^{-3}$. The red line shows the boundary of the region where $q > 3.82$, which indicates a connection between sub-diffusive behavior and cell shape similar to that seen in the SPV.

understand these dynamics separately. For this reason, and to connect with existing results, we will do this using the effective self-diffusivity employed by Bi *et. al.* [18]. Formally, the self-diffusivity is defined as

$$D_s = \lim_{t \rightarrow \infty} \frac{\langle [\Delta \mathbf{r}(t)]^2 \rangle}{4t}, \quad (2.19)$$

where $\langle [\Delta \mathbf{r}(t)]^2 \rangle$ is the mean square displacement of cells, with $\Delta \mathbf{r}(t) = \mathbf{r}(t) - \mathbf{r}(0)$. The dimensionless diffusivity employed in Ref. [18] may then be defined as $D_{\text{eff}} = D_s/D_0$ where $D_0 = v_0^2/(2D_r)$ is the self-diffusivity of active Brownian particles without interactions. To approximate D_s from simulations that span a finite time, we perform a linear fit of the msd data for times past the ballistic regime (i.e. between $t = 10/D_r$ and the end of the simulation). The self-diffusivity is then approximated as one quarter of the slope of this fit.

The colormap of the effective diffusion in Fig. 2.4 displays qualitative agreement with results from the SPV model [18]. Cells with very small effective diffusion are found at the lowest values of s_0 and v_0 , where the tissue is expected to be rigid. The diffusion may be greatly enhanced with an increase in v_0 or by an increase in s_0 . At the lowest motility values, this transition is most sensitive near the rigidity transition expected from the investigation of static tissue $s_0^* \sim 3.81$ [16]. As expected from the discussion above, this phase behavior is qualitatively different from that presented in Fig. 2.3 for the uncaging time $\tau_{\alpha 0}$. In particular, D_{eff} is able to identify a regime at low motility where cells are energetically capable of escaping their cages, despite the long time it takes them to arrive there. We note that the same can effect can be identified in the data for self-overlap by measuring $\tau_{\alpha 0}$ in units of $\tau_0 = \frac{b^2 D_r}{2v_0^2}$, similar to the normalization of D_{eff} .

To inspect whether this transition from a solid-like state to a fluid like state displays a structural order parameter similar to the SPV model [18], we inspect the dimensionless shape index $q = \langle P/\sqrt{A} \rangle$. The red line in Fig 2.4 shows the boundary of the region defined by $q > 3.82$, which indicates a rough correlation between the effective diffusion and this average cell shape. Overall, this investigation situates our expectations for future investigations using this model.

The effect of the rotational diffusion D_r on the phase behavior in Fig. 2.4 was included in the investigation by Bi *et. al.* [18] for the SPV model. They found that at high self-propulsion, states which were previously fluid-like may be rigidified by increasing D_r , while at low self-propulsion D_r has little effect. This suggests that persistent self-propulsion is more efficient in fluidizing a tissue. While we do not directly explore this effect here, the qualitative behavior is expected to be the same. Future work may include such an investigation.

Chapter 3

Glassy States in Confluent Tissues with Mitosis and Apoptosis

As discussed in Section 1.3.1, experiments conducted over the past decade [2, 115, 94] have indicated the existence of glassy states in confluent epithelial tissues. This evidence includes the observation of dynamical heterogeneities characteristic of supercooled liquids [2], and caging effects in motile cell trajectories [94]. In tandem, many varied microscopic models [59, 16, 18, 155] of tissue have put forth clear indications as to the origin of these glassy phenomena. Altogether, these combined works appear to be on the way towards a coherent and perhaps paradigmatic understanding of glassiness and rigidity in tissues.

In the same living tissues, constituent cells will often undergo mitosis (cell division) and apoptosis (programmed cell death) in a regulated cell life cycle. These cell life cycle events are necessary for the survival and function of many tissues [107, 138]. Introducing and removing mechanical elements from any system should impact the dynamics, and it is therefore important to examine the effect of cell division and cell death on the tissue glassy state

Recent simulations have suggested that the presence of cell division and cell death should generically render a tissue fluid [81, 82, 105, 76]. In the work of Matoz-Fernandez *et. al.* [81],

a particle-based model of a dense tissue indicates that even at small rates k_δ of cell division and death per cell, one will not observe sub-diffusive behavior in the cell trajectories. This therefore poses a serious question for the experiments and proximal theories: why are caging behavior and glassiness observed at all?

Earlier work by Ranft et. al. [105] at the continuum level considered the effect of these cell division & death events on a model of 3-dimensional elastic tissue. Their analytical and numerical findings suggest that cell dynamics will be diffusive and controlled by k_δ in the limit of infinitely large tissue.

These investigations include cell division and death as the only forces driving the dynamics. However, epithelial cells may also generate tractions to propel themselves across a substrate and escape the cages set by their neighbors. The timescale over which cells may escape their cages reflects the rigidity of the tissue. Even in the absence of cell division and cell death, this uncaging timescale varies over orders of magnitude depending on the tissue mechanical properties and the magnitude of the propulsive forces. The full dynamics of tissues which experience motile forces in addition to mitosis and apoptosis should therefore have contributions from each of these sources of internal driving. In particular, it seems natural that the observed relaxation time of a tissue will be set by a competition between the timescale of cell cycling events and the timescale of cage escape due to motility and mechanical energy barriers.

Here, we investigate the influence of these driving forces on tissue using a modified version of the Vertex Model which has been used extensively to understand patterning and rigidity in tissues [38, 55, 126, 17, 16, 84]. Our modified model includes the influence of motility as described in Chapter 2 as well as a single controlled rate of mitosis and apoptosis. Using this model we confirm that the tissue exhibits signatures of glassy dynamics in the presence of a slow, but finite, rate of mitosis and apoptosis. We identify the finite range of cell division & death rates for which the tissue dynamics are effectively unchanged.

In the opposite limit, where cell cycle events happen fast, we find that tissue motility

and rigidity continue to play a role. To understand this combined influence, we carefully investigate the displacements produced by single mitosis and single apoptosis events. Each event produces an Eshelby-like displacement field of tissue cells, in addition to a mechanical noise. From these ingredients, we construct simplified models that capture the contribution of mitosis and apoptosis to the observed motion of cells. The results of this model provide insight which allows us to collapse the dynamical data over a range of parameters into a scaling plot, revealing a universal crossover between cell-cycle-dominated and motility-dominated rheology.

3.1 Tissue Simulations with Cell Division and Cell Death

We perform simulations of a dynamic epithelial tissue with dividing and dying cells using a modified version of the well-studied vertex model [38, 126, 55, 17, 16]. In this framework, the plane is tiled by polygonal cells. As discussed in Section 1.3.1, the influence of subcellular forces may be captured by the energy functional

$$E_{total} = \sum_a [\kappa_A(A_a - A_{0a}) + \kappa_P(P_a - P_{0a}) - \gamma v_0 \hat{\mathbf{n}}(\theta_a) \cdot \mathbf{r}^a], \quad (3.1)$$

where the area A_a and perimeter P_a of cell a tend toward a target area A_{0a} and target perimeter P_{0a} . Including cell division and cell cycling events means that these target shape parameters will not always be the same for all cells. The last term on the right hand side captures the forces exerted by cell a to propel itself across the substrate. As in Section 2.2, cell a will propel its geometric center in the direction $\hat{\mathbf{n}}(\theta_a)$. Here the angle of motion θ_a evolves as in Eq. 2.3 by a white gaussian noise with a rotational diffusion D_r . Motion of cells is assumed to be overdamped and the position of vertex μ will then follow the equation of motion

$$\partial_t \mathbf{r}_\mu = -\frac{1}{\gamma} \nabla_\mu E_{tot}. \quad (3.2)$$

For the purposes of this work, we set $D_r = \kappa_P = \kappa_A = \gamma = 1.0$ and perform simulations using the “cellGPU” codebase [132].

3.1.1 Simulation of mitosis and apoptosis events

We would now like to incorporate the influence of cell cycle events in these vertex model simulations. To identify an appropriate procedure, we first acknowledge the expected influence of changing cell number in our model. Consider a tissue of cells having some target perimeter P_0 and target area A_0 and for which each cell is able to realize these target values. If some apoptosis events occur with the system size fixed, then these cells will no longer be able to realize their target A_0 as they must continue to tile the same space. Lending from known results from the rigidity transition in these tissues [16, 85] we might also expect that the cells will no longer be able to realize their target P_0 , and thereby a potentially drastic change in tissue rheology may result.

In an effort to minimize such cell density effects, we choose to work in a constant-number ensemble. In our simple implementation, each instance of apoptosis will be accompanied by a mitosis event somewhere else in the tissue. In addition, the implementation of the individual cell cycle events is chosen to preserve the sum $A_{0T} = \sum_a A_{0a}$ at all times.

In apoptosis, a cell will abruptly contract to a small size and then extrude itself, effectively disappearing from the 2d monolayer [111]. Shown in Fig.3.1(d-f), our simple realization of apoptosis on cell a begins with setting $A_{0a} \rightarrow 0$ and $P_{0a} \rightarrow 0$. This change induces the rapid contraction of cell a to small size and generally will lead to a final triangular shape. The simulation then will detect triangular cells which are smaller than some threshold area A_{min} and delete them.

Similarly, in the process of mitosis a cell will expand, eventually reaching a threshold size checkpoint and dividing into two complete cells [27, 31, 128], all the while maintaining tissue cohesion [4]. While this process typically spans a much longer time period than the event of a cell death, we model this growth process as similarly instantaneous to preserve

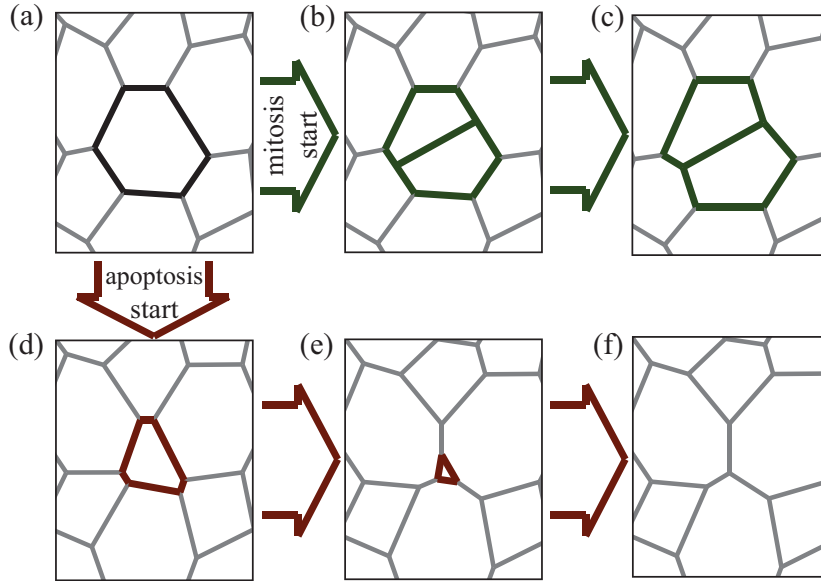


Figure 3.1: The process for a single mitosis event in our model is shown sequentially in (a-c). Starting again with the initial cell in (a), the model steps for apoptosis are shown sequentially in (d-f).

the constant A_{0T} and for simplicity. Shown in Fig 3.1, in the division of cell a opposite edges of the cell are chosen at random, thus determining the axis of the division. A vertex is then added to the center of each edge and these new vertices are connected with a new edge. Naturally the product is two closed polygonal cells out of one, and the shape parameters of these new cells are then set to the uniform value of the other cells in the tissue. These cells are then allowed to expand dynamically in the simulation. Similar division dynamics were studied in a quasi-static system by others, including Farhadifar *et. al.* [38].

In practice, such constant number simulations allow us to enforce the global cell cycle event rate k_{Δ} , which is implemented as a Poisson process. This sets the effective cycle rate per cell which may be written as $k_{\delta} = k_{\Delta}/N_{cells}$. Note that k_{δ} is a more appropriate observable parameter for real biological systems whose cell cycle timing does not depend strongly on the overall tissue size. We therefore use $k_{\delta} = 1/\tau_{\delta}$ as our tuning parameter.

In simulations with cell division and death, complications arise when trying to extract

cell trajectory data. This is because many trajectories will start and end during the course of the simulation. Rather than parse this network of trajectories, we follow the method used in [81] and exclude a small (%10) subset of the cells from the cell cycle events. Using these “tracer” cells to obtain our dynamical data is both convenient and affords the closest comparison with the existing investigation in [81].

3.2 Tissue rheology in the presence of mitosis and apoptosis

Similar to the analysis in Section 2.3, tissue rheology may be quantified using the trajectories of cell center positions $\mathbf{r}_a(t)$ over the course of simulations. This may be accomplished with either the mean square displacement

$$\langle [\Delta \mathbf{r}(t)]^2 \rangle = \left\langle \frac{1}{N_{cells}} \sum_a [\mathbf{r}^a(t) - \mathbf{r}^a(0)]^2 \right\rangle, \quad (3.3)$$

where the angle brackets indicate an ensemble average, or with the self-overlap, defined by

$$\mathcal{O}(t) = \frac{1}{N_{cells}} \sum_a \Theta(b - |\mathbf{r}^a(t) - \mathbf{r}^a(0)|), \quad (3.4)$$

where Θ is the heaviside function while b represents the size of a typical cage and is set to 0.5 in natural units for the purposes of this work. All distances are measured in units of $1/\sqrt{\rho}$, where ρ is the system number density. The function \mathcal{O} has a value of 1 at $t = 0$ and will decay toward zero as cells travel past this caging distance b . We may then define a timescale τ_α as the time required for the overlap to decay past $1/e \sim 0.368$. This timescale is an estimate of the time required for cells to escape their cages. The notation intentionally differs from that in Section 2.3, to distinguish $\tau_{\alpha 0}$ as the uncaging time in the limit of zero apoptosis and zero mitosis ($k_\delta \rightarrow 0$).

We search for “glassiness” as identified by a sub-diffusive mean square displacement and

a long overlap decay time (τ_α) as in Section 2.3. This is guided by the simple expectation that rheology is determined by a competition between the timescale τ_δ of division and death events and the timescale of motility driven cage escape $\tau_{\alpha 0}$. In particular, we expect to recover the dynamics of the “bare” (free of cell division and death) AVM for sufficiently small values of τ_δ . This can be seen in Fig. 3.2 (b) and (c), where sufficient decrease in the value of k_δ leads the msd and the self-overlap to approach a limiting form which matches the data from Fig. 2.3. This is useful for identifying the limits of when cell division and cell death events have an impact on mechanics.

That the influence of mitosis and apoptosis will be negligible in the limit $\tau_\delta \gg \tau_{\alpha 0}$ where motility operates on a much faster timescale, is reasonable. One may expect to find the opposite behavior in the limit $\tau_\delta \ll \tau_{\alpha 0}$, where motility-based dynamics should play a negligible role. To check this, we vary s_0 , because $\tau_{\alpha 0}$ decreases as s_0 increases, in Fig. 3.2. When $\tau_{\alpha 0}$ is large and τ_δ is small (k_δ is high) we observe structural relaxation times τ_α which are independent of s_0 and by proxy, $\tau_{\alpha 0}$.

3.3 Simple null model for interaction between τ_δ and

$\tau_{\alpha 0}$

The limiting behaviors described above agree with expectations, and hint at possibilities for understanding data in the intermediate regime where both timescales $\tau_{\alpha 0}$ and τ_δ will play a role. To establish expectations in this regime, we first develop a very simple null model for the interactions between cell death & division and glassy dynamics. Specifically, we assume that the overlap decay rate $\frac{1}{\tau_\alpha}$ of a dividing tissue is determined by the weighted sum of the bare cage escape rate ($\frac{1}{\tau_{\alpha 0}}$) and the rate of division & death events according to

$$\frac{1}{\tau_\alpha} = \frac{C_1}{\tau_{\alpha 0}} + \frac{C_2}{\tau_\delta}, \quad (3.5)$$

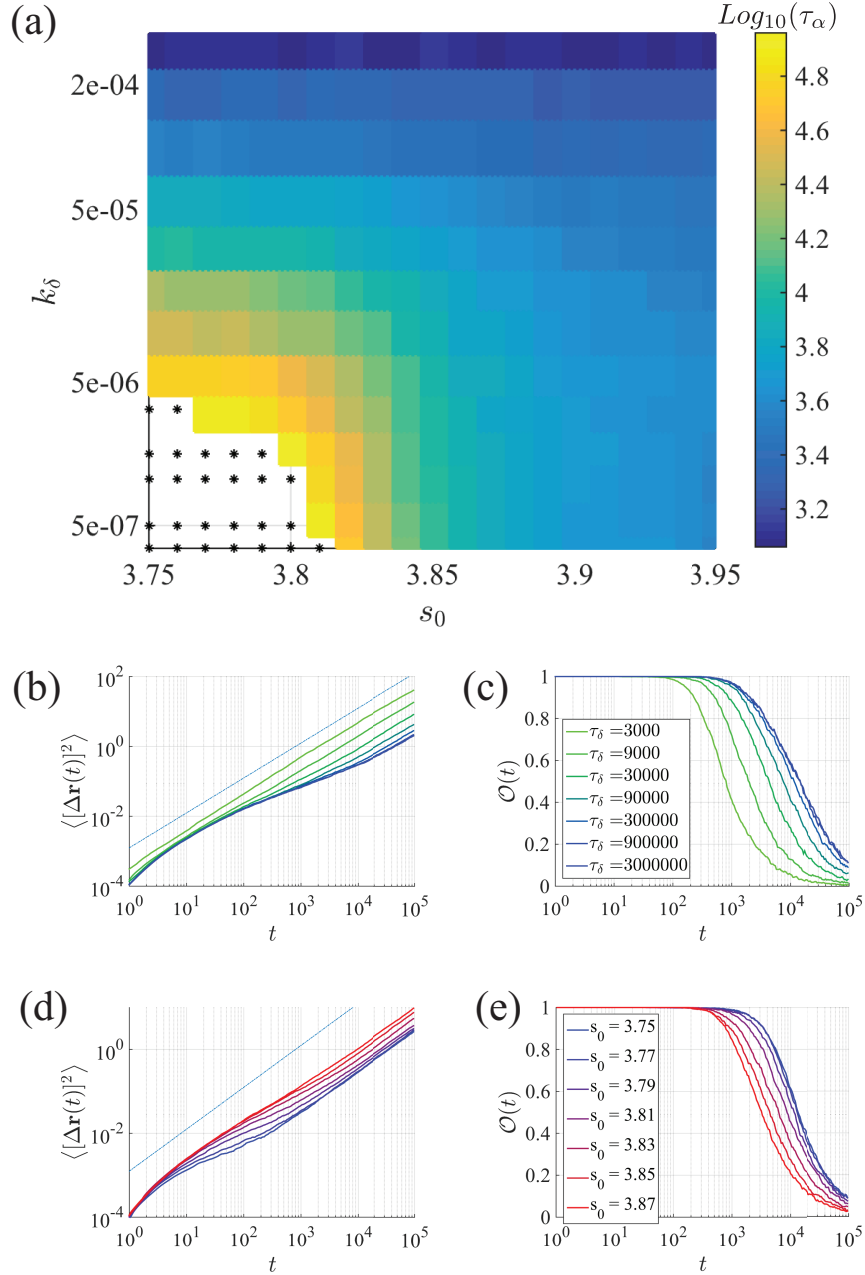


Figure 3.2: Rheological measures of tissues with mitosis and apoptosis for $v_0 = 0.05$ and $D_r = 1$. In (a), the measured overlap decay τ_α as a function of s_0 and the cell cycling rate k_δ is displayed as a colormap, indicating generically that k_δ tends to fluidize the tissue. In (b) and (c), mean square displacement and overlap curves are plotted for constant $s_0 = 3.83$ over a series of k_δ and show that the dynamics approach the expected values from the “bare” AVM at small enough k_δ . In (d) and (e) are a similar series of curves for a constant $k_\delta = 1.6 \times 10^{-5}$ over a series of s_0 values. Here, the approach towards a universal behavior (expected at the lowest values of s_0) only becomes clear at long times.

where τ_δ is the time between division and death events for a single cell and C_2 captures the displacements of surrounding cells resulting from the division & death events, which is made more precise in the following sections. The weight C_1 , which captures the relative contribution of bare glassy dynamics, is set to unity based on the limiting behavior identified in the previous section. The strong assumption we have made here is that the two rates add in series and are not strongly correlated. This null model predicts that the quantity $\frac{\tau_\alpha}{\tau_{\alpha 0}}$ will be a function only of $\frac{\tau_\delta}{\tau_{\alpha 0}}$. As shown in Fig. 3.4(a), this works fairly well, indicating that there is a regime with fast divisions where the dominate the rheology and $\tau_\alpha \propto \tau_\delta$, and a regime with slow divisions where $\tau_\alpha \perp \tau_\delta$. However, there is not a perfect collapse. One possibility is that the coefficient C_2 , which captures displacements generated by cell division and death, does depend significantly on the inherent tissue rheology $C_2 = C_2(\tau_{\alpha 0})$. This possibility is explored further in the next section.

3.4 Flow and fluidization from individual mitosis and apoptosis events

To quantify the effect of a single cell cycling (division or death) event on the motion of surrounding tissue, we perform a special set of “single-event” simulations. In these, the standard AVM is run for a short equilibration time before a single cell is chosen at random to undergo either apoptosis or mitosis in a randomly chosen direction. Following this, the AVM continues to run, and the motion of the surrounding tissue cells are monitored and quantities of interest are averaged over 1000 realizations.

We measure the individual vector cell displacements $\{\mathbf{u}_i\}$ and use them to construct a few useful quantities. In order to resolve coherent spatial data, the cells are first binned based on their distance from the event (and in the case of cell division based on their angle relative to the division axis orientation). Within each bin, we calculate two quantities: the vector averaged displacement $\mathbf{u}(r, \theta)$ and the vector standard deviation of this average, $\boldsymbol{\sigma}_{(m,a)}(r, \theta)$,

where the subscripts m and a refer to mitosis and apoptosis events, respectively.

As noted by Puosi *et. al.* [103] for the similar case of shear transformations in thermal sphere packings, the vector averaged $\mathbf{u}_{(m,a)}(r, \theta)$ captures the affine elastic response of the surrounding medium. Straightforward calculation of the response of a homogeneous elastic medium to localized strains [103] suggests that the affine field associated with either a cell death or cell division event should fall off as r^{-1} in two dimensions. This is consistent with the numerical observations in our model, shown in Fig. 3.3 (a), (b) and (c). In particular, the dashed line in Fig. 3.3(c) shows the expected scaling of r^{-1} , which is in reasonable agreement with the data. The “non-affine” piece captured in $\boldsymbol{\sigma}_{(m,a)}(r, \theta)$ quantifies the additional cell displacements which are expected to arise in the vicinity of the event due to disorder in the tissue structure.

3.4.1 Toy Models for Cell Displacements

Guided by these single event results, we construct simplified models to estimate their influence on measurable quantities, such as τ_α . As pointed out by Ranft *et. al.* [105], the “affine” displacements identified above will produce a constantly changing reference state in an elastic material. Therefore, while these cells may oscillate in their cages, the cages themselves move as a result of each event via the displacement fields $\mathbf{u}_{(m,a)}(r, \theta)$. We would like to estimate the effect of this changing reference state on the mean square displacement of our tracer cells. In addition, these events will create additional non-affine displacements on top of the affine motion.

In practice, the diffusion produced by each of these contributions can be evaluated separately. Assuming these contributions do not display significant correlations (other than in their chosen locations) the diffusion constants from each mechanism may be summed to find the total diffusion due to cell cycling events

$$D_\delta = D_{(a)}^{\text{aff}} + D_{(m)}^{\text{aff}} + D_{(a)}^{\text{non-aff}} + D_{(m)}^{\text{non-aff}}. \quad (3.6)$$

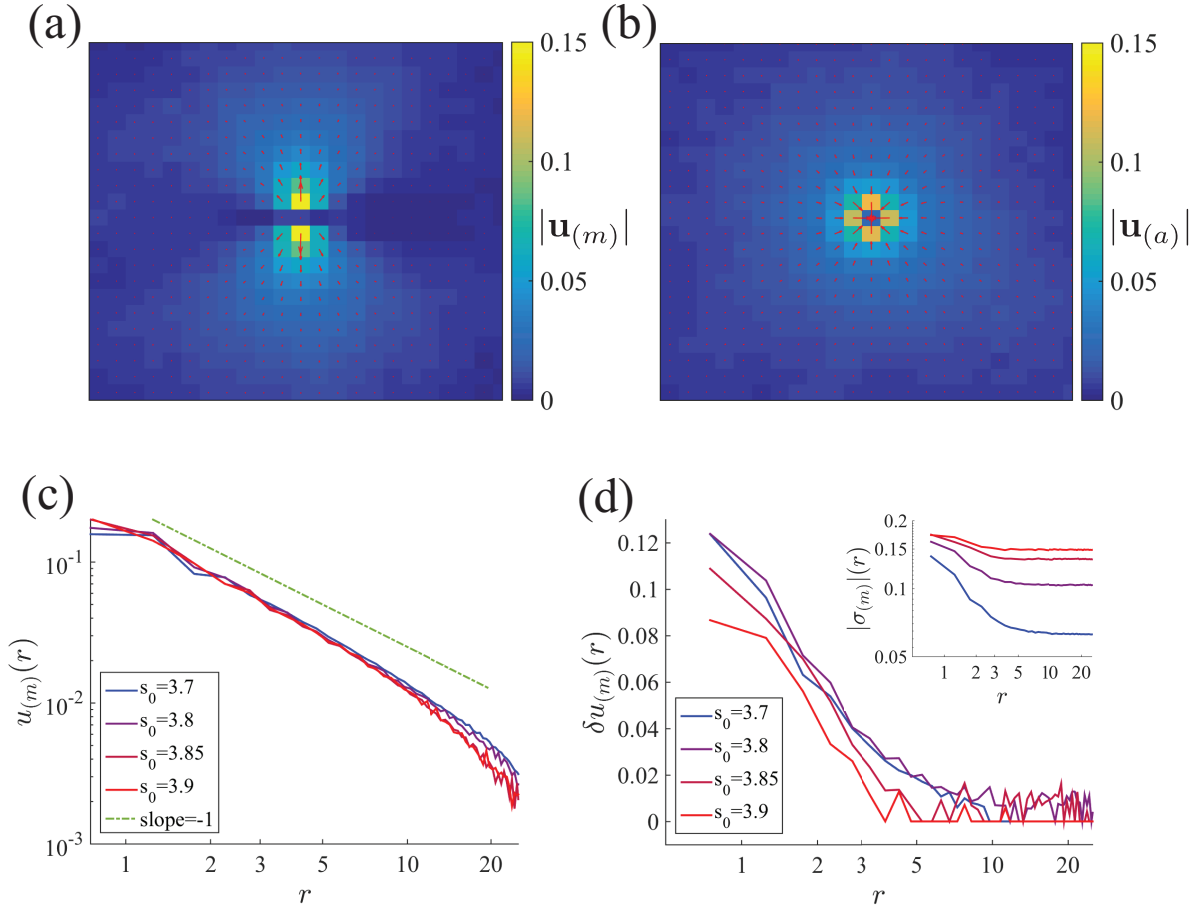


Figure 3.3: Affine and non-affine displacements quantified in response to a single mitosis/apoptosis event for $N_{cells} = 5000$. In (a) and (b), arrows show the affine displacements in response to a mitosis and apoptosis, respectively, for a tissue with $s_0 = 3.6$, $v_0 = 0.05$. Colormap indicates the magnitude of these affine vectors with grid spacing 1.5. In (c), the magnitude of affine displacements averaged over angles is plotted as a function of distance from a mitosis event. The purple dot-dashed line shows the agreement with the expected scaling of $1/r$ for a series of s_0 values. In (d), the values for the $\delta u_{(m,a)}(r)$ per Eq. 3.10 are plotted similarly, revealing a finite region of non-affine displacements. The inset in (d) shows the same non-affine data without the long distance behavior removed, showing a plateau to a finite value.

Here, $D_{(m,a)}^{\text{aff}}$ captures the diffusion due to $\mathbf{u}_{(m,a)}(r, \theta)$, while $D_{(m,a)}^{\text{non-aff}}$ captures diffusion due to $\boldsymbol{\sigma}_{(m,a)}(r, \theta)$ in a manner which is made more precise in the following sections. Each analysis will rely on the simplifying assumptions (1) that we may ignore the randomness in the timing of the divisions and deaths and (2) that the effect from each event is felt instantaneously by

the surrounding tissue; in other words, the speed of sound in the tissue is fast compared to the structural relaxation. This enables us to simply sum up the $n(t) = tN_{cells}/\tau_\delta$ events that will have taken place after a time t .

Estimating affine contributions to displacement

To estimate the first and second terms on the right hand side of Eq. 3.6, we consider the displacement of a tracer cell as a result of the affine motion $\mathbf{u}_{(m,a)i}(r, \theta)$ produced in each cell cycle i . With the dynamics

$$\Delta \mathbf{x}_{(m,a)}(t) = \sum_i^{n(t)} \mathbf{u}_{(m,a)i}(r, \theta), \quad (3.7)$$

the msd may be computed as

$$\langle \Delta \mathbf{x}_{(m,a)}^2(t) \rangle = \sum_i^{n(t)} \langle \mathbf{u}_{(m,a)i}^2(r, \theta) \rangle. \quad (3.8)$$

where $\langle \rangle$ represents the ensemble average over the realizations of these apoptosis and mitosis events. As these contributions are each identical in form, the stochasticity here comes from the spatial positioning (and orientation) of the mitosis (apoptosis) event with respect to our tracer. Therefore, finding this average for $\langle \mathbf{u}_{(m,a)i}^2 \rangle$ amounts to integrating over the possible positions and orientations of this mitosis (apoptosis) event. Equivalently, we may center the event location in our coordinate system and instead integrate over the possible positions of our tracer. Appropriately normalized, this integral is written

$$\langle \mathbf{u}_{(m,a)i}^2 \rangle = \frac{\rho}{N_{cells}} \int_{r_{small}}^{r_{large}} dr r \langle \mathbf{u}_{(m,a)}^2 \rangle_\theta(r), \quad (3.9)$$

where the small r_{small} and large r_{large} cutoffs of integration respectively capture the typical cell neighbor spacing and the extent of the affine field. The brackets $\langle \rangle_\theta$ represent an average over angular position. We have written things this way because $\langle \mathbf{u}_{(m,a)}^2 \rangle_\theta(r) \equiv u_{(m,a)}^2(r)$ is

precisely the quantity we estimate from simulations. The data shown in Fig. 3.3 suggest it is nearly identical for apoptosis and mitosis events in our model.

Estimating non-affine contributions to displacement

We now consider the contribution to tracer displacement from the non-affine (third and fourth) terms in Eq. 3.6. We note that the quantity $|\sigma_{(m,a)}|(r)$ measured in simulations will both capture local contributions from the mitosis(apoptosis) event as well as contributions everywhere from active, motility driven, cell motions. To separate the contribution of non-affine elastic displacements from the noise generated by the active forces in the AVM, we define

$$\delta u_{(m,a)}(r) = |\sigma_{(m,a)}|(r) - |\sigma_{(m,a)}|(\infty), \quad (3.10)$$

where $\sigma_{(m,a)}(\infty)$ is the far-field plateau in the non-affine displacement field generated by active noise, shown in the inset to Fig. 3.3 (d). The resulting elastic non-affine displacement field, $\delta u_{(m,a)}(r)$, is plotted in Fig. 3.3(d) for a mitosis event.

It is clear that $\delta u_{(m,a)}(r)$ varies with s_0 , with less elastic displacement generated by divisions in the more fluid states. Similarly to Eq. 3.7, the contribution to the tracer dynamics generated by these non-affine displacements is written as

$$\Delta \mathbf{r}_{(m,a)}^{\text{non-aff}}(t) = \sum_{i=0}^{n(t)} \delta \mathbf{u}_{(m,a)i}, \quad (3.11)$$

where $\delta \mathbf{u}_i$ is the non-affine displacement produced by the i -th mitosis(apoptosis) event. This displacement is assumed to have a random direction and magnitude determined by the distribution of $\delta u_{(m,a)}(r)$ from Eq. 3.10. The mean square displacement is computed from the average $\langle \delta u_{(m,a)}^2(r) \rangle$. Since the variation in this average comes from the placement of the tracer with respect to the event, this average again takes the form of a spatial integral, explicitly written as

$$\langle \delta \mathbf{u}_{(m,a)i}^2 \rangle = \frac{\rho}{N_{\text{cells}}} \int_{r_{\text{small}}}^{r_{\text{large}}} dr r \delta u_{(m,a)}(r). \quad (3.12)$$

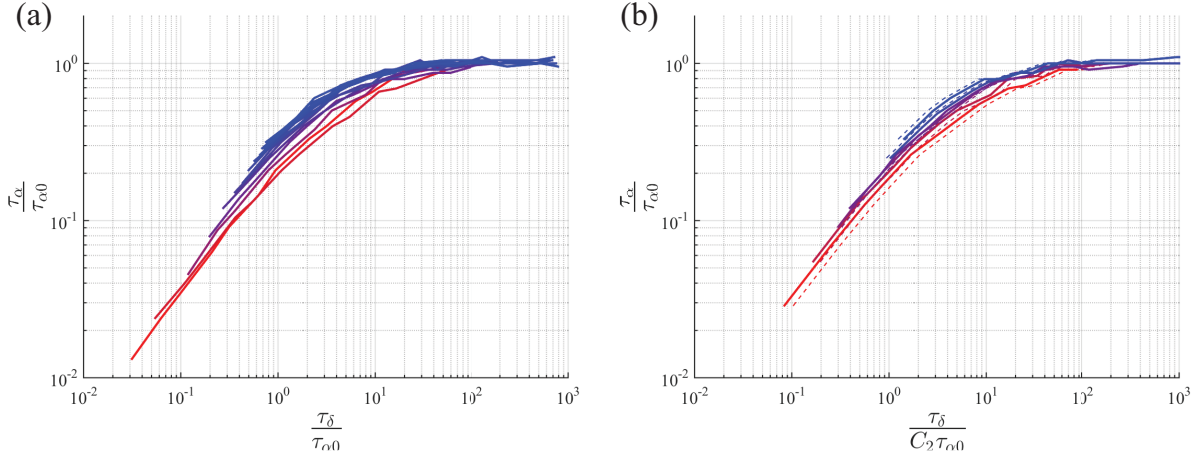


Figure 3.4: In (a) data for τ_α vs. τ_δ for a series of $\tau_{\alpha 0}$ does not collapse with simple rescaling using $\tau_{\alpha 0}$. In (b), the same data comes closer to collapse by additionally normalizing τ_δ using an averaged scale of motion ($C_2(\tau_{\alpha 0})$) extracted from single event apoptosis and mitosis data. Dotted lines represent the same data plotted for a constant C_2 . A universal curve for the crossover between mitosis/apoptosis dominated behavior and motility-dominated behavior is suggested.

3.4.2 Single event data guides a scaling collapse

Returning to Eq. 3.5, it is now clear that the term C_2 may depend significantly on s_0 , and therefore on $\tau_{\alpha 0}$. It is then not surprising that simply rescaling data for τ_α vs. T_δ with the timescale $\tau_{\alpha 0}$ (Fig. 3.4 (a)) is insufficient to collapse the data perfectly. We note that $C_2(\tau_{\alpha 0})$ can be written in terms of the integrals in Eq. 3.9 and Eq. 3.12:

$$C_2 \propto \langle \delta \mathbf{u}_{(m)i}^2 \rangle + \langle \delta \mathbf{u}_{(a)i}^2 \rangle + \langle \mathbf{u}_{(m)i}^2 \rangle + \langle \mathbf{u}_{(a)i}^2 \rangle, \quad (3.13)$$

We may therefore simply integrate the simulation data in Fig. 3.3(a) and (b). This produces an estimate for C_2 as a function of s_0 , which may then be incorporated into the scaling of τ_α data as shown in Fig. 3.4(b).

While incorporating the variation of C_2 with s_0 brings the data closer together, as shown in Fig. 3.4(b) the data at different $\tau_{\alpha 0}$ are still visibly distinct. Why then does this rescaling

factor not produce a full collapse of the data as suggested by Eq. 3.5? One reason comes from simply writing down Eq. 3.5, where a cellular rate $\frac{1}{\tau_\delta}$ and a macroscopic rate $\frac{1}{\tau_{\alpha 0}}$ are treated on similar footing. Since $\tau_{\alpha 0}$ quantifies dynamics similar to those in supercooled fluids where heterogeneity is observed, and since the Stokes-Einstein relation which connects microscopic and macroscopic rates is known to break down in such heterogeneous systems, it is not clear that the overall tissue relaxation can be expressed as such an average of rates. In addition, we have considered how the weight C_2 might vary with the intrinsic tissue rheology (as quantified by $\tau_{\alpha 0}$), but we have given no consideration to the opposite case. One might imagine that motile forces act differently on a tissue which is continuously experiencing cell division and cell death events, and it is entirely possible that the coefficient $C_1 \rightarrow C_1(\tau_\delta)$ will reflect this.

Even our estimation of the rescaling parameter C_2 was enabled by additional assumptions. Eq. 3.13 assumes that the total magnitude of motion coming from cell division and death events in a single timestep is computed from separate contributions coming from nonaffine and affine pieces of each event. However, it is entirely possible that these events interfere with one another, displaying correlations which should be incorporated in a more appropriate estimate of C_2 . In addition, we have assumed that the displacements from these cell cycling events happen nearly instantaneously, and that they therefore do not correlate with one another in time. In particular, the affine displacements destructively interfere with the periodic images of themselves as shown by the long distance dropoff in Fig. 3.3(c). The same interference may occur temporally when the division and death events are sufficiently fast compared to the speed of sound in the tissue. Finally, we note that our numeric estimates of the integrals in Eq. 3.9 and Eq. 3.12 extend from the division or death event out to a radius $L/2$. We are therefore neglecting the corners of the box, assuming them not to contribute significantly to the integral. This assumption is reasonable given the tendency of displacements to decrease with distance as shown in Fig. 3.3 (c) and (d), and is not expected to significantly impact our results.

Chapter 4

Continuum Modeling of Tissues

Pattern formation during embryonic development, coordinated tissue movements in wound healing, and the breakdown of patterning in cancer tumorigenesis have all traditionally been explained in terms of biochemical signaling, such as morphogen gradients and growth factor secretion. Although biochemical gradients are clearly important, recent work has suggested that mechanical interactions and mechano-sensitive response can play a complementary and vital role in the robust patterning of these self-organized systems. For example, the extra-cellular matrix (ECM) that contributes to the mechanical environment of cancer tissues strongly affects metastasis[41, 95], and the stiffness of an underlying substrate can control differentiation[30, 35] and collective cell migration in wound healing assays for cell monolayers[131].

Concurrent with these investigations of cell-substrate and cell-ECM interactions, another group of researchers has focused on cell-cell interactions, in an effort to understand the “material properties” of tissues. Continuum models that describe epithelia as active viscoelastic fluids[21, 20, 105, 57, 152] or active elastic sheets[7, 6, 8, 69] have been shown to reproduce many phenomena observed in wound healing assays and confined tissues. Experimental studies discovered that many 2D monolayers[2, 93, 42] and 3D bulk tissues[116, 115, 97] are viscoelastic, exhibiting glassy dynamics that indicates they are close to a continuous fluid-

to-solid, or jamming transition. Developing continuum models that incorporate jamming transitions has proven difficult even in non-active materials [37, 123, 51], and so continuum models to date have not included this effect. In addition, although most work has focused on the average material properties of a tissue, many tissues are heterogeneous. Therefore, given the close proximity of a fluid-solid transition where the shear modulus is expected to rise quickly from zero, it is natural to wonder if stiffness gradients within a tissue can drive patterning. There is already some experimental evidence for this; Tambe and coworkers coined the term “plithotaxis” to describe their observation that MDCK cells polarize and move in the direction of local maximal principal stress to minimize local shear[136]. Using a simple model, this phenomena may be understood in terms of the deformations of the underlying actomyosin network[104].

To our knowledge, there are no models that seek to quantify how gradients in stiffness within a tissue drive patterning, or predict the parameters that control patterning in such a system, although there are some analogues that can guide us. For example, in active particle-based models, there is a direct relationship between the packing fraction of particles and the fluidity of the material. This leads to a natural coupling between the polarization (the direction that a particle wants to move) and the packing fraction that can be encapsulated in hydrodynamic models[39, 24] and gives rise to a novel type of patterning called motility induced phase separation. Similarly, in liquid crystals there is a relationship between the nematic order parameter and the molecular mobility[127]. Again, one can write a hydrodynamic model that encapsulates this relationship and predicts pattern formation in liquid crystals.

But what is an appropriate hydrodynamic model for confluent tissues? It is well-established that cells in a tissue can be polarized to move in a particular direction and can coordinate their motion to form a flock[75]. This suggests that a cell polarization field should be incorporated in a continuum model of tissue, in analogy with continuum theories of flocking[144, 45, 87] and particle-based active matter models. But confluent tissues can

change from fluid to solid at a packing fraction of unity, suggesting that density might not be an optimal choice for the hydrodynamic field. As described in Section 1.3.1, a recent body of work based on vertex models at the cellular scale suggests that confluent tissues exhibit a novel type of rigidity transition based on cell shape [38, 126, 17, 16, 18, 94]. Evidence for a similar rigidity transition has also been found in cellular Potts models [46, 59, 26] that may provide an alternate starting point for formulating a continuum theory of tissue.

Therefore, in Section 4.1 of this chapter, we develop a mean-field description of the fluid-solid transition in vertex models that directly incorporates our knowledge from Chapter 2 of how cell shapes govern jamming transitions and tissue stiffness in confluent tissues. It is important to note the distinction between a single-cell shape anisotropy field and an orientation field that captures alignment of elongated cells, first highlighted by Stark and Lubensky [127] for liquid crystals. In inert materials, however, molecular shape fluctuations decay on microscopic time scales and can therefore be neglected in hydrodynamic models. Cells, in contrast, are extended objects that can individually acquire isotropic or anisotropic shapes. Moreover, cellular shape changes have been shown to control the tissue rigidity, driving a continuous transition between liquid-like and solid-like states. Shape fluctuations become long-lived at the transition and their dynamics must be incorporated in a hydrodynamic theory. When elongated, cells can additionally align their orientation and form states with liquid crystalline order. Various shape-driven behavior of epithelial tissues are shown schematically in Fig. (4.1-a). Recent work by Ishihara *et al.* [57], concurrent with our own, also uses vertex model energy for the tissue to construct a continuum theory. This work does not, however, distinguish between a tissue of cells with isotropic mean shape (see Fig.(4.1a-left)) and a tissue of cells that have anisotropic shape on average, but do not exhibit nematic order (see Fig.(4.1a-middle)), as observed in simulations [16, 18, 155]. In the model proposed in Ref. [57] the onset of cell anisotropy is always accompanied by nematic order of elongated cells, which was not observed in the shape-driven solid-liquid transition predicted in Vertex and Voronoi models [16, 18, 155].

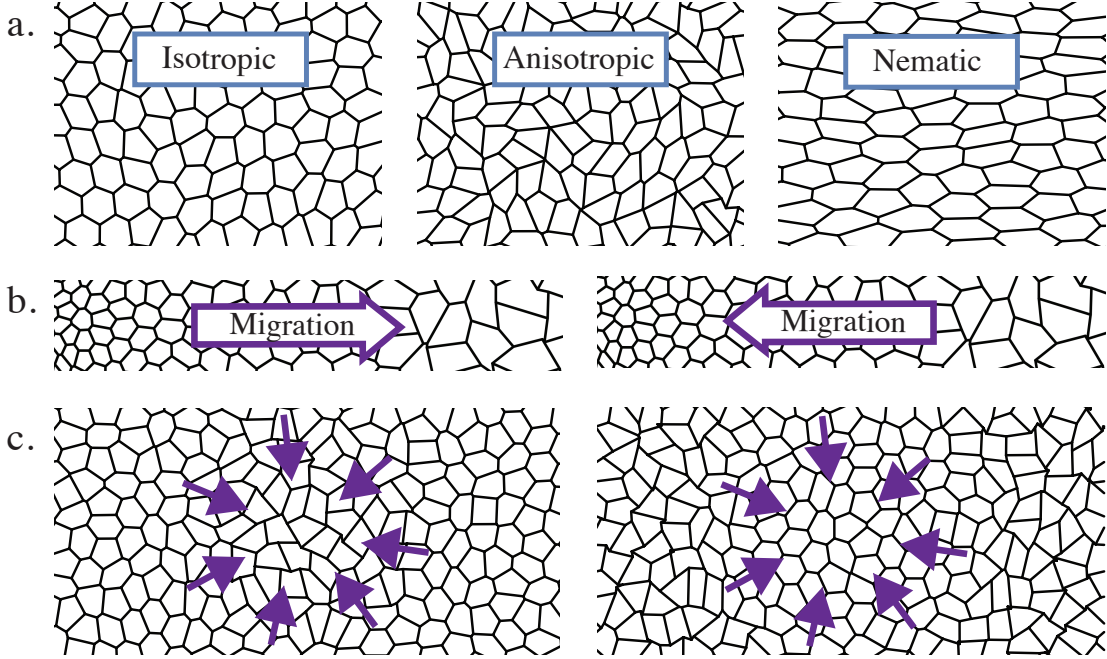


Figure 4.1: Diagrams illustrating various shape-related behaviors in epithelial tissues. **a** From left to right: isotropic cell shapes (solid/jammed state), anisotropic cell shapes (fluid), nematic order of anisotropic cell shapes. **b** and **c** together display the *morphotaxis* properties of the tissue. **b**: Cells may sense local gradients in shape, corresponding to gradients in tissue rigidity, and thereby polarize and migrate towards (left) or away from (right) the more anisotropic cells. **c**: Sinks of polarized motile forces may induce an increase (left) or a decrease (right) in the local cell anisotropy.

In Section 4.2, we present a hydrodynamic model that couples a cell-shape anisotropy order parameter (that describes the tissue shear stiffness) to cell polarization. The hydrodynamic equations incorporate two important effects illustrated in Figs. (4.1-b,4.1-c). The first is a coupling between gradients of tissue rigidity (as embodied by cell shape) and cell polarization through a parameter ν that relates the coordination of cell migration to the mechanical properties of the tissue providing a macroscopic analog of plithotaxis. We take ν to be positive when cells migrate in the direction of stiffer (higher shear modulus) tissue, and negative when the cells migrate in the direction of softer tissue.

The second effect captures how a sink of polarized motile forces affects tissue shape and shear stiffness. Our chosen convention is that if a sink (inward splay of polarization) tends to fluidize the tissue, generating anisotropic shapes (Fig. (4.1-c) left), the coupling param-

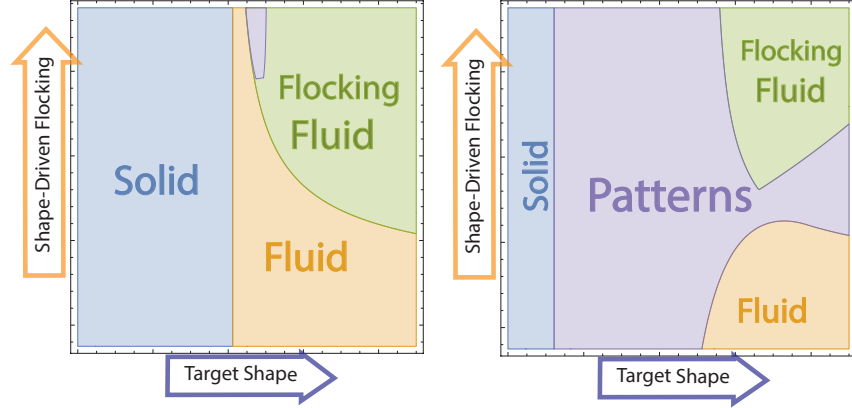


Figure 4.2: Schematic phase diagram comparing negative (left) and positive(right) *morphotaxis* parameters for a shape-based hydrodynamic model where convergent polarization tends to decrease local cell shape anisotropy. The “target shape” axis captures the average cell’s preferred perimeter to area ratio, while the “shape-driven flocking” axis quantifies the degree to which elongated cell shapes promote polarization. The left panel corresponds to tissues in which cells tend to migrate toward fluid-like regions with more shape anisotropy, and the behavior is largely homogeneous. The right panel describes tissues where cells polarize toward solid-like regions of tissue with lower shape anisotropy, and the tissue exhibits patterns like asters or bands in a large region of the phase space.

eter is negative, and positive in the opposite case (Fig. (4.1-c) right). As our analysis will demonstrate, these two effects encapsulate the interaction between polarization and shape and their product controls patterning. Therefore we introduce the new term *morphotaxis* – morpho- from the greek $\mu\rho\rho\phi\acute{\eta}$ meaning form or structure, and -taxis from the greek $\tau\acute{\alpha}\xi\iota\varsigma$. When the morphotaxis parameter is positive, patterns such as asters and traveling bands dominate. In contrast, when the morphotaxis parameter is negative, the tissue response is largely homogeneous.

Our work explores for the first time the hydrodynamics of shape as a property distinct from the orientational order of elongated shapes. It additionally provides perhaps the first continuum description of glassy dynamics in terms of a structural order parameter. While elusive in conventional soft matter systems, a structural signature of the onset of rigidity appears naturally in tissues in terms of cellular shape.

4.1 A mean-field model for 2D shape anisotropy

As described in Section 1.3.1 as well as Chapter 2, the Vertex Model [38, 55, 126] is able to describe the mechanics and dynamics of epithelial tissues from the cellular scale. In this model, cells are represented as polygons which tile the plane. For a two-dimensional tissue containing N cells the inter- and intra-cellular interactions are then captured by a shape energy parametrized in terms of area A_a and perimeter P_a of the a -th cell, given (again) by

$$E_{shape} = \sum_a [\kappa_A (A_a - A_0)^2 + \kappa_P (P_a - P_0)^2] , \quad (4.1)$$

where the sum runs over the N cells in the tissue. As described in Section 1.3.1, the target area A_0 and target perimeter P_0 may be understood in terms of subcellular ingredients. Most notably P_0 arises from the competition between cell-cell adhesions and the tension produced by the cortical actomyosin network.

Numerical studies of the ground states of the shape energy given in Eq. (4.1) have identified a rigidity transition [16, 18, 94] that occurs as a function of the dimensionless “target shape-index” $s_0 = P_0/\sqrt{A_0}$. In previous work, the symbol p_0 was used for this quantity, but we change it here both for consistency with work in 3D [84] and to distinguish it from cell polarization p . When $s_0 < s_0^* \approx 3.81$, cortical tension dominates and the tissue is rigid with finite barriers to cellular rearrangements. For $s_0 > s_0^*$ the energy barriers to cellular rearrangements vanish, resulting in zero-energy deformation modes that enable cells to elongate their shapes and fluidize the tissue. An analysis of cellular shapes reveals that the spatially-averaged cell shape-index $q = \langle P_a/\sqrt{A_a} \rangle$ provides an order parameter for the transition in both non-motile and motile tissues: a tissue with $q < s_0^*$ is a rigid network of roughly regular cell shapes, while a tissue with $q > s_0^*$ is a fluid-like tissue of elongated and irregular cell shapes.

4.1.1 The Shape Tensor

Our first goal is to construct a continuum mean-field model of the rigidity transition captured by the VM. To do this we characterize the shape of the a -th cell via a shape tensor, given by

$$\mathbf{G}^a = \frac{1}{n_a} \sum_{\mu \in a} (\mathbf{r}^\mu - \mathbf{r}^a) \otimes \left(\frac{\mathbf{r}^\mu - \mathbf{r}^a}{|\mathbf{r}^\mu - \mathbf{r}^a|} \right), \quad (4.2)$$

where \mathbf{r}^μ is the position of the μ -th vertex of the a -th cell, \mathbf{r}^a points to the geometric center of cell- a and the sum runs over the n_a vertices on this cell. The cellular shape tensor \mathbf{G}^a is very

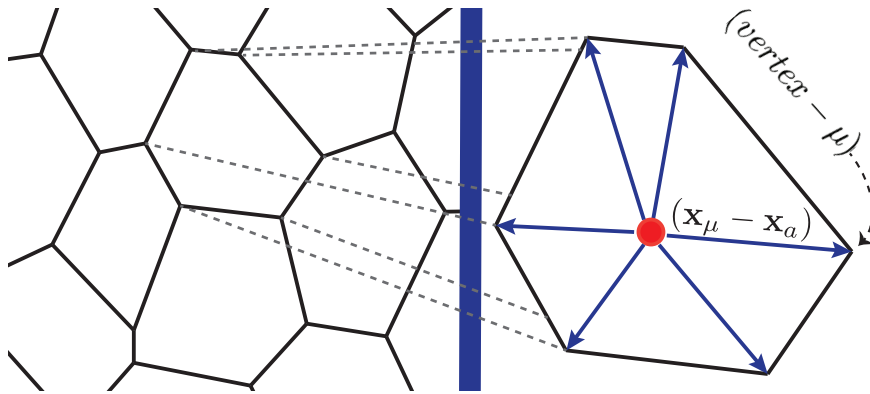


Figure 4.3: Left: The Vertex Model representation of cells in a confluent monolayer. Right: The vectors which are used to create the cellular shape tensor.

similar to the gyration tensor used to characterize the configuration of polymers[34, 117]. To directly connect with area and perimeter, we define the shape tensor with units of length, in contrast to what is done in most previous literature. This choice does not, however, impact our results. Since \mathbf{G}^a is a real and symmetric tensor, it has three independent degrees of freedom in two dimensions, and can generally be written in the form

$$G_{ij}^a = M_a \left[\hat{e}_i^a \hat{e}_j^a - \frac{1}{2} \delta_{ij} \right] + \frac{1}{2} \Gamma_a \delta_{ij}, \quad (4.3)$$

where $M_a = \lambda_1^a - \lambda_2^a > 0$ and $\Gamma_a = \text{Tr}[\mathbf{G}^a] = \lambda_1^a + \lambda_2^a$ are the sum and differences of the eigenvalues $\lambda_{1,2}^a$, $\hat{\mathbf{e}}^a$ is the eigenvector of the largest eigenvalue, λ_1^a , and i, j denote Cartesian components. We introduce the dimensionless parameter $m_a = M_a/\Gamma_a$, which vanishes for

isotropic cells and can be written as

$$m_a = \frac{2}{\Gamma_a} \hat{\mathbf{e}}^a \cdot \mathbf{G}^a \cdot \hat{\mathbf{e}}^a - 1 . \quad (4.4)$$

Note that m_a is chosen to be positive definite. For regular n -sided polygons the shape tensor is always diagonal with $\lambda_1^a = \lambda_2^a$, hence $m_a = 0$. The area A_a and the perimeter P_a can then be expressed in terms of the shape tensor as

$$A_a = 2n_a \sin(2\pi/n_a) \text{Det}[\mathbf{G}^a] , \quad (4.5)$$

$$P_a = 2n_a \sin(\pi/n_a) \text{Tr}[\mathbf{G}^a] . \quad (4.6)$$

It can be shown numerically that these shape relations will hold approximately for small deformations of irregular polygons. To verify the validity of Eqs. (4.5) & (4.6), we have tested these equations by deforming polygons through the application of Gaussian noise to the positions of the vertices of regular polygons of area = 1 . Up to a noise magnitude of 0.2, the shape tensor estimates correlate with the exact values of area and perimeter with a correlation coefficient $r > 0.95$.

4.1.2 Mean-field theory

Our first goal is to re-write the deformation energy of a single cell in terms of the cell shape anisotropy, m_a . This is accomplished using Eqs. (4.5) and (4.6):

$$\epsilon_a = \left[c_1(n_a)(1 - m_a^2)\tilde{\Gamma}_a^2 - 1 \right]^2 + \tilde{\kappa} \left[c_2(n_a)\tilde{\Gamma}_a - s_0 \right]^2 , \quad (4.7)$$

where $c_1(n_a) = \frac{n_a}{2} \sin(2\pi/n_a)$, $c_2(n_a) = 2n_a \sin(\pi/n_a)$ and we have scaled lengths with $\sqrt{A_0}$ and energies with $A_0^2 \kappa_A$ and defined $\tilde{\Gamma}_a = \Gamma_a / \sqrt{A_0}$ and $\tilde{\kappa} = \kappa_P / (A_0 \kappa_A)$.

Now we would like to use this to develop a simple mean-field model that captures the fluid-solid transition we see in metastable states at $s_0^* \approx 3.81$ in the vertex model. From

previous work we expect the transition to be governed by the shape anisotropy m_a , so we minimize (4.7) as function of m_a , keeping $\tilde{\Gamma}_a$ fixed such that $P_a = P_0$. Alternatively, we could have chosen to fix $\text{Det}(\mathbf{G}_a)$ such that $A_a = A_0$, obtaining qualitatively the same results, as shown in Appendix A.1.

The minimal single-cell energy can then be written as a function of cell shape anisotropy as

$$\epsilon_a^{min} = \frac{1}{2}\alpha(s_0, n_a)m_a^2 + \frac{1}{4}\beta(s_0, n_a)m_a^4. \quad (4.8)$$

The parameters α and β are controlled by the target shape parameter s_0 and the polygon degree n_a . While β is positive for all s_0 and n_a , α changes sign as a function of s_0 and n_a . Equation (4.8) has the familiar form of a ϕ^4 theory, changing continuously from a single well to a double well at a critical value $s_0^*(n_a)$, as shown in Fig. (4.4).

Nothing in our analysis so far has specified n_a , the polygon degree, which sets the value of the shape order parameter at the critical point. Previous work on the 2D vertex model has shown that the rigidity transition occurs at $s_0^* \approx 3.81$, which is the shape index corresponding to a regular pentagon. Although pentagons cannot tile space, we can still choose $n_a = 5$ in our mean field model, so that the ground state anisotropy \bar{m} that minimizes Eq. (4.8) transitions from $\bar{m} = 0$ to $\bar{m} > 0$ at the correct value of s_0^* , as shown in the inset to Fig. (4.4). With this choice, α and β are given by

$$\alpha(s_0) = as_0^2 - bs_0^4, \quad (4.9)$$

$$\beta(s_0) = bs_0^4. \quad (4.10)$$

with $a = \text{Cot}(\pi/5)/5$ and $b = [\text{Cot}(\pi/5)]^2/100$. Cell-cell interactions could provide additional constraints not present in Eq. (4.8), which should generally increase the energy of a cell (hence this is a *minimal* energy). Recent work by some of us has also shown that in this model rigidity arises from purely geometric incompatibility[84], even in the absence of topological defects such as T_1 transitions[89].

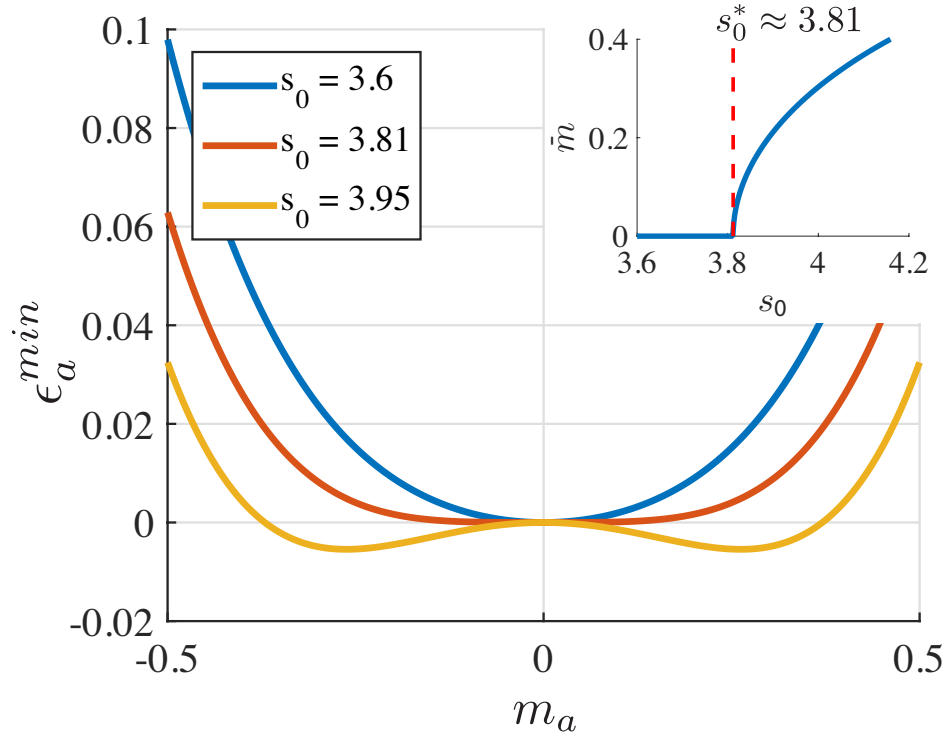


Figure 4.4: Mean-Field tissue energy as a function of shape-anisotropy for various values of the target shape-index s_0 . As this shape index is increased past $s_0^* \approx 3.81$ the energy develops two minima and the anisotropy \bar{m} becomes finite, as shown in the inset.

In summary, we have re-written the vertex model energy functional in terms of the shape anisotropy m of deformed polygons of degree n , minimized with respect to m to find a ground state, and then chosen $n = 5$ so that the ground state switches from isotropic to anisotropic shape at a value of the control parameter that is consistent with simulations of the microscopic model. While the choice $n = 5$ is well motivated, we note that choosing a different value of n (e.g. $n = 6$) will only shift the location of the fluid-solid transition, without impacting the qualitative results of the model.

4.2 Hydrodynamic theory of cellular shape

Guided by the mean-field theory described in the previous section, we now formulate a continuum model of the shape-driven rigidity transition. As previously pointed out in the

context of the Poisson-bracket derivation of the hydrodynamic equations of nematic liquid crystals [127], it is important to distinguish between fluctuations in the shape of individual cells, as quantified by the single-cell anisotropy m_a , and fluctuations in the local alignment of elongated cells that are captured by correlations in the direction $\hat{\mathbf{e}}^a$ of the shape tensor eigenvectors. To our knowledge, a hydrodynamic description of single cell fluctuations has not been explored before. To define continuum fields, it is convenient to introduce the traceless part of the cellular shape tensor, given by

$$\tilde{G}_{ij}^a = G_{ij}^a - \frac{1}{2}\delta_{ij}\Gamma_a = M_a \left[\hat{e}_i^a \hat{e}_j^a - \frac{1}{2}\delta_{ij} \right]. \quad (4.11)$$

Following conventional definitions, we introduce coarse-grained fields, given by

$$\Gamma(\mathbf{r}, t) = \left[\sum_a \Gamma_a \delta(\mathbf{r} - \mathbf{r}^a) \right]_c, \quad (4.12)$$

$$\tilde{G}_{ij}(\vec{x}, t) = \left[\sum_a \tilde{G}_{ij}^a \delta(\mathbf{r} - \mathbf{r}^a) \right]_c, \quad (4.13)$$

where the brackets $[...]_c$ denote coarse-graining and \mathbf{r}^a is the position of the centroid of the a -th polygonal cell. Additionally, the local coarse-grained number density is given by

$$\rho(\mathbf{r}, t) = \left[\sum_a \delta(\mathbf{r} - \mathbf{r}^a) \right]_c. \quad (4.14)$$

For fixed number of cells, i.e., in the absence of cell growth and death, and in systems of fixed total area A_T with periodic boundary conditions, the number density is slaved to cell area. Recent experiments have reported “giant number fluctuations” (GNF) in tissues [42, 157, 158, 43]. One may then expect the dynamics of the number density, ρ , to play a role in tissue stability. GNF have been mainly observed, however, in highly motile, fluid tissue, while in the rigid state the number density seems to remain uniformly high, with minimal fluctuations. We therefore expect that the dynamics of density fluctuations may play an

important role in fluid tissue, but not in the vicinity of the fluid-solid transition. The study of such effects is reserved for future work and in the following we simply equate the density to its mean value $\rho_0 = 1/\bar{A}$, with \bar{A} the mean cell area.

The coarse-grained field $\Gamma(\mathbf{r}, t)$ represents a fluctuating cell perimeter density. If all cell perimeters are identical it will simply be proportional to the number density. The coarse-grained field $\tilde{G}_{ij}(\mathbf{r}, t)$ is a symmetric and traceless tensor of rank two. It has a structure similar to that of the familiar nematic alignment tensor, but it incorporates both fluctuations in individual cell shape and in the direction of the principal eigenvector. To separately quantify cell-shape fluctuations, we define an additional coarse-grained field, the cell-shape anisotropy, as

$$m(\mathbf{r}, t) = \frac{[\sum_a M_a \delta(\mathbf{r} - \mathbf{r}^a)]_c}{\Gamma(\mathbf{r}, t)}. \quad (4.15)$$

The traceless shape tensor is then written as

$$\tilde{G}_{ij}(\mathbf{r}, t) = m(\mathbf{r}, t)\Gamma(\mathbf{r}, t)Q_{ij}(\mathbf{r}, t), \quad (4.16)$$

where

$$Q_{ij}(\mathbf{r}, t) = \frac{\tilde{G}_{ij}(\mathbf{r}, t)}{m(\mathbf{r}, t)\Gamma(\mathbf{r}, t)}. \quad (4.17)$$

is the nematic alignment tensor.

At the single-cell level, the shape tensor G_{ij}^a is characterized by three independent quantities that can be chosen as the cell area (proportional to $\text{Det}(\mathbf{G}^a)$ and inversely proportional to the mean density in a confluent tissue), the cell anisotropy $m_a = M_a/\Gamma_a$, and the angle defined by $\hat{\mathbf{e}}_a$. Then Γ_a , which is proportional to cell perimeter, can be written as $\Gamma_a = c\sqrt{A_a/(1 - m_a^2)} \sim [\rho_0(1 - m_a^2)]^{-1/2}$, with c a numerical constant of order unity. Fluctuations in the field $\Gamma(\mathbf{x}, t)$ will then be controlled by density and shape anisotropy fluctuations, and $\Gamma(\mathbf{r}, t) = \Gamma(\rho(\mathbf{r}, t), m(\mathbf{r}, t)) \simeq \Gamma(\rho_0, m(\mathbf{r}, t))$. In other words, we do not need to consider Γ as an independent field as it is slaved to m .

If cells are isotropic, both m and \tilde{G}_{ij} vanish identically. When cells are elongated and m

is finite, cells can additionally exhibit orientational order captured by the tensor Q_{ij} . For uniaxial systems, Q_{ij} can be written as

$$Q_{ij}(\mathbf{r}, t) = S(\mathbf{r}, t) \left[n_i n_j - \frac{1}{2} \delta_{ij} \right], \quad (4.18)$$

where $\mathbf{n}(\mathbf{r}, t)$ is the nematic director. Tissues of elongated cells with a nonzero mean value of m can then additionally exhibit orientational order of cell elongation characterized by a finite value of $S(\mathbf{r}, t)$. Such nematic order has not, however, been observed in simulations of Active Vertex or Self-Propelled Voronoi models in the absence of interactions that tend to align cell polarization. For this reason we do not consider the dynamics of Q_{ij} here and leave this for future work. As seen below, here we only model tissues where cell elongation may result in polar alignment of cell motility, possibly leading to global flocking of the tissue. This may describe monolayers of MDCK cells as studied by Puliafito *et. al.*[102] that show a strong correlation between cell morphology and the transition between motile and non-motile tissues.

4.2.1 Hydrodynamics of Shape in Non-Motile Tissues

We begin by constructing a hydrodynamic equation for $m(\mathbf{r}, t)$ in the absence of cell motility. Due to the complexity of the interactions arising from the shape energy, an exact coarse graining appears intractable. Instead, we recognize that the simplified mean-field theory of pentagons described in Section 4.1.2 already encodes the key properties of the shape driven liquid-solid transition seen in simulations[16, 18]. At large length scales, we then neglect density fluctuations and assume that the VM can be described by a Landau-type free energy functional given by

$$F = \int d\mathbf{r} \left\{ \frac{1}{2} \alpha(s_0) m^2 + \frac{1}{4} \beta(s_0) m^4 + \frac{D}{2} (\nabla m)^2 \right\}, \quad (4.19)$$

where D is a stiffness that describes the energy cost of spatial variation in cellular shape arising from interactions. Since the rigidity transition is found to be continuous in numerical simulations of Vertex and Voronoi models, and well described by the free energy of Eq. (4.19), we use here the same quadratic energy derived for a single cell as a mean-field description for the tissue. The relaxational dynamics of $m(\mathbf{r}, t)$ is then given by

$$\begin{aligned} \partial_t m &= - \frac{1}{\gamma} \frac{\delta F}{\delta m} \\ &= - [\alpha(s_0) + \beta(s_0)m^2] m + D \nabla^2 m, \end{aligned} \tag{4.20}$$

where for simplicity we have taken the kinetic coefficient $\gamma = 1$. The phenomenological parameters α and β depend on the target shape index s_0 via Eqs.(4.9, 4.10), with $\beta > 0$ and α changing sign at $s_0 = 3.81$. The steady state solution of Eq. (4.20) then yields two homogeneous states: a solid state with $m_{ss} = 0$ for $\alpha > 0$, corresponding to $s_0 < 3.81$, and a liquid state with $m_{ss} = \sqrt{-\alpha/\beta}$ for $\alpha < 0$, corresponding to $s_0 > 3.81$. It therefore provides a mean-field description of the liquid-solid transition seen in the vertex model. The stiffness D tends to stabilize the homogeneous states. Fluctuations are characterized by a correlation length $\ell_m \sim \sqrt{D/|\alpha|}$ that diverges at the transition. In the rest of this work α and β are functions of s_0 even where this dependence is suppressed.

4.2.2 Hydrodynamics of Shape in Motile Tissues

Inspired by the Toner-Tu model of flocking, we describe cell motility at the continuum level in terms of a local polarization field, $\mathbf{p}(\mathbf{r}, t)$, that defines the direction of the propulsive force originating from the traction that cells exert on a substrate. In particle-based flocking models, a mean polarization arises from the explicit tendency of particles to align with their metric neighbors and is thereby tuned by density. In contrast, collective motion in our model is directly tuned by cell shape, which can exhibit slow dynamics at the liquid-solid transition. On the other hand, although cell-shape anisotropy can generate mechanical forces

that build up local polarization, the *direction* of cellular polarization does not in general need not correlate with the orientation of anisotropic cell shapes. As a result, a tissue may be polarized (i.e., $|\mathbf{p}| \neq 0$) even in the absence of nematic order of elongated cell shape (i.e., $\text{Tr}[\mathbf{Q}^2] = 0$). In this work, we ignore the dynamics of Q_{ij} and explore the possibility that structural nematic order of elongated cell shapes and polar alignment of cell polarization be effectively independent. The long time dynamics of the tissue is then described by coupled continuum equations for cell anisotropy and polarization, given by

$$\partial_t m + \nu_1 \mathbf{p} \cdot \nabla m = - [\alpha(s_0) + \beta(s_0)m^2] m + \sigma \nabla \cdot \mathbf{p} + D \nabla^2 m, \quad (4.21)$$

$$\begin{aligned} \partial_t \mathbf{p} + \lambda_1 (\mathbf{p} \cdot \nabla) \mathbf{p} = & - [\alpha_p(m) + \beta_p p^2] \mathbf{p} - \nu \nabla m \\ & + \lambda_2 \nabla p^2 - \lambda_3 (\nabla \cdot \mathbf{p}) \mathbf{p} + D_p \nabla^2 \mathbf{p}. \end{aligned} \quad (4.22)$$

As with all phenomenological hydrodynamic models, Eqs. (4.21) and (4.22) contain quite a few parameters, which can in general be functions of m and p^2 . For simplicity here we take them as constant unless otherwise noted. The cell anisotropy field m is convected by polarization at rate ν_1 and diffuses with diffusivity D . The polarization equation has a form closely analogue to the Toner-Tu equations, with the shape anisotropy m replacing the density, but with the important difference that m is not conserved. The convective parameters λ_1, λ_2 and λ_3 arise from the breaking of Galilean invariance due to the presence of the substrate. For simplicity we neglect the anisotropy of the stiffnesses for bend and splay deformations and assume a single isotropic diffusivity, D_p . The coefficients β (described in Section II) and β_p are both assumed to be positive so the model admits stable anisotropic and flocking states. Both α (introduced in the previous section) and $\alpha_p(m) = \alpha_p^0 - am$ (with $\alpha_p^0, a > 0$) change sign as a function of s_0 , resulting in mean-field transitions and instabilities tuned by the target cell shape s_0 . The choice $a > 0$ describes the possibility that anisotropic cell shapes promote flocking in the fluid, which is a new ingredient of our model. Motivation for such a term comes from the expectation that cell elongation and the associated tissue

fluidity may enhance cell motility, promoting alignment. Since a controls the onset of flocking and its value is not experimentally constrained, we explore the stability of the hydrodynamic model as a function of this parameter. Note that an alternate mechanism for flocking, akin to ones explored in particle-based active matter models, was recently considered in Ref. [44] via a coupling that tends to align the cell polarization with the mean forces due to the cell's neighbors. This alignment mechanism allows for the formation of a flocking solid state that cannot occur in the model presented here, where a finite value of m (hence fluidity) is required for the onset of a polarized state. In fact the alignment with the local force implemented in Ref. [44] even enhances tissue rigidity by suppressing fluctuations transverse to the direction of mean motion. Incorporating such an alignment interaction into our model may require coupling to internal cellular degrees of freedom distinct from shape anisotropy and perhaps also higher order terms. This is left for future work.

There are two key parameters that couple \mathbf{p} and m . The term proportional to σ describes the fact that spatial gradients of polarization can drive changes in local cell shape. A positive value of σ corresponds to a situation where m increases towards regions of positive polarization splay. The sign of this parameter could be determined by correlating TFM measurements of local traction forces with cell shape fluctuations from segmentation images of static tissues. Here we set $\sigma = +1$. The term proportional to ν represents a stiffness gradient driven by cellular shape. Tambe *et. al.* [136] have shown that collective cell migration is directed by gradients in local stress. Since stress transmission is controlled by the mechanical properties of the material, it is then natural to expect that cells may sense gradients in tissue stiffness and this may direct their migration. Wound healing assays in expanding tissues have reported the tendency of MDCK and RPME cells to migrate along directions of minimal shear stresses[136]. This may suggest a tendency to move from the solid to the liquid, corresponding to $\nu < 0$, although other behavior may occur in different cell types. Below we explore our hydrodynamic model for both $\nu = +1$ and $\nu = -1$.

An important difference between the Toner-Tu equations and our model is that cell-shape

Table 4.1: Homogeneous steady states

Phase	Fields	Homogeneous Stability Condition
Solid	$m_{ss} = p_{ss} = 0$	$\alpha > 0, \alpha_p^0 > 0$
Fluid	$m_{ss}^2 = -\frac{\alpha}{\beta}, p_{ss} = 0$	$\alpha < 0, \alpha_p(m_{ss}) > 0$
Flocking Fluid	$m_{ss}^2 = -\frac{\alpha}{\beta}, \beta_p p_{ss}^2 = -\alpha_p(m_{ss})$	$\alpha < 0, \alpha_p(m_{ss}) < 0$

anisotropy m is not a conserved field, but an order parameter associated with a liquid solid transition. Our model couples for the first time collective cell motility with a tissue rigidity transition, allowing us to examine the feedback between motility and shape in a crowded environment.

4.2.3 Homogeneous Steady States

Our hydrodynamic equations for motile tissues exhibit three homogeneous steady state solutions:

(i) a solid with $m_{ss} = p_{ss} = 0$ for $\alpha > 0$ and $\alpha_p^0 > 0$, corresponding to a non-motile rigid tissue with isotropic cellular shapes;

(ii) a non-motile fluid with $m_{ss} = \sqrt{-\alpha/\beta}$ and $p_{ss} = 0$ for $\alpha < 0$ and $\alpha_p(m_{ss}) > 0$, or equivalently $-\beta(\alpha_p^0/a)^2 < \alpha < 0$, corresponding to a liquid-like tissue with elongated cellular shapes and zero mean motion;

and

(iii) a flocking fluid with $m_{ss} = \sqrt{-\frac{\alpha}{\beta}}$ and $p_{ss} = \sqrt{(am_{ss} - \alpha_p^0)/\beta_p}$ for $\alpha < 0$ and $\alpha_p(m_{ss}) < 0$, or equivalently $\alpha < -\beta(\alpha_p^0/a)^2$, corresponding to a liquid-like tissue with elongated cellular shapes and finite mean polarization.

The regions of parameter space where each solution exists are summarized in Table (4.1) and in Fig. (4.5). We find two critical values of $\alpha(s_0)$ in the mean-field phase diagram, corresponding to $\alpha_{c1} = 0$ and $\alpha_{c2} = -\beta(\alpha_p^0/a)^2$. These give two critical lines in the (s_0, a) phase diagram shown in Fig.(4.5), where s_0 is the target shape parameter and a controls elongation-driven collective motility.

Our model yields a density-independent flocking transition in confluent tissues tuned by

cortical tension and cell-cell adhesion, which are captured by the parameter s_0 . The existence of a “flocking solid” state has been prevented by the choice $\alpha_p^0 > 0$.

Our hydrodynamic equations are formally similar to those studied by Yang *et al.* [156] to describe populations of self-propelled entities in the absence of number conservation, with a nonconserved density taking the place of the shape parameter m . This work, in fact, reports static and dynamical patterns qualitatively similar to the ones obtained here. One difference, however, is that the density of self-propelled entities discussed by Yang *et al.* [156] even if not conserved always fluctuates around a finite value, so that small fluctuations can have either sign. Here, the shape parameter m is defined positive and fluctuations in the solid state where $m_{ss} = 0$ can only be positive, describing the occurrence of liquid-like regions in a solid matrix. This impacts the linear stability of these states, as discussed in the next section.

4.2.4 Simplified 1d Model

The hydrodynamic equations (4.21) and (4.22) contain many parameters and the linear stability analysis described in the next section is not transparent. It is therefore instructive to first consider an approximate form of the model that provides useful insight. Retaining only the lowest order couplings between shape parameter and polarization in Eqs. (4.21) and (4.22) and specializing to a one-dimensional system, the dynamics of small deviations from the homogeneous values is governed by

$$\partial_t \delta m = -\tilde{\alpha} \delta m + \sigma \partial_x \delta p_x, \quad (4.23)$$

$$\partial_t \delta p_x = -\tilde{\alpha}_p \delta p_x - \nu \partial_x \delta m \quad (4.24)$$

where $\tilde{\alpha}, \tilde{\alpha}_p > 0$ are effective relaxation rates. At steady state these equations are readily combined into a single equation describing, for instance, spatial variations of the shape

parameter

$$\partial_\tau^2 \delta m = \frac{\tilde{\alpha} \tilde{\alpha}_p}{\sigma \nu} \delta m, \quad (4.25)$$

revealing a characteristic length scale $\ell_c = \sqrt{(|\sigma \nu|)/(\tilde{\alpha} \tilde{\alpha}_p)}$. For $\sigma \nu < 0$, there are no spatially varying solutions that satisfy uniform boundary conditions, suggesting that the homogeneous states are stable, as indeed found below from the analysis of the full equations. For $\sigma \nu > 0$, the system admits wave-like solutions of wavelength $2\pi\ell_c$, which may be excited in the presence of noise. In this case we expect the emergence of spatial patterns, as found below. This simple model also reveals information about the nature of the patterns, specifically that spatial variations of m and p_x are shifted by a quarter of a wavelength. Assuming $\sigma > 0$, for $\nu > 0$, we expect large migratory forces directed from fluid regions toward solid regions of tissue, while these forces will point in the opposite direction for $\nu < 0$. This qualitative picture is confirmed by the simulations of the full model described in Section 4.2.6.

4.2.5 Linear Stability Analysis

Here we examine the linear stability of each of the three homogeneous states against spontaneous fluctuations. After linearizing the hydrodynamic equations (4.21) and (4.22) in the fluctuations of the fields around their steady state values, $\delta m(\mathbf{r}, t) = m(\mathbf{r}, t) - m_{ss}$ and $\delta \mathbf{p}(\mathbf{r}, t) = \mathbf{p}(\mathbf{r}, t) - \mathbf{p}_{ss}$, we expand the fluctuations in Fourier components,

$$\begin{bmatrix} \delta m(\mathbf{r}, t) \\ \delta \mathbf{p}(\mathbf{r}, t) \end{bmatrix} = \int d\mathbf{k} e^{-i\mathbf{k}\cdot\mathbf{r}} \begin{bmatrix} m_{\mathbf{k}}(t) \\ \mathbf{p}_{\mathbf{k}}(t) \end{bmatrix}. \quad (4.26)$$

The linear dynamics of the Fourier components of the fluctuations can then be written in the compact form

$$\partial_t \phi_{\mathbf{k}}(t) = \mathbf{M}^{ss}(\mathbf{k}) \cdot \phi_{\mathbf{k}}(t), \quad (4.27)$$

where $\phi_{\mathbf{k}} = (m_{\mathbf{k}}, \mathbf{p}_{\mathbf{k}})$ and $\mathbf{M}^{ss}(\mathbf{k})$ is a matrix given in Eqs. (A.15) and (A.25) of Appendix A.2.

The decay or growth of the fluctuations is governed by the eigenvalues $z_\mu(\mathbf{k})$ of $\mathbf{M}^{ss}(\mathbf{k})$,

where μ labels the eigenvalue (see Appendix A.2 for details). An instability occurs when $\text{Re}[z_\mu(\mathbf{k})] > 0$ for any (μ, \mathbf{k}) . A nonzero imaginary part of the eigenvalue corresponds to propagating modes.

As we will see below, pattern formation in our model depends crucially on the sign of the product $\sigma\nu$ that defines the morphotaxis parameter of the tissue (or, since we have chosen $\sigma = +1$, the sign of ν) and is best discussed by examining each steady state one at a time. This product combines the response of polarization to gradients in shape with the response of shape to sinks/sources of polarization.

Solid State. The solid state with $m_{ss} = p_{ss} = 0$ exists for $\alpha > 0$. The steady state has no spontaneously broken symmetry and fluctuations are isotropic in the sense that their decay rates only depend on the magnitude of \mathbf{k} , not on its direction. In this case it is convenient to split $\mathbf{p}_\mathbf{k}$ in components longitudinal and transverse to \mathbf{k} as $\mathbf{p}_\mathbf{k} = (p_\mathbf{k}^L, p_\mathbf{k}^T)$, where $p_\mathbf{k}^L = \hat{\mathbf{k}} \cdot \mathbf{p}_\mathbf{k}$ and $\mathbf{p}_\mathbf{k}^T = \mathbf{p}_\mathbf{k} - \hat{\mathbf{k}}p_\mathbf{k}^L$, with $\hat{\mathbf{k}} = \mathbf{k}/|\mathbf{k}|$. Fluctuations in the transverse part of the polarization that corresponds to bend deformations are decoupled and always decay. The coupled dynamics of fluctuations in shape anisotropy and $p_\mathbf{k}^L$ that describes splay deformation is controlled by two eigenvalues, given by

$$z_\pm^{(solid)} = -\frac{1}{2} [\alpha + \alpha_p^0 + (D + D_p)k^2] \pm \frac{1}{2} \sqrt{[\alpha - \alpha_p^0 + (D - D_p)k^2]^2 + 4k^2\nu\sigma}. \quad (4.28)$$

The modes are always stable for $\sigma\nu < 0$. When $\sigma\nu > 0$ the mode $z_+^{(solid)}$ can become positive and yield an instability when $\sigma\nu > [\sqrt{\alpha_p^0 D} + \sqrt{\alpha D_p}]^2$. This condition is, however, obtained by relinquishing the constraint that $m > 0$ and allowing it to fluctuate freely around $m_{ss} = 0$. Imposing the constraint of positive m renormalizes the stability boundary. Lacking an analytic tool, the analysis must, however, be carried out numerically.

The wavelength of the fastest growing mode defines a characteristic length scale given by

$$\ell_{solid} = 2\pi \sqrt{\frac{2DD_p}{\sigma\nu - \alpha_p^0 D - \alpha D_p}}. \quad (4.29)$$

At the onset of instability this becomes $\ell_{solid} = 2\pi(DD_p/\alpha\alpha_p^0)^{1/4}$ and can be interpreted as the geometric mean of two length scales, $\ell_{solid} = 2\pi\sqrt{\ell_m\ell_p}$, where $\ell_m = \sqrt{D/\alpha}$ represents the distance over which diffusion balances the relaxation of the anisotropy field, while $\ell_p = \sqrt{D_p/\alpha_p^0}$ describes spatial variation in the polarization field.

Fluid state. The non-polarized fluid state is obtained for $\alpha < 0$ and $\alpha_p = \alpha_p(m_{ss}) > 0$ and has finite $m_{ss} = \sqrt{-\alpha/\beta}$ and $p_{ss} = 0$. The behavior is formally the same as obtained for the solid state, but with the relaxation rate of the anisotropy parameter m replaced by $-2\alpha > 0$ and that of polarization decreased from α_p^0 to $\alpha_p = \alpha_p^0 - am_{ss} = \alpha_p^0 - a\sqrt{-\alpha/\beta} > 0$. The steady state is again isotropic and fluctuations in the transverse polarization $\mathbf{p}_{\mathbf{k}}^T$ are decoupled and always decaying. The coupled dynamics of fluctuations in shape and splay polarization is controlled by the eigenvalues

$$z_{\pm}^{(fluid)} = -\frac{1}{2} [2|\alpha| + \alpha_p + (D + D_p)k^2] \pm \frac{1}{2} \sqrt{[2|\alpha| - \alpha_p + (D - D_p)k^2]^2 + 4k^2\nu\sigma}. \quad (4.30)$$

Again the steady state is stable when $\sigma\nu < 0$ and unstable for $\sigma\nu > [\sqrt{\alpha_p D} + \sqrt{2|\alpha|D_p}]^2$.

The wavelength of the fastest growing mode is

$$\ell_{fluid} = 2\pi \sqrt{\frac{2DD_p}{\sigma\nu - \alpha_p D - 2|\alpha|D_p}} \quad (4.31)$$

that reduces to $\ell_{fluid} = 2\pi(DD_p/2|\alpha|\alpha_p)^{1/4}$ at the onset of the instability. Note, however, that α_p vanishes at $|\alpha_{c2}| = (\alpha_p^0/a)^2\beta$ where the system undergoes a mean-field transition to a flocking liquid state and ℓ_{fluid} diverges.

Flocking fluid. In the flocking fluid state, obtained for $\alpha < \alpha_{c2}$, the system acquires a finite mean polarization, breaking rotational symmetry, and all modes are coupled. We then choose the x axis along the direction of broken symmetry, i.e., $\mathbf{p}_{ss} = p_{ss}\hat{\mathbf{x}}$. For simplicity we only examine here the behavior of the fluctuations for wavevectors parallel and perpendicular to the direction of broken symmetry. For wavevector \mathbf{k} along the direction of broken symmetry, $\mathbf{k} = k\hat{\mathbf{x}}$, *bending* fluctuations in the orientation of polarization, $\delta p_{\mathbf{k}}^y$, decouple and are always stable. Fluctuations in shape anisotropy and the magnitude of polarization, $\delta p_{\mathbf{k}}^x$, are coupled and the stability is controlled by the eigenvalues

$$\begin{aligned}
2z_{\pm}^{(band)} &= 2(\alpha + \alpha_p(m_{ss})) + ip_{ss}(\nu_1 + \lambda_T)k - (D + D_p)k^2 \\
&\pm \left[\left[2(\alpha - \alpha_p(m_{ss})) + ip_{ss}(\nu_1 - \lambda_T)k - (D - D_p)k^2 \right]^2 \right. \\
&\quad \left. + 4\sigma(\nu k^2 - ikap_{ss}) \right]^{1/2}
\end{aligned} \tag{4.32}$$

where $\lambda_T = \lambda_1 + \lambda_3 - 2\lambda_2$. In this case the sign of the real part of the modes was examined numerically. We find an instability close to the mean-field transition line in a range of wavevectors along the direction of broken symmetry, analogous to the banding instability of Toner-Tu models[15, 87]. Near the mean field transition, the banding instability occurs in a narrow region of s_0 for $\sigma\nu > 2|\alpha|D_p > 0$ and is absent when $\sigma\nu < 0$. A numerical solution of the nonlinear equations reveals, however, a narrow region of banding instability even for $\sigma\nu < 0$. The sign of the morphotaxis parameter $\sigma\nu$ additionally affects the morphology of these banded states (see Fig. (4.5C,4.5D)).

Next we examine the stability of the ordered state deep in the flocking regime. In this case fluctuations in the magnitude of polarization, $\delta p_{\mathbf{k}}^x$, decay on microscopic time scales and can be eliminated by neglecting $\partial_t \delta p_{\mathbf{k}}^x$ in Eq. (4.27). We then obtain coupled equations for fluctuations in cell shape and direction of orientational order. The latter are long-lived at long wavelength because they represent the Goldstone mode associated with the spontaneously

broken orientational symmetry. The full decay rates are shown in Appendix A.2.4. We examine the stability by carrying out a small wavevector expansion of the hydrodynamic modes. For $\mathbf{k} = k\hat{\mathbf{x}}$, corresponding to bend deformation, the homogeneous state is always stable. For $\mathbf{k} = k\hat{\mathbf{y}}$, coupled splay and shape fluctuations become unstable for

$$\sigma\nu > \frac{\sigma\lambda_2 a}{\beta_p} + 2|\alpha| \left(D_p - \frac{\lambda_2\lambda_3}{\beta_p} \right). \quad (4.33)$$

Unlike the corresponding instability obtained in the Toner-Tu model[87], this instability persists even when the advective nonlinearities proportional to λ_2 and λ_3 are neglected.

4.2.6 Numerical simulations

We have solved numerically the full nonlinear hydrodynamic equations (Eqs. (4.21,4.22)) on a periodic grid using a standard RK4 explicit iterative method. We choose a timestep $\Delta t = 0.005$ and grid spacing $\Delta x = 0.1$ to satisfy the Von Neumann stability condition. Simulations are initialized in the appropriate homogeneous state (Table.(4.1)) with superimposed spatially white noise of variance small compared to all equation parameters. To quantify the onset of spatial patterns, we examine the Fourier spectrum of the configurations obtained at long times. If the integral of the discrete Fourier transform of the deviations of the m -field from its mean value is greater than some small cutoff number, then the corresponding state is identified as patterned in Fig.(4.5). Because the perturbations are small, we expect these numerics to agree with and reinforce our analytic phase diagram.

As shown in Fig. (4.5) the numerical results agree well with those of the linear stability analysis. For $\nu < 0$ (Fig. (4.5) top left) the homogeneous states are stable in most of parameter space, with patterns emerging only in a narrow banding region. In contrast, for $\nu > 0$ (Fig. (4.5) bottom left) we obtain a variety of emergent patterns, as expected from the linear stability analysis. As anticipated in Sec. 4.2.5, the stability boundary of the $\nu = 1$ homogeneous solid is shifted as compared to the analytic prediction (i.e. there

are blue circles denoting numerical observations of homogeneous states in the region linear stability analysis suggests should be unstable). This is due to the $m > 0$ restriction used in the numerics but not in the linear analysis, which prevents some instabilities from arising. Reassuringly, we find that relaxing this constraint in simulations resolves the discrepancy and yields agreement with the analytics.

The simulations also reveal the structure of the spatial patterns that replace the uniform states. Examples are shown in Fig. (4.5). For $\nu = 1$, in the solid phase we find droplets of fluid asters surrounded by solid tissue with a positively splayed polarization field (frame A). As s_0 increases, the asters become more closely spaced, and elongated inclusions begin to appear. Past the transition from the solid into the liquid, these patterns invert and we find clusters of solid tissue surrounded by fluid, with the polarization now pointing inward, corresponding to negative splay (frame B). In the banding region we observe elongated regions of fluid tissue, with outward pointing polarization (frame C). Because of the symmetry of the polarization in these bands, the structures do not migrate and their dynamics is reminiscent of coalescence. The banding patterns obtained for $\nu = -1$ are qualitatively different, as shown in Fig. (4.5D). In this case we obtain alternating solid/fluid traveling bands with the polarization aligned transverse to bands. The direction of motion of the band is opposite to that direction of the net polarization, which is reminiscent of a “traffic wave” phenomenon.

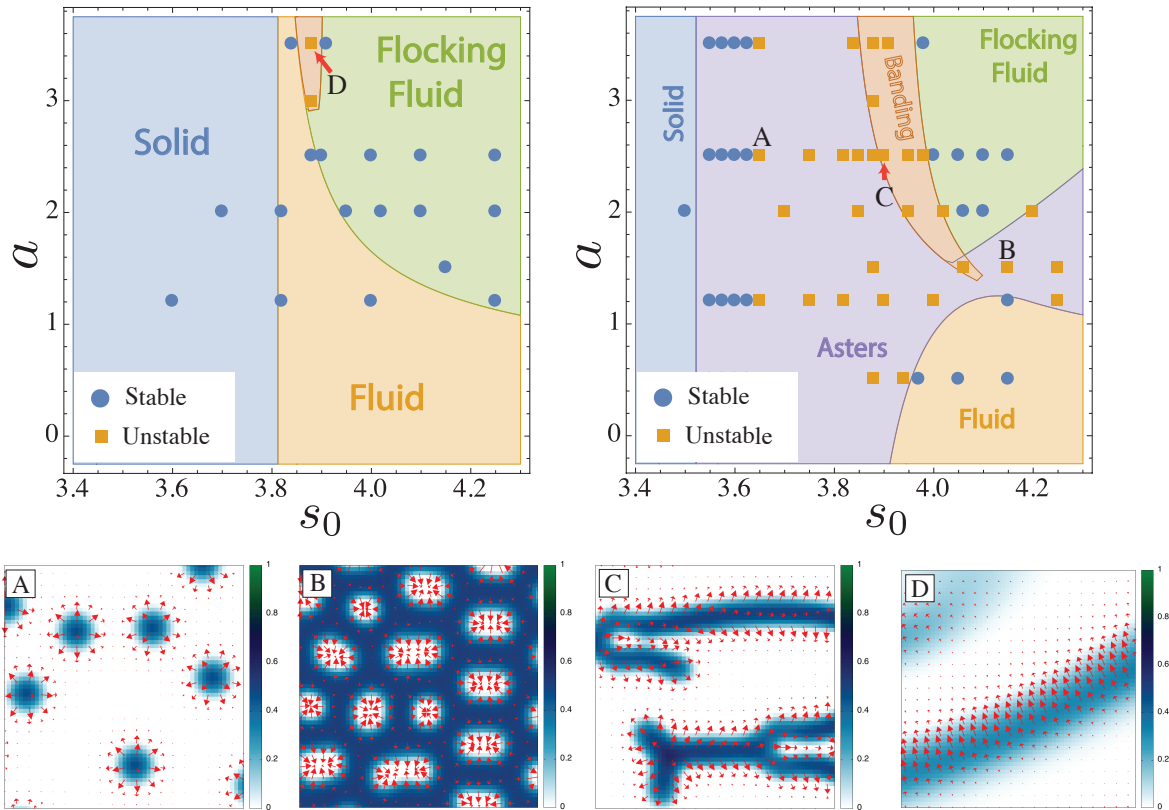


Figure 4.5: Phase diagrams and simulation results in the $s_0 - a$ plane. As in the legend, blue circles represent simulations in which the fields relax to their homogeneous steady state solution. Orange squares represent simulations in which patterns are found to emerge. Here we compare the cases $\nu = -1$ (Top-Left) and $\nu = 1$ (Top-Right) to show the qualitative change induced by this plithotactic parameter. Bottom: Snapshots of different types of emergent patterns from tissue simulations. Colorbars represent the magnitude of local anisotropy (m) while red arrows represent local cell polarization (\mathbf{p}). (A): Sparse aster-like islands of anisotropic cells emerge near the onset of instability in the solid phase. (B): shows an example of “solid” islands arising in the flocking fluid phase due to a splay instability and preventing collective motion. (C) shows the elongated structures resultant from banding instability for $\nu = 1$ while (D) shows the qualitatively different band structures for $\nu = -1$.

Chapter 5

Discussion

We have investigated the consequences of “active” driving forces on the dynamical behavior of cells in epithelial tissues using both simulations and theory. Our investigations are guided by the overarching question: How might evolution control and take advantage of tissue rheological properties in the designing and maintenance of organisms? Using a modification of the vertex model, we investigated the influence of two kinds of active processes on the tissue rigidity: the self-propulsive forces that cells generate by exerting tractions on a substrate and the strains produced by cell division and programmed cell death. We quantify the role of such active forces in controlling tissue rheology. We then examine the interplay between tissue rigidity and cell motility using a hydrodynamic model and identify a novel mechanism for the formation of patterns in development. We summarize the results of each of these efforts below and conclude with some remarks on future directions of investigation of developmental dynamics in tissues.

Cell motility may fluidize tissues. To study the influence of propulsive forces on the rheological state of tissue, we have developed a new Active Vertex Model (AVM). This model generalizes the Vertex Model framework to incorporate cell motility. While other models of confluent motile tissues have recently been developed, such as the Self Propelled Voronoi model [18, 85], this is the first instance that preserves the freedom of cell shape associated

with treating the cell vertices as the degrees of freedom.

In Chapter 2, we show that this new model reproduces the results of the SPV model. As found previously by Bi *et. al.* [18], we locate “glassy” states where cells are stuck in cages and exhibit sub-diffusive mean square displacements. The transition from a fluid-like state to a solid-like state is achieved either by decreasing the propulsive forces, or by increasing the effective cell-cell interfacial tension. This interfacial tension has been previously shown [38, 17] to emerge from the competition between cell-cell adhesions and the active tension generated in the cortical actomyosin gel. These control parameters are suggestive of biological “dials” which tissues may use to self-regulate their rheology.

This tissue rigidity transition is reflected in the shapes of the tissue cells. We show for our model, that a dimensionless cellular “shape-index” is correlated with the ability of cells to escape their cages. This correspondence is not as sharp as in the case of the SPV, where the average shape index transitions past a special value exactly where the effective diffusivity becomes negligibly small [18]. However, in the AVM cell shape and tissue rigidity are nonetheless highly correlated, suggesting a structural order parameter for tissue glassiness.

Mitosis and apoptosis may fluidize tissues We then extended the AVM to investigate the influence of cell death and cell division on tissue rheology. Our investigation is guided by the expectation that the rate of cell division and death will compete with the “bare” uncaging rate of the AVM identified in Chapter 2 to determine the tissue dynamics. This simple picture allows us to identify evidence of glassy states (defined as states where particles exhibit sub-diffusive behavior) even at finite rates of apoptosis and mitosis, where another investigation suggested they should not exist [81]. This appears to resolve a standing discrepancy between experiments and theory. While cell division and death events will generally lead to diffusive fluid-like behavior on the longest timescales, subdiffusive behavior is observed on intermediate timescales when the cell division rate and bare uncaging rate are

slow enough. These tissues are analogous to a supercooled fluid and are thereby expected to behave rigidly on all but the longest timescales.

We further characterized the spatial distribution of cell displacements in the vicinity of each individual mitosis and apoptosis event. As expected from previous work for the case of area-preserving deformations [103], we have identified an average displacement field that matches the one obtained from elasticity theory, as well as “non-affine” displacements that capture noise. The elastic affine response decays spatially as $1/r$, with a magnitude that does not depend significantly on tissue rheology. The non-affine displacements, in contrast, have both a magnitude and spatial extent that varies with rheological tuning parameters, such as cell interfacial tension. Specifically, mitosis and apoptosis events generate longer ranged deformations in rigid tissues than in fluid ones.

Using the calculated affine and non-affine displacements resulting from these division and death events, we assess the relative importance of motile forces versus division and death in the tissue dynamics. This guides our search for a scaling collapse of rheological data across a range of parameters. While the results suggest a universal behavior in the crossover from tissues which are effectively unaffected by cell division & death to tissues where these events will dominate, the data do not fully collapse onto a single curve. The remaining spread in the data may be indicative of a few different effects: (1) that the displacements produced by cell division and by cell death events are not independent, but interfere and correlate with one another in time and space, (2) that the tissue structural relaxation rate cannot be expressed simply as a sum of relaxation rates from separate sources of activity or (3) that cell division and death produce a structural change in a tissue, altering the role of motile forces in fluidizing the tissue. In our future investigations, we will attempt to parse and quantify these effects.

Hydrodynamics of motile tissues In Chapter 4 we develop a hydrodynamic theory for confluent tissue close to this shape-based rigidity transition. The hydrodynamic equations

are formulated in terms of a scalar field that quantifies single-cell anisotropy and a cell polarization field. Cell anisotropy can drive alignment of local polarization, resulting in a flocking liquid state. The interplay of cell shape and polarization additionally drives the organization of a variety of aster and banding patterns consisting of solid tissue inclusions in a liquid matrix or liquid inclusions in the solid, with associated polarization patterns.

Since cell anisotropy is effectively a measure of the rheological properties of the tissue, with isotropic cell shapes identifying the solid or jammed state and anisotropic shapes corresponding to a liquid, variations in cell shape anisotropy are directly associated with variation in the rheological properties of the tissue. Our work therefore quantifies for the first time the role of gradients in tissue stiffness in driving morphological patterns. This is achieved through a morphotaxis parameter that couples polarization to gradients of cell shape anisotropy. Tambe *et al.* [136] used the name “plithotaxis” to describe the observed tendency of cells to move in the direction that minimizes local shear stresses. The parameter ν in our equations could be related to such a plithotactic effect as it embodies the transmission of positional sensing in collective cell migrations via gradient in local tissue rigidity arising from variations in cell shape (see the term $\nu\nabla m$ in Eq. (4.22)). Patterning in our model is controlled, however, by the combined action of this term and the changes in local cell shapes induced by polarization sinks and sources (the term $\sigma\nabla \cdot \mathbf{p}$ in Eq. (4.21)). These two effects together define the “morphotaxis” properties of the tissue. Our work therefore provides a complementary, purely mechanical view to how patterns of growth and differentiation may be specified in development and tissue regeneration. Our results could be tested in experiments by combining segmented cell images with traction force microscopy and particle image velocimetry. In solid regions, where cell migration is strongly suppressed, traction forces provide a direct measure of local cell polarization. Correlating traction measurements with cell shapes could therefore provide information on the sign of the morphotaxis parameter.

Once elongated, cells can also align their orientations and exhibit nematic order on tissue

scales, an effect not included in our work. Nematic order has been observed for instance in mouse fibroblasts and can be enhanced by confinement [33]. Recent work has also established an intriguing connection between topological defects in nematic tissue and cell extrusion and death [114, 62]. Work concurrent to ours by Ishihara *et. al.* [57] has examined the interplay of nematic alignment of elongated cells with tissue mechanical properties and active contraction-elongation. This is accomplished with a continuum model that, although similar in spirit to ours, does not highlight the important distinction between cell anisotropy and nematic order that allows for the onset of polarized states even in the absence of nematic alignment of cell shape, as seen in simulations of self-propelled Voronoi models. Further work will be needed to examine the interplay between cell shape, polarization and nematic order, as well as the role of cell growth, in driving tissue patterning.

Another open question is the role of number density fluctuations, that can be very large in highly motile, fluid tissue, as recently observed in experiments [42, 157, 158, 43]. Extending our work to include variations in number density will require understanding the density dependence of the tuning parameters of the model, such as the cells target perimeter and area, P_0 and A_0 . This is a challenging problem and is left for future investigation.

Open Questions. It will be interesting to explore in more details the interplay between different flocking mechanisms. In particular, recent work by some of us has implemented an explicit alignment interaction of the cell polarization with the local force due to the neighbors and found that this alignment mechanism promotes solidification and allows for a solid flocking state not present in the model considered here [44]. In contrast, in the present model polar order is driven directly by cell shape anisotropy, hence requires tissue fluidity, which in turn enhances coordinated cell migration. These two mechanisms may generally be both at play in living tissue, but further work is needed to understand how they may compete to control the tissue rheology.

The patterns obtained here are not uncommon in developmental biology. The polariza-

tion sinks found in our model imply a local tissue compression that may lead to buckling such as that seen in the apical constriction and invagination of the *Drosophila* embryo[78]. Similar developmental patterns are zebrafish stripes[154], hair follicles[122], evenly spaced feathers in the chicken embryo[58], and branching during lung development[29]. These are more commonly understood as biochemical in origin and modeled through reaction-diffusion equations and Turing-type models[146, 68]. Our work suggests an alternative or complementary purely mechanical mechanism for tissue sorting and pattern formation that may be at play in many of these examples.

Appendix A

Appendices

A.1 Anisotropic Perturbation of the Shape Tensor

We describe here two ways in which the shape energy of an irregular polygon may be obtained as a perturbation of that of a regular one. In this section we work at the single-cell level and for convenience suppress the cell label a . Using the definition given in Eq. (4.2), the shape tensor \mathbf{G}^{reg} of a regular polygon is diagonal and has a single eigenvalue λ , i.e., it takes the form

$$\mathbf{G}^{reg} = \lambda \begin{bmatrix} 1 & 0 \\ 0 & 1 \end{bmatrix} = \frac{\text{Tr}\mathbf{G}^{reg}}{2} \begin{bmatrix} 1 & 0 \\ 0 & 1 \end{bmatrix}. \quad (\text{A.1})$$

We are interested in the form that the tensor takes when perturbed away from this initial reference state. As we will only be concerned with quantities constructed from the eigenvalues of this tensor, we may choose to consider the perturbed tensor in a reference frame in which it is diagonal. The perturbed shape tensor can then be written as

$$\mathbf{G}^{diag} = \frac{\text{Tr}\mathbf{G}^{reg} + \Delta}{2} \left(\begin{bmatrix} 1 & 0 \\ 0 & 1 \end{bmatrix} + m \begin{bmatrix} 1 & 0 \\ 0 & -1 \end{bmatrix} \right), \quad (\text{A.2})$$

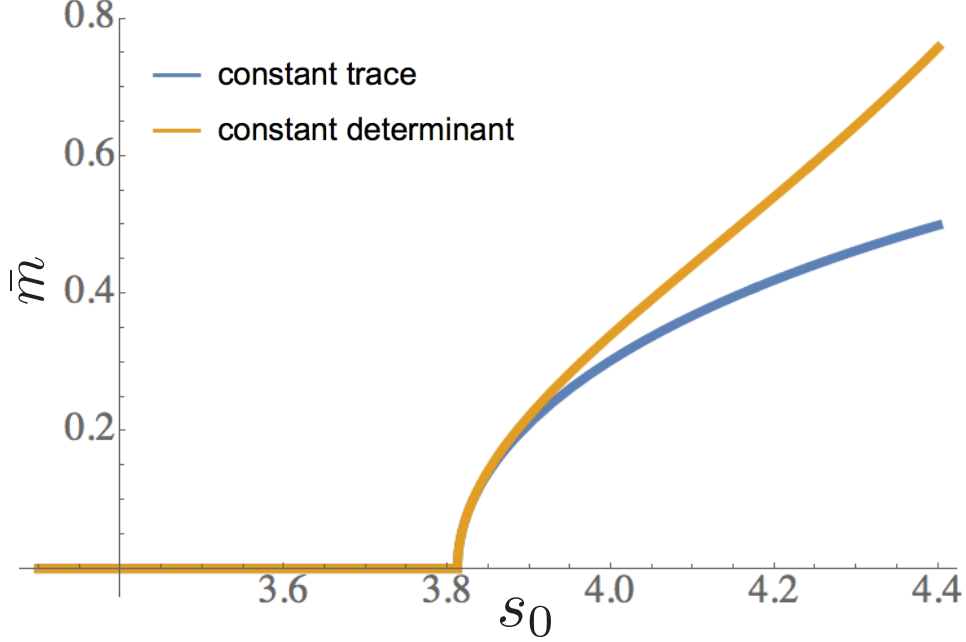


Figure A.1: The mean value \bar{m} of the order-parameter obtained by minimizing the single-cell free energy derived using different geometric perturbations of the energy of a regular pentagon.

where Δ is the change in the tensor trace due to the perturbation. Our choice of the function Δ will constrain our perturbation to a subset of possible trajectories. Our goal is to show that the choice of this function (within reasonable bounds) is not consequential, and therefore that we may consider the energy in terms of the anisotropy m alone. Employing the Area and Perimeter relations (Eqs.(4.5,4.6)), the dimensionless vertex model energy for a single cell can be rewritten in terms of Δ and m as

$$\begin{aligned} \epsilon = & \left[\frac{n}{2} \sin(2\pi/n)(1 - m^2) \left(\tilde{\text{Tr}}[\mathbf{G}^{reg}] + \tilde{\Delta}(m) \right)^2 - 1 \right]^2 \\ & + \bar{\kappa} \left[2n \sin(\pi/n) \left(\tilde{\text{Tr}}[\mathbf{G}^{reg}] + \tilde{\Delta}(m) \right) - s_0 \right]^2, \end{aligned} \quad (\text{A.3})$$

where $\tilde{\text{Tr}}[\mathbf{G}^{reg}] = \text{Tr}[\mathbf{G}^{reg}]/\sqrt{A_0}$ and $\tilde{\Delta}(m) = \Delta(m)/\sqrt{A_0}$ are dimensionless quantities.

We first explore the choice $\tilde{\Delta}(m) = 0$ that corresponds to a perturbation with constant

trace, hence constant perimeter. In this case the cell energy becomes

$$\epsilon = \frac{1}{2}\alpha^{(tr)}(\tilde{\text{Tr}}\mathbf{G}^{reg})m^2 + \frac{1}{4}\beta^{(tr)}(\tilde{\text{Tr}}\mathbf{G}^{reg})m^4, \quad (\text{A.4})$$

with

$$\begin{aligned} \alpha^{(tr)}(\tilde{\text{Tr}}\mathbf{G}^{reg}) &= 2n \sin(2\pi/n)(\tilde{\text{Tr}}\mathbf{G}^{reg})^2 \\ &\quad - n^2 \sin^2(2\pi/n)(\tilde{\text{Tr}}\mathbf{G}^{reg})^4, \end{aligned} \quad (\text{A.5})$$

$$\beta^{(tr)}(\tilde{\text{Tr}}\mathbf{G}^{reg}) = n^2 \sin^2(2\pi/n)(\tilde{\text{Tr}}\mathbf{G}^{reg})^4, \quad (\text{A.6})$$

where we have shifted the energy by an overall constant, independent of m . Eqs. (4.9) & (4.10) may now be recovered from the above by setting $\tilde{\text{Tr}}\mathbf{G}^{reg} = s_0(2n \sin \pi/n)^{-1}$, or equivalently $P = P_0$.

An alternative approach consists of perturbing \mathbf{G}^{reg} while keeping its determinant constant, implying constant area. The $\tilde{\Delta}(m)$ that preserves this condition is given by

$$\tilde{\Delta}(m) = \tilde{\text{Tr}}[\mathbf{G}^{reg}] \left(\frac{1}{\sqrt{1-m^2}} - 1 \right). \quad (\text{A.7})$$

Using this, the single-cell energy may be written in terms of m and the fixed (dimensionless) area \tilde{A} . This energy has the same form as given in Eq. (A.4), but with coefficients now given by

$$\alpha^{(det)}(s_0) = \tilde{\kappa}\tilde{A} \left[8n \tan \frac{\pi}{n} - 4 \frac{s_0}{\sqrt{\tilde{A}}} \sqrt{n \tan \frac{\pi}{n}} \right], \quad (\text{A.8})$$

and

$$\beta^{(det)}(s_0) = \tilde{\kappa}\tilde{A} \left[16n \tan \frac{\pi}{n} - 6 \frac{s_0}{\sqrt{\tilde{A}}} \sqrt{n \tan \frac{\pi}{n}} \right]. \quad (\text{A.9})$$

Because this energy corresponds to a free cell, the fixed area is expected to realize the target area which implies $\tilde{A} = 1$.

The value \bar{m} of m that minimizes the single-cell energy (A.4) for $\alpha < 0$ is $\bar{m} = \sqrt{-\alpha/\beta}$,

where α and β are given by Eqs (4.9,4.10) or by Eqs. (A.8,A.9) for each of the two perturbations used. The dependence of \bar{m} on s_0 for pentagonal cells ($n = 5$) obtained using the two perturbations shown in Fig. (A.1) demonstrates that the behavior does not depend on the perturbation near the transition, which is the region of interest in our work. In the main text we use the results obtained with the perturbation that keeps the trace constant.

A.2 Linear Stability Analysis

The stability analysis follows a well-known procedure. We consider the equations

$$\begin{aligned} \partial_t m + \nu_1 \mathbf{p} \cdot \nabla m + \nu_2 m \nabla \cdot \mathbf{p} = & - [\alpha(s_0) + \beta(s_0)m^2] m \\ & + \sigma \nabla \cdot \mathbf{p} + D \nabla^2 m, \end{aligned} \quad (\text{A.10})$$

and

$$\begin{aligned} \partial_t \mathbf{p} + \lambda_1 (\mathbf{p} \cdot \nabla) \mathbf{p} = & - [\alpha_p - am + \beta_p p^2] \mathbf{p} \\ & - \nu \nabla m + \lambda_2 \nabla p^2 - \lambda_3 (\nabla \cdot \mathbf{p}) \mathbf{p} + D_p \nabla^2 \mathbf{p}, \end{aligned} \quad (\text{A.11})$$

where we have included the ν_2 term for generality. To recover the results of the main text, one needs only to set $\nu_2 = 0$ in the following equations. Equations (A.10,A.11) have the uniform, steady state solutions (m_{ss}, \mathbf{p}_{ss}) enumerated in Table.(4.1). There are two types of solutions: stationary or non-polarized ones with $|\mathbf{p}_{ss}| = 0$ (a fluid and a solid) and moving or polarized ones with $|\mathbf{p}_{ss}| \neq 0$ (flocking fluid). To evaluate the stability of these steady states, we perturb the steady state solutions ($m \rightarrow m_{ss} + \delta m, \mathbf{p} \rightarrow \mathbf{p}_{ss} + \delta \mathbf{p}$) and examine the linear dynamics of the fluctuations (A.10,A.11). By introducing Fourier transforms, the linear equations for the fluctuations can be written as

$$\partial_t \begin{bmatrix} m_{\mathbf{k}}(t) \\ p_{\mathbf{k}}^x(t) \\ p_{\mathbf{k}}^y(t) \end{bmatrix} = \mathbf{M}(\mathbf{k}) \begin{bmatrix} m_{\mathbf{k}}(t) \\ p_{\mathbf{k}}^x(t) \\ p_{\mathbf{k}}^y(t) \end{bmatrix}, \quad (\text{A.12})$$

where

$$\begin{bmatrix} m_{\mathbf{k}}(t) \\ p_{\mathbf{k}}^x(t) \\ p_{\mathbf{k}}^y(t) \end{bmatrix} = \int \frac{d\mathbf{r}}{(2\pi)^2} e^{i\mathbf{k}\cdot\mathbf{r}} \begin{bmatrix} \delta m(\mathbf{r}, t) \\ \delta p^x(\mathbf{r}, t) \\ \delta p^y(\mathbf{r}, t) \end{bmatrix} \quad (\text{A.13})$$

are the Fourier amplitudes and the explicit expression of the matrix $\mathbf{M}(\mathbf{k})$ depends on the homogenous state considered. We seek solutions of the form

$$(m_{\mathbf{k}}(t), p_{\mathbf{k}}^x(t), p_{\mathbf{k}}^y(t)) = \exp(zt)(m_{\mathbf{k}}, p_{\mathbf{k}}^x, p_{\mathbf{k}}^y). \quad (\text{A.14})$$

The eigenvalues of $\mathbf{M}(\mathbf{k})$ then represent the growth rates of the perturbations.

A homogeneous state is then linearly stable iff the real part of each eigenvalue of $\mathbf{M}(\mathbf{k})$ is negative for all \mathbf{k} . With this condition satisfied, all small perturbations decay in time and the system returns to the steady state. The lack of symmetry breaking in the non-polarized regimes allows $\mathbf{M}(\mathbf{k})$ and the stability analysis to be simplified greatly. We consider these solutions first.

A.2.1 Stability of stationary (non-polarized) states

First, we analyze the region in which $m_{ss} = |p_{ss}| = 0$. Here, $\mathbf{M}(\mathbf{k})$ is simplified by considering $\mathbf{p}_{\mathbf{k}} = p_{\mathbf{k}}^L \hat{\mathbf{k}} + p_{\mathbf{k}}^T \hat{\mathbf{k}}_{\perp}$ as shown in Eq. (A.15). This form, for later convenience, applies to both the fluid and solid.

$$\mathbf{M}^{iso}(\mathbf{k}) = \begin{bmatrix} -\alpha - 3\beta m_{ss}^2 - Dk^2 & -i\sigma(m_{ss})k & 0 \\ i\nu k & -\alpha_p(m_{ss}) - D_p k^2 & 0 \\ 0 & 0 & -\alpha_p(m_{ss}) - D_p k^2 \end{bmatrix}, \quad (\text{A.15})$$

where $\alpha_p(m_{ss}) \equiv \alpha_p^0 - am_{ss}$ and $\sigma(m_{ss}) \equiv \sigma - \nu_2 m_{ss}$. We see that fluctuations $p_{\mathbf{k}}^T$ in the transverse polarization, describing bend deformations, are decoupled and always stable,

and decay at the rate $z_{\perp} = -\alpha_p(m_{ss}) - D_p k^2$. The other two eigenvalues control coupled fluctuations in shape and longitudinal polarization $p_{\mathbf{k}}^L$, corresponding to splay deformations and are given by the solutions of a quadratic equation,

$$2z_{\pm}(k) = -[\alpha(m_{ss}) + \alpha_p(m_{ss})] - (D + D_p)k^2 \pm \sqrt{[\alpha(m_{ss}) - \alpha_p(m_{ss}) + (D - D_p)k^2]^2 + 4k^2\nu\sigma(m_{ss})}, \quad (\text{A.16})$$

where $\alpha(m_{ss}) = \alpha + 3\beta m_{ss}^2$. The stability is always controlled by the mode $z_+(k)$.

A.2.2 Stability of Stationary Solid

In the solid $m_{ss} = 0$, hence $\alpha_p(m_{ss}) = \alpha_p^0$ and $\sigma(m_{ss}) = \sigma$. Instabilities in the homogeneous stationary solid will arise ($z_+(k) > 0$) when

$$\sigma\nu > \left(\sqrt{\alpha_p^0 D} + \sqrt{\alpha D_p} \right)^2 \quad (\text{A.17})$$

in a band of wavenumbers $k_- < k < k_+$. The wavenumbers k_{\pm} are solutions of a quadratic equation

$$\alpha\alpha_p^0 + [\alpha D_p + \alpha_p^0 D - \sigma\nu] k^2 + DD_p k^4 = 0 \quad (\text{A.18})$$

and are given by

$$k_{\pm}^2 = - \left[\frac{\alpha}{2D} + \frac{\alpha_p^0}{2D_p} - \frac{\sigma\nu}{2DD_p} \right] \pm \sqrt{\left[\frac{\alpha}{2D} + \frac{\alpha_p^0}{2D_p} - \frac{\sigma\nu}{2DD_p} \right]^2 - \frac{\alpha\alpha_p^0}{DD_p}}. \quad (\text{A.19})$$

These solutions are real provided Eq. (A.17) is satisfied. The dispersion relation of the mode $z_+(k)$ in the stationary solid phase is shown in Fig. (A.2) for a few parameter values. Note that an instability can only occur provided $\sigma\nu > 0$. Near the onset of instability the

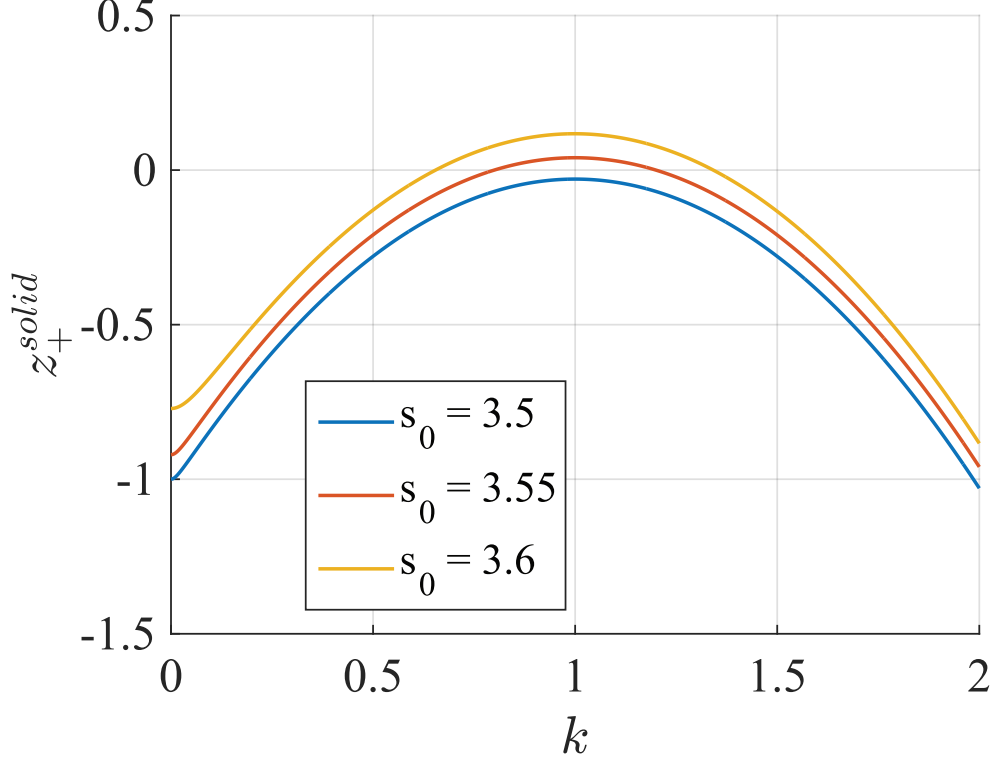


Figure A.2: Dispersion relation of the eigenvalue $z_+^{solid}(k)$ in the stationary solid phase as a function of k . Lines correspond to points in the $\nu = 1$ phase diagram from Fig.4.5. The blue curve then corresponds to a stable homogeneous state, while yellow and green represent unstable states.

wavelength of the fastest growing mode is given by

$$\ell^{solid} = \left(\frac{DD_p}{\alpha\alpha_p^0} \right)^{1/4}, \quad (\text{A.20})$$

which is the geometric average of the length scale $l_m(m_{ss}) = \sqrt{D/\alpha(m_{ss})}$ governing variation in m and the length scale $l_p(m_{ss}) = \sqrt{D_p/\alpha_p(m_{ss})}$ controlling spatial variation of the polarization \mathbf{p} . The lengths l_m and l_p represent the characteristic distances over which diffusion balances the decay rate. In the solid phase, we find emergent patterns as s_0 is increased. Further increase of s_0 increases the characteristic scales of such patterns. Because $\alpha(s_0)$ is roughly linear in s_0 in the range of interest, we may deduce the critical scaling as $l \sim (s_0 - s_0^*)^{0.25}$, where $s_0^* = 3.812$.

A.2.3 Stability of Stationary Fluid

In the fluid, we have $m_{ss}^2 = -\alpha/\beta$, $\alpha_p(m_{ss}) = \alpha_p^0 - am_{ss}$ and $\sigma(m_{ss}) = \sigma - \nu_2 m_{ss}$. When

$$\nu\sigma(m_{ss}) > \left(\sqrt{\alpha_p(m_{ss})D} + \sqrt{2|\alpha|D_p} \right)^2 \quad (\text{A.21})$$

the mode z_+ is unstable for a band of wavevectors $k_- < k < k_+$. The wavevectors k_{\pm} are again solutions of a quadratic equation

$$\alpha\alpha_p(m_{ss}) + [\alpha D_p + \alpha_p(m_{ss})D - \sigma(m_{ss})\nu]k^2 + DD_p k^4 = 0 \quad (\text{A.22})$$

and are given by

$$\begin{aligned} k_{\pm}^2 = & - \left[\frac{\alpha_p(m_{ss})}{2D_p} - \frac{\alpha}{D} - \frac{\nu\sigma(m_{ss})}{2DD_p} \right] \\ & \pm \sqrt{\left[\frac{\alpha_p(m_{ss})}{2D_p} - \frac{\alpha}{D} - \frac{\nu\sigma(m_{ss})}{2DD_p} \right]^2 + 2\frac{\alpha\alpha_p(m_{ss})}{DD_p}}. \end{aligned} \quad (\text{A.23})$$

From this equation we are able to isolate the stability condition as well as the characteristic wavevector of the fastest growing mode near the stability-instability boundary. This gives us a lengthscale

$$\ell^{fluid} = \sqrt{-DD_p/2\alpha(\alpha_p^0 - am_{ss})} \quad (\text{A.24})$$

expected to govern emerging patterns. Again this may be thought of as the geometric average of the length scales $\ell_m(m_{ss})$ and $\ell_p(m_{ss})$ controlling spatial variation in the decoupled fields.

A.2.4 Stability of Flocking Fluid

In this case there is special direction in the system, which is the direction of the broken-symmetry $\mathbf{p}_{ss} \neq 0$, and all modes are coupled. The stability matrix is given by

$$\mathbf{M}^{pol}(\mathbf{k}) = \begin{bmatrix} 2\alpha + i\nu_1 p_{ss} k_x & -i\sigma(m_{ss})k_x & -i\sigma(m_{ss})k_y \\ -Dk^2 & & \\ i\nu k_x + ap_{ss} & 2\alpha_p(m_{ss}) & i\lambda_3 p_{ss} k_y \\ & +i\lambda_T p_{ss} k_x - D_p k^2 & \\ i\nu k_y & -2i\lambda_2 p_{ss} k_y & i\lambda_1 p_{ss} k_x - D_p k^2 \end{bmatrix}, \quad (\text{A.25})$$

where we have chosen a coordinate system with the x axis along the direction of broken symmetry, so that $\mathbf{p}_{ss} = p_{ss} \hat{\mathbf{x}}$. We have defined $\lambda_T = \lambda_1 - 2\lambda_2 + \lambda_3$. To avoid solving a cubic equation for the decay rates, we only estimate stability along special directions.

Banding Instability

We first examine the behavior of the modes for \mathbf{k} along the direction of broken symmetry, $\mathbf{k} = k \hat{\mathbf{x}}$. Fluctuations in $p_{\mathbf{k}}^y$ then decouple and are always stable. The quadratic equation for the remaining two modes is easily solved, with the result

$$\begin{aligned} 2z_{\pm}^{(band)} = & 2(\alpha + \alpha_p(m_{ss})) + ip_{ss}(\nu_1 + \lambda_T)k - (D + D_p)k^2 \\ & \pm \left[\left[2(\alpha - \alpha_p(m_{ss})) + ip_{ss}(\nu_1 - \lambda_{TOT})k - (D - D_p)k^2 \right]^2 \right. \\ & \left. + 4\sigma(m_{ss})(\nu k^2 - ikap_{ss}) \right]^{1/2}. \end{aligned} \quad (\text{A.26})$$

Close to the mean-field transition between stationary and flocking liquid ($\alpha_p(m_{ss}) = 0$) a small wavevector expansion yields an instability for

$$\nu\sigma(m_{ss}) > 2|\alpha|D_p > 0. \quad (\text{A.27})$$

The instability boundaries shown in our phase diagram are obtained, however, through a more general analysis carried out with Mathematica. The wavelength of the fastest growing mode can also be calculated. In the limit $\alpha_p(m_{ss}) \rightarrow 0$ it is given by

$$\ell_{band} \sim \frac{\pi}{|\alpha|} \sqrt{\frac{2\sigma(m_{ss})\nu|\alpha|(D_p - D) - \sigma(m_{ss})^2\nu^2}{|\alpha|D_p - \frac{1}{2}\sigma(m_{ss})\nu}}. \quad (\text{A.28})$$

This instability is analogous to the banding instability of Toner-Tu models, as it describes the onset of bands of alternating ordered and disordered regions preferentially aligned in the direction transverse to that of broken symmetry.

Instability of Splay Fluctuations

We now analyze the stability deep in the ordered polar state. In this region, fluctuations in p_{ss} always decay on short time scales. For this reason we neglect $\partial_t p_x$ and eliminate p_x in favor of p_y and m , obtaining again a quadratic equation for the dispersion relation of the modes that can be solved analytically. For simplicity we only examine the modes for $\mathbf{k} = k_x \hat{x}$ and $\mathbf{k} = k_y \hat{y}$. These decay rates of the hydrodynamic mode are then given by

$$z_+^{(flock)}(k_x) = iA_x k_x - D_p k_x^2 + \mathcal{O}(k_x^3) \quad (\text{A.29})$$

and

$$z_+^{(flock)}(k_y) = iA_y k_y - D_y^{eff} k_y^2 + \mathcal{O}(k_y^3). \quad (\text{A.30})$$

The mode is always stable for $\mathbf{k} = k_x \hat{x}$. In contrast,

$$D_y^{eff} = D_p - \frac{\lambda_2 \lambda_3}{\beta_p} - \frac{\sigma(m_{ss})}{2|\alpha|} \left(\nu - \frac{a\lambda_2}{\beta_p} \right) \quad (\text{A.31})$$

changes sign, resulting in the coupled instability of shape anisotropy and splay fluctuations of the polarization for

$$\sigma(m_{ss})\nu > \frac{\sigma(m_{ss})\lambda_2 a}{\beta_p} + 2|\alpha| \left(D_p - \frac{\lambda_2 \lambda_3}{\beta_p} \right). \quad (\text{A.32})$$

Bibliography

- [1] M. Abercrombie. Contact inhibition in tissue culture. *In Vitro*, 6(2):128–142, sep 1970.
- [2] Thomas E Angelini, Edouard Hannezo, Xavier Trepant, Manuel Marquez, Jeffrey J Fredberg, and David A Weitz. Glass-like dynamics of collective cell migration. *Proceedings of the National Academy of Sciences of the United States of America*, 108(12):4714–9, mar 2011.
- [3] Gil Ariel and Amir Ayali. Locust Collective Motion and Its Modeling. *PLOS Computational Biology*, 11(12):e1004522, dec 2015.
- [4] J Baker and D Garrod. Epithelial cells retain junctions during mitosis. *Journal of cell science*, 104 (Pt 2):415–25, feb 1993.
- [5] M Ballerini, N Cabibbo, R Candelier, A Cavagna, E Cisbani, I Giardina, V Lecomte, A Orlandi, G Parisi, A Procaccini, M Viale, and V Zdravkovic. Interaction ruling animal collective behavior depends on topological rather than metric distance: evidence from a field study. *Proceedings of the National Academy of Sciences of the United States of America*, 105(4):1232–7, jan 2008.
- [6] S. Banerjee and M. C. Marchetti. Substrate rigidity deforms and polarizes active gels. *EPL (Europhysics Letters)*, 96(2):28003, oct 2011.

- [7] Shiladitya Banerjee and M. Cristina Marchetti. Contractile Stresses in Cohesive Cell Layers on Finite-Thickness Substrates. *Physical Review Letters*, 109(10):108101, sep 2012.
- [8] Shiladitya Banerjee, Kazage J.C. Utuje, and M. Cristina Marchetti. Propagating Stress Waves During Epithelial Expansion. *Physical Review Letters*, 114(22):228101, jun 2015.
- [9] Daniel L. Barton, Silke Henkes, Cornelis J. Weijer, and Rastko Sknepnek. Active Vertex Model for cell-resolution description of epithelial tissue mechanics. *PLOS Computational Biology*, 13(6):e1005569, jun 2017.
- [10] Aparna Baskaran and M. Cristina Marchetti. Hydrodynamics of self-propelled hard rods. *Physical Review E*, 77(1):011920, January 2008.
- [11] L. V. Belousov, N. N. Louchinskaia, and A. A. Stein. Tension-dependent collective cell movements in the early gastrula ectoderm of *Xenopus laevis* embryos. *Development Genes and Evolution*, 210(2):92–104, jan 2000.
- [12] Claire Bertet, Lawrence Sulak, and Thomas Lecuit. Myosin-dependent junction remodelling controls planar cell intercalation and axis elongation. *Nature*, 429(6992):667–671, jun 2004.
- [13] Ludovic Berthier. Nonequilibrium Glassy Dynamics of Self-Propelled Hard Disks. *Physical Review Letters*, 112(22):220602, jun 2014.
- [14] Ludovic Berthier and Jorge Kurchan. Non-equilibrium glass transitions in driven and active matter. *Nature Physics*, 9(5):310–314, may 2013.
- [15] Eric Bertin, Michel Droz, and Guillaume Grégoire. Hydrodynamic equations for self-propelled particles: microscopic derivation and stability analysis. *Journal of Physics A: Mathematical and Theoretical*, 42(44):445001, November 2009.

- [16] Dapeng Bi, J. H. Lopez, J. M. Schwarz, and M. Lisa Manning. A density-independent rigidity transition in biological tissues. *Nature Physics*, pages 1074–1079, sep 2015.
- [17] Dapeng Bi, Jorge H Lopez, J M Schwarz, and M Lisa Manning. Energy barriers and cell migration in densely packed tissues. *Soft matter*, 10(12):1885–90, March 2014.
- [18] Dapeng Bi, Xingbo Yang, M. Cristina Marchetti, and M. Lisa Manning. Motility-Driven Glass and Jamming Transitions in Biological Tissues. *Physical Review X*, 6(2):021011, apr 2016.
- [19] Julian Bialké, Hartmut Löwen, and Thomas Speck. Microscopic theory for the phase separation of self-propelled repulsive disks. *EPL (Europhysics Letters)*, 103(3):30008, aug 2013.
- [20] C. Blanch-Mercader and J. Casademunt. Hydrodynamic instabilities, waves and turbulence in spreading epithelia. *Soft Matter*, 13(38):6913–6928, oct 2017.
- [21] C. Blanch-Mercader, R. Vincent, E. Bazellères, X. Serra-Picamal, X. Trepât, and J. Casademunt. Effective viscosity and dynamics of spreading epithelia: a solvable model. *Soft Matter*, 13(6):1235–1243, feb 2017.
- [22] Antoine Bricard, Jean-Baptiste Caussin, Nicolas Desreumaux, Olivier Dauchot, and Denis Bartolo. Emergence of macroscopic directed motion in populations of motile colloids. *Nature*, 503(7474):95–98, nov 2013.
- [23] J Buhl, D J T Sumpter, I D Couzin, J J Hale, E Despland, E R Miller, and S J Simpson. From disorder to order in marching locusts. *Science (New York, N.Y.)*, 312(5778):1402–6, jun 2006.
- [24] M E Cates, D Marenduzzo, I Pagonabarraga, and J Tailleur. Arrested phase separation in reproducing bacteria creates a generic route to pattern formation. *Proceedings of*

- the National Academy of Sciences of the United States of America*, 107(26):11715–20, jun 2010.
- [25] Oleksandr Chepizhko, Maria Chiara Lionetti, Chiara Malinverno, Costanza Giampietro, Giorgio Scita, Stefano Zapperi, and Caterina A. M. La Porta. From jamming to collective cell migration through a boundary induced transition. *Soft Matter*, 14(19):3774–3782, may 2018.
- [26] M. Chiang and D. Marenduzzo. Glass transitions in the cellular Potts model. *EPL (Europhysics Letters)*, 116(2):28009, oct 2016.
- [27] Ian Conlon and Martin Raff. Differences in the way a mammalian cell and yeast cells coordinate cell growth and cell-cycle progression. *Journal of Biology*, 2(1):7, apr 2003.
- [28] Robert David, Olivia Luu, Erich W Damm, Jason W H Wen, Martina Nagel, and Rudolf Winklbauer. Tissue cohesion and the mechanics of cell rearrangement. *Development (Cambridge, England)*, 141(19):3672–82, October 2014.
- [29] Stijn P. De Langhe, Frédéric G. Sala, Pierre-Marie Del Moral, Timothy J. Fairbanks, Kenneth M. Yamada, David Warburton, Robert C. Burns, and Saverio Belusci. Dickkopf-1 (DKK1) reveals that fibronectin is a major target of Wnt signaling in branching morphogenesis of the mouse embryonic lung. *Developmental Biology*, 277(2):316–331, jan 2005.
- [30] Dennis E. Discher, Paul Janmey, and Yu-li Wang. Tissue Cells Feel and Respond to the Stiffness of Their Substrate. *Science*, 310(5751), 2005.
- [31] Helmut Dolznig, Florian Grebien, Thomas Sauer, Hartmut Beug, and Ernst W. Müllner. Evidence for a size-sensing mechanism in animal cells. *Nature Cell Biology*, 6(9):899–905, sep 2004.

- [32] Michelle Driscoll, Blaise Delmotte, Mena Youssef, Stefano Sacanna, Aleksandar Donev, and Paul Chaikin. Unstable fronts and motile structures formed by microrollers. *Nature Physics*, 13(4):375–379, apr 2017.
- [33] G Duclos, S Garcia, H G Yevick, and P Silberzan. Perfect nematic order in confined monolayers of spindle-shaped cells. *Soft matter*, 10(14):2346–53, apr 2014.
- [34] Ellen C. Lee, Michael J. Solomon, and Susan J. Muller. Molecular Orientation and Deformation of Polymer Solutions under Shear: A Flow Light Scattering Study. 1997.
- [35] Adam J. Engler, Shamik Sen, H. Lee Sweeney, and Dennis E. Discher. Matrix Elasticity Directs Stem Cell Lineage Specification. *Cell*, 126(4):677–689, aug 2006.
- [36] Raphaël Etournay, Marko Popović, Matthias Merkel, Amitabha Nandi, Corinna Blasse, Benoît Aigouy, Holger Brandl, Gene Myers, Guillaume Salbreux, Frank Jülicher, and Suzanne Eaton. Interplay of cell dynamics and epithelial tension during morphogenesis of the *Drosophila* pupal wing. *eLife*, 4:e07090, jun 2015.
- [37] Michael L. Falk and J.S. Langer. Deformation and Failure of Amorphous, Solidlike Materials. *Annual Review of Condensed Matter Physics*, 2(1):353–373, mar 2011.
- [38] Reza Farhadifar, Jens-Christian Röper, Benoit Aigouy, Suzanne Eaton, and Frank Jülicher. The influence of cell mechanics, cell-cell interactions, and proliferation on epithelial packing. *Current biology : CB*, 17(24):2095–104, December 2007.
- [39] Yaouen Fily and M. Cristina Marchetti. Athermal Phase Separation of Self-Propelled Particles with No Alignment. *Physical Review Letters*, 108(23):235702, jun 2012.
- [40] Peter J Foster, Sebastian Fürthauer, Michael J Shelley, and Daniel J Needleman. Active contraction of microtubule networks. *eLife*, 4, dec 2015.
- [41] Peter Friedl and Darren Gilmour. Collective cell migration in morphogenesis, regeneration and cancer. *Nature Reviews Molecular Cell Biology*, 10(7):445–457, jul 2009.

- [42] Simon Garcia, Edouard Hannezo, Jens Elgeti, Jean-François Joanny, Pascal Silberzan, and Nir S Gov. Physics of active jamming during collective cellular motion in a monolayer. *Proceedings of the National Academy of Sciences of the United States of America*, pages 1510973112–, dec 2015.
- [43] Fabio Giavazzi, Chiara Malinverno, Salvatore Corallino, Francesco Ginelli, Giorgio Scita, and Roberto Cerbino. Giant fluctuations and structural effects in a flocking epithelium. *Journal of Physics D: Applied Physics*, 50(38):384003, sep 2017.
- [44] Fabio Giavazzi, Matteo Paoluzzi, Marta Macchi, Dapeng Bi, Giorgio Scita, M. Lisa Manning, Roberto Cerbino, and M. Cristina Marchetti. Flocking Transition in Confluent Tissues. jun 2017.
- [45] Kripa Gowrishankar and Madan Rao. Nonequilibrium phase transitions, fluctuations and correlations in an active contractile polar fluid. *Soft Matter*, 12(7):2040–2046, feb 2016.
- [46] François Graner and James Glazier. Simulation of biological cell sorting using a two-dimensional extended Potts model. *Physical Review Letters*, 69(13):2013–2016, sep 1992.
- [47] Guillaume Grégoire and Hugues Chaté. Onset of Collective and Cohesive Motion. *Physical Review Letters*, 92(2):025702, January 2004.
- [48] Giorgia Guglielmi, Henning Johannes Falk, and Stefano De Renzi. Optogenetic Control of Protein Function: From Intracellular Processes to Tissue Morphogenesis. *Trends in cell biology*, 26(11):864–874, 2016.
- [49] Andrew R Harris, Loic Peter, Julien Bellis, Buzz Baum, Alexandre J Kabla, and Guillaume T Charras. Characterizing the mechanics of cultured cell monolayers. *Proceedings of the National Academy of Sciences of the United States of America*, 109(41):16449–54, oct 2012.

- [50] B. Hein, K. I. Willig, and S. W. Hell. Stimulated emission depletion (STED) nanoscopy of a fluorescent protein-labeled organelle inside a living cell. *Proceedings of the National Academy of Sciences*, 105(38):14271–14276, sep 2008.
- [51] David L Henann and Ken Kamrin. A predictive, size-dependent continuum model for dense granular flows. *Proceedings of the National Academy of Sciences of the United States of America*, 110(17):6730–5, apr 2013.
- [52] Silke Henkes, Yaouen Fily, and M. Cristina Marchetti. Active jamming: Self-propelled soft particles at high density. *Physical Review E*, 84(4):040301, October 2011.
- [53] Stephanie Höhn, Aurelia R. Honerkamp-Smith, Pierre A. Haas, Philipp Khuc Trong, and Raymond E. Goldstein. Dynamics of a *Volvox* Embryo Turning Itself Inside Out. *Physical Review Letters*, 114(17):178101, apr 2015.
- [54] Jonathan R. Howse, Richard A. L. Jones, Anthony J. Ryan, Tim Gough, Reza Vafabakhsh, and Ramin Golestanian. Self-Motile Colloidal Particles: From Directed Propulsion to Random Walk. *Physical Review Letters*, 99(4):048102, jul 2007.
- [55] Lars Hufnagel, Aurelio A Teleman, Hervé Rouault, Stephen M Cohen, and Boris I Shraiman. On the mechanism of wing size determination in fly development. *Proceedings of the National Academy of Sciences of the United States of America*, 104(10):3835–40, March 2007.
- [56] Jan Huisken, Jim Swoger, Filippo Del Bene, Joachim Wittbrodt, and Ernst H K Stelzer. Optical sectioning deep inside live embryos by selective plane illumination microscopy. *Science (New York, N.Y.)*, 305(5686):1007–9, aug 2004.
- [57] Shuji Ishihara, Philippe Marcq, and Kaoru Sugimura. From cells to tissue: A continuum model of epithelial mechanics. *Physical Review E*, 96(2):022418, aug 2017.

- [58] Han-Sung Jung, Philippa H Francis-West, Randall B Widelitz, Ting-Xin Jiang, Sheree Ting-Berreth, Cheryl Tickle, Lewis Wolpert, and Cheng-Ming Chuong. Local Inhibitory Action of BMPs and Their Relationships with Activators in Feather Formation: Implications for Periodic Patterning. *Developmental Biology*, 196(1):11–23, apr 1998.
- [59] Alexandre J Kabla. Collective cell migration: leadership, invasion and segregation. *Journal of the Royal Society, Interface / the Royal Society*, 9(77):3268–78, December 2012.
- [60] Arben Kalziqi, David Yanni, Jacob Thomas, Siu Lung Ng, Skanda Vivek, Brian K. Hammer, and Peter J. Yunker. Immotile Active Matter: Activity from Death and Reproduction. *Physical Review Letters*, 120(1):018101, jan 2018.
- [61] K. E. Kasza, D. L. Farrell, and J. A. Zallen. Spatiotemporal control of epithelial remodeling by regulated myosin phosphorylation. *Proceedings of the National Academy of Sciences*, 2014.
- [62] Kyogo Kawaguchi, Ryoichiro Kageyama, and Masaki Sano. Topological defects control collective dynamics in neural progenitor cell cultures. *Nature*, 2017.
- [63] R. Keller, L. Davidson, A. Edlund, T. Elul, M. Ezin, D. Shook, and P. Skoglund. Mechanisms of convergence and extension by cell intercalation. *Philosophical Transactions of the Royal Society B: Biological Sciences*, 355(1399):897–922, jul 2000.
- [64] Ray Keller, Lance A. Davidson, and David R. Shook. How we are shaped: The biomechanics of gastrulation. *Differentiation*, 71(3):171–205, apr 2003.
- [65] D P Kiehart, C G Galbraith, K A Edwards, W L Rickoll, and R A Montague. Multiple forces contribute to cell sheet morphogenesis for dorsal closure in *Drosophila*. *The Journal of cell biology*, 149(2):471–90, apr 2000.

- [66] Jae Hun Kim, Xavier Serra-Picamal, Dhananjay T Tambe, Enhua H Zhou, Chan Young Park, Monirosadat Sadati, Jin-Ah Park, Ramaswamy Krishnan, Bomi Gweon, Emil Millet, James P Butler, Xavier Trepast, and Jeffrey J Fredberg. Propulsion and navigation within the advancing monolayer sheet. *Nature materials*, 12(9):856–63, 2013.
- [67] Simone Köhler and Andreas R. Bausch. Contraction Mechanisms in Composite Active Actin Networks. *PLoS ONE*, 7(7):e39869, jul 2012.
- [68] Shigeru Kondo and Takashi Miura. Reaction-diffusion model as a framework for understanding biological pattern formation. *Science (New York, N.Y.)*, 329(5999):1616–20, sep 2010.
- [69] Michael H. Köpf and Len M. Pismen. A continuum model of epithelial spreading. *Soft Matter*, 9(14):3727, 2013.
- [70] Matej Krajnc, Sabyasachi Dasgupta, Primož Zihlerl, and Jacques Prost. Fluidization of sheet-like tissues by active cell rearrangements. may 2018.
- [71] Uros Krzic, Stefan Gunther, Timothy E Saunders, Sebastian J Streichan, and Lars Hufnagel. Multiview light-sheet microscope for rapid in toto imaging. *Nature Methods*, 9(7):730–733, jul 2012.
- [72] J R Kuszak. The ultrastructure of epithelial and fiber cells in the crystalline lens. *International review of cytology*, 163:305–50, 1995.
- [73] Martin Lenz. Geometrical Origins of Contractility in Disordered Actomyosin Networks. *Physical Review X*, 4(4):041002, oct 2014.
- [74] Tanniemola B Liverpool and M Cristina Marchetti. Hydrodynamics and rheology of active polar filaments. In *Cell motility*, pages 177–206. Springer, 2008.
- [75] Chiara Malinverno, Salvatore Corallino, Fabio Giavazzi, Martin Bergert, Qingsen Li, Marco Leoni, Andrea Disanza, Emanuela Frittoli, Amanda Oldani, Emanuele Martini,

- Tobias Lendenmann, Gianluca Deflorian, Galina V. Beznoussenko, Dimos Poulikakos, Kok Haur Ong, Marina Uroz, Xavier Trepas, Dario Parazzoli, Paolo Maiuri, Weimiao Yu, Aldo Ferrari, Roberto Cerbino, and Giorgio Scita. Endocytic reawakening of motility in jammed epithelia. *Nature Materials*, 16(5):587–596, jan 2017.
- [76] Abdul N. Malmi-Kakkada, Xin Li, Himadri S. Samanta, Sumit Sinha, and D. Thirumalai. Cell Growth Rate Dictates the Onset of Glass to Fluidlike Transition and Long Time Superdiffusion in an Evolving Cell Colony. *Physical Review X*, 8(2):021025, apr 2018.
- [77] Adam C. Martin. Pulsation and stabilization: Contractile forces that underlie morphogenesis. *Developmental Biology*, 341(1):114–125, may 2010.
- [78] Adam C. Martin, Matthias Kaschube, and Eric F. Wieschaus. Pulsed contractions of an actinmyosin network drive apical constriction. *Nature*, 457(7228):495–499, jan 2009.
- [79] Paul Martin, Susan M Parkhurst, and M Peifer. Parallels between tissue repair and embryo morphogenesis. *Development (Cambridge, England)*, 131(13):3021–34, jul 2004.
- [80] Eric Martz and Malcolm S. Steinberg. The role of cell-cell contact in ?contact? inhibition of cell division: A review and new evidence. *Journal of Cellular Physiology*, 79(2):189–210, apr 1972.
- [81] D. A. Matoz-Fernandez, Kirsten Martens, Rastko Sknepnek, J. L. Barrat, and Silke Henkes. Cell division and death inhibit glassy behaviour of confluent tissues. *Soft Matter*, 13(17):3205–3212, may 2017.
- [82] D.A. Matoz-Fernandez, Elisabeth Agoritsas, Jean-Louis Barrat, Eric Bertin, and Kirsten Martens. Nonlinear Rheology in a Model Biological Tissue. *Physical Review Letters*, 118(15):158105, apr 2017.

- [83] Rowena McBeath, Dana M Pirone, Celeste M Nelson, Kiran Bhadriraju, and Christopher S Chen. Cell shape, cytoskeletal tension, and RhoA regulate stem cell lineage commitment. *Developmental cell*, 6(4):483–95, apr 2004.
- [84] Matthias Merkel, Raphaël Etournay, Marko Popović, Guillaume Salbreux, Suzanne Eaton, and Frank Jülicher. Triangles bridge the scales: Quantifying cellular contributions to tissue deformation. *Physical Review E*, 95(3):032401, mar 2017.
- [85] Matthias Merkel and M Lisa Manning. A geometrically controlled rigidity transition in a model for confluent 3D tissues. *New Journal of Physics*, 20(2):022002, feb 2018.
- [86] N. D. Mermin and H. Wagner. Absence of Ferromagnetism or Antiferromagnetism in One- or Two-Dimensional Isotropic Heisenberg Models. *Physical Review Letters*, 17(22):1133–1136, nov 1966.
- [87] Shradha Mishra, Aparna Baskaran, and M. Cristina Marchetti. Fluctuations and pattern formation in self-propelled particles. *Physical Review E*, 81(6):061916, jun 2010.
- [88] Hitoshi Morita, Silvia Grigolon, Martin Bock, S.F. Gabriel Krens, Guillaume Salbreux, and Carl-Philipp Heisenberg. The Physical Basis of Coordinated Tissue Spreading in Zebrafish Gastrulation. *Developmental Cell*, 40(4):354–366.e4, feb 2017.
- [89] Michael Moshe, Mark J. Bowick, and M. Cristina Marchetti. Geometric frustration and rigidity transitions in 2D tissue. aug 2017.
- [90] Satoshi Nakata and Kyoko Matsuo. Characteristic self-motion of a camphor boat sensitive to ester vapor. *Langmuir*, 21(3):982–984, 2005. PMID: 15667178.
- [91] Lisa M Nash, Dustin Kleckner, Alismari Read, Vincenzo Vitelli, Ari M Turner, and William T M Irvine. Topological mechanics of gyroscopic metamaterials. *Proceedings of*

- the National Academy of Sciences of the United States of America*, 112(47):14495–500, nov 2015.
- [92] Daniel J Needleman, Yangqing Xu, and Timothy J Mitchison. Pin-hole array correlation imaging: highly parallel fluorescence correlation spectroscopy. *Biophysical journal*, 96(12):5050–9, jun 2009.
- [93] Kenechukwu David Nnetu, Melanie Knorr, Josef Käs, and Mareike Zink. The impact of jamming on boundaries of collectively moving weak-interacting cells. *New Journal of Physics*, 14(11):115012, nov 2012.
- [94] Jin-Ah Park, Jae Hun Kim, Dapeng Bi, Jennifer A. Mitchel, Nader Taheri Qazvini, Kelan Tantisira, Chan Young Park, Maureen McGill, Sae-Hoon Kim, Bomi Gweon, Jacob Notbohm, Robert Steward Jr, Stephanie Burger, Scott H. Randell, Alvin T. Kho, Dhananjay T. Tambe, Corey Hardin, Stephanie A. Shore, Elliot Israel, David A. Weitz, Daniel J. Tschumperlin, Elizabeth P. Henske, Scott T. Weiss, M. Lisa Manning, James P. Butler, Jeffrey M. Drazen, and Jeffrey J. Fredberg. Unjamming and cell shape in the asthmatic airway epithelium. *Nature Materials*, 14(10):1040–1048, oct 2015.
- [95] Matthew J. Paszek, Nastaran Zahir, Kandice R. Johnson, Johnathon N. Lakins, Gabriela I. Rozenberg, Amit Gefen, Cynthia A. Reinhart-King, Susan S. Margulies, Micah Dembo, David Boettiger, Daniel A. Hammer, and Valerie M. Weaver. Tensional homeostasis and the malignant phenotype. *Cancer Cell*, 8(3):241–254, sep 2005.
- [96] Adam Patch, David Yllanes, and M. Cristina Marchetti. Kinetics of motility-induced phase separation and swim pressure. *Physical Review E*, 95(1):012601, jan 2017.
- [97] Steve Pawlizak, Anatol W. Fritsch, Steffen Grosser, Dave Ahrens, Tobias Thalheim, Stefanie Riedel, Tobias R. Kießling, Linda Oswald, Mareike Zink, M. Lisa Manning, and Josef A. Käs. Testing the differential adhesion hypothesis across the epithelial-mesenchymal transition. *New Journal of Physics*, 17(8), 2015.

- [98] Walter F. Paxton, Ayusman Sen, and Thomas E. Mallouk. Motility of Catalytic Nanoparticles through Self-Generated Forces. *Chemistry - A European Journal*, 11(22):6462–6470, nov 2005.
- [99] Andrea Maria Pereira, Cicerone Tudor, Johannes S. Kanger, Vinod Subramaniam, and Enrique Martin-Blanco. Integrin-Dependent Activation of the JNK Signaling Pathway by Mechanical Stress. *PLoS ONE*, 6(12):e26182, dec 2011.
- [100] L Petitjean, M Reffay, E Grasland-Mongrain, M Poujade, B Ladoux, A Buguin, and P Silberzan. Velocity fields in a collectively migrating epithelium. *Biophysical journal*, 98(9):1790–800, May 2010.
- [101] M Poujade, E Grasland-Mongrain, A Hertzog, J Jouanneau, P Chavrier, B Ladoux, A Buguin, and P Silberzan. Collective migration of an epithelial monolayer in response to a model wound. *Proceedings of the National Academy of Sciences of the United States of America*, 104(41):15988–93, October 2007.
- [102] Alberto Puliafito, Lars Hufnagel, Pierre Neveu, Sebastian Streichan, Alex Sigal, D Kuchnir Fygenson, and Boris I Shraiman. Collective and single cell behavior in epithelial contact inhibition. *Proceedings of the National Academy of Sciences of the United States of America*, 109(3):739–44, jan 2012.
- [103] F. Puosi, J. Rottler, and J-L. Barrat. Time-dependent elastic response to a local shear transformation in amorphous solids. *Physical Review E*, 89(4):042302, apr 2014.
- [104] T. Putelat, P. Recho, and L. Truskinovsky. Mechanical stress as a regulator of cell motility. *Physical Review E*, 97(1):012410, jan 2018.
- [105] Jonas Ranft, Markus Basan, Jens Elgeti, Jean-François Joanny, Jacques Prost, and Frank Jülicher. Fluidization of tissues by cell division and apoptosis. *Proceedings of the National Academy of Sciences of the United States of America*, 107(49):20863–8, dec 2010.

- [106] Matteo Rauzi, Pascale Verant, Thomas Lecuit, and Pierre-François Lenne. Nature and anisotropy of cortical forces orienting *Drosophila* tissue morphogenesis. *Nature Cell Biology*, 10(12):1401–1410, dec 2008.
- [107] A G Renehan, C Booth, and C S Potten. What is apoptosis, and why is it important? *BMJ (Clinical research ed.)*, 322(7301):1536–8, jun 2001.
- [108] Craig W. Reynolds, Craig W., Reynolds, and Craig W. Flocks, herds and schools: A distributed behavioral model. In *Proceedings of the 14th annual conference on Computer graphics and interactive techniques - SIGGRAPH '87*, volume 21, pages 25–34, New York, New York, USA, 1987. ACM Press.
- [109] Thomas Risler, Aurélien Peilloux, and Jacques Prost. Homeostatic Fluctuations of a Tissue Surface. *Physical Review Letters*, 115(25), dec 2015.
- [110] Pilar Rodríguez-Franco, Agustí Brugués, Ariadna Marín-Llauradó, Vito Conte, Guiomar Solanas, Eduard Batlle, Jeffrey J. Fredberg, Pere Roca-Cusachs, Raimon Sunyer, and Xavier Trepas. Long-lived force patterns and deformation waves at repulsive epithelial boundaries. *Nature Materials*, 16(10):1029–1037, sep 2017.
- [111] J Rosenblatt, M C Raff, and L P Cramer. An epithelial cell destined for apoptosis signals its neighbors to extrude it by an actin- and myosin-dependent mechanism. *Current biology : CB*, 11(23):1847–57, nov 2001.
- [112] Monirosadat Sadati, Nader Taheri Qazvini, Ramaswamy Krishnan, Chan Young Park, and Jeffrey J Fredberg. Collective migration and cell jamming. *Differentiation; research in biological diversity*, 86(3):121–5, October 2013.
- [113] Tim Sanchez, Daniel T. N. Chen, Stephen J. DeCamp, Michael Heymann, and Zvonimir Dogic. Spontaneous motion in hierarchically assembled active matter. *Nature*, 491(7424):431–434, nov 2012.

- [114] Thuan Beng Saw, Amin Doostmohammadi, Vincent Nier, Leyla Kocgozlu, Sumesh Thampi, Yusuke Toyama, Philippe Marcq, Chwee Teck Lim, Julia M. Yeomans, and Benoit Ladoux. Topological defects in epithelia govern cell death and extrusion. *Nature*, 544(7649):212–216, apr 2017.
- [115] E.-M. Schotz, M. Lanio, J. A. Talbot, and M. L. Manning. Glassy dynamics in three-dimensional embryonic tissues. *Journal of The Royal Society Interface*, 10(89):20130726–20130726, 2013.
- [116] EvaMaria Schötz, Rebecca D. Burdine, Frank Jülicher, Malcolm S. Steinberg, Carl-Philipp Heisenberg, and Ramsey A. Foty. Quantitative differences in tissue surface tension influence zebrafish germ layer positioning. *HFSP Journal*, 2(1):42–56, feb 2008.
- [117] Charles M. Schroeder, Rodrigo E. Teixeira, Eric S. G. Shaqfeh, and Steven Chu. Characteristic Periodic Motion of Polymers in Shear Flow. *Physical Review Letters*, 95(1):018301, jul 2005.
- [118] Rajesh Babu Sekar and Ammasi Periasamy. Fluorescence resonance energy transfer (FRET) microscopy imaging of live cell protein localizations. *The Journal of cell biology*, 160(5):629–33, mar 2003.
- [119] Friedhelm Serwane, Alessandro Mongera, Payam Rowghanian, David A Kealhofer, Adam A Lucio, Zachary M Hockenbery, and Otger Campàs. In vivo quantification of spatially varying mechanical properties in developing tissues. *Nature Methods*, 14(2):181–186, feb 2017.
- [120] Danying Shao, Herbert Levine, and Wouter-Jan Rappel. Coupling actin flow, adhesion, and morphology in a computational cell motility model. *Proceedings of the National Academy of Sciences of the United States of America*, 109(18):6851–6, may 2012.

- [121] Danying Shao, Wouter-Jan Rappel, and Herbert Levine. Computational Model for Cell Morphodynamics. *Physical Review Letters*, 105(10):108104, sep 2010.
- [122] Stefanie Sick, Stefan Reinker, Jens Timmer, and Thomas Schlake. WNT and DKK determine hair follicle spacing through a reaction-diffusion mechanism. *Science (New York, N.Y.)*, 314(5804):1447–50, dec 2006.
- [123] Peter Sollich. Soft Glassy Rheology. In *Molecular Gels*, pages 161–192. Springer-Verlag, Berlin/Heidelberg, 2006.
- [124] A. P. Solon, Y. Fily, A. Baskaran, M. E. Cates, Y. Kafri, M. Kardar, and J. Tailleur. Pressure is not a state function for generic active fluids. *Nature Physics*, 11(8):673–678, aug 2015.
- [125] Hojun Song, Bert Foquet, Ricardo Mariño-Pérez, and Derek A. Woller. Phylogeny of locusts and grasshoppers reveals complex evolution of density-dependent phenotypic plasticity. *Scientific Reports*, 7(1):6606, dec 2017.
- [126] D. B. Staple, R. Farhadifar, J. C. Röper, B. Aigouy, S. Eaton, and F. Jülicher. Mechanics and remodelling of cell packings in epithelia. *The European Physical Journal E*, 33(2):117–127, oct 2010.
- [127] H. Stark and T. C. Lubensky. Poisson-bracket approach to the dynamics of nematic liquid crystals. *Physical Review E*, 67(6):061709, jun 2003.
- [128] S. J. Streichan, C. R. Hoerner, T. Schneidt, D. Holzer, and L. Hufnagel. Spatial constraints control cell proliferation in tissues. *Proceedings of the National Academy of Sciences*, 111(15):5586–5591, 2014.
- [129] Sebastian J Streichan, Matthew F Lefebvre, Nicholas Noll, Eric F Wieschaus, and Boris I Shraiman. Global morphogenetic flow is accurately predicted by the spatial distribution of myosin motors. *eLife*, 7:e27454, feb 2018.

- [130] Robert W Style, Rostislav Boltyanskiy, Guy K German, Callen Hyland, Christopher W MacMinn, Aaron F Mertz, Larry A Wilen, Ye Xu, and Eric R Dufresne. Traction force microscopy in physics and biology. *Soft matter*, 10(23):4047–55, June 2014.
- [131] R. Sunyer, V. Conte, J. Escribano, A. Elosegui-Artola, A. Labernadie, L. Valon, D. Navajas, J. M. Garcia-Aznar, J. J. Munoz, P. Roca-Cusachs, and X. Trepat. Collective cell durotaxis emerges from long-range intercellular force transmission. *Science*, 353(6304):1157–1161, sep 2016.
- [132] Daniel M. Sussman. cellGPU: Massively parallel simulations of dynamic vertex models. *Computer Physics Communications*, 219:400–406, oct 2017.
- [133] Daniel M. Sussman and Matthias Merkel. No unjamming transition in a marginal vertex model of biological tissue. aug 2017.
- [134] Daniel M. Sussman, M. Paoluzzi, M. Cristina Marchetti, and M. Lisa Manning. Anomalous glassy dynamics in simple models of dense biological tissue. *EPL (Europhysics Letters)*, 121(3):36001, feb 2018.
- [135] K Svoboda and S M Block. Biological Applications of Optical Forces. *Annual Review of Biophysics and Biomolecular Structure*, 23(1):247–285, jun 1994.
- [136] Dhananjay T. Tambe, C. Corey Hardin, Thomas E. Angelini, Kavitha Rajendran, Chan Young Park, Xavier Serra-Picamal, Enhua H. Zhou, Muhammad H. Zaman, James P. Butler, David A. Weitz, Jeffrey J. Fredberg, and Xavier Trepat. Collective cell guidance by cooperative intercellular forces. *Nature Materials*, 10(6):469–475, jun 2011.
- [137] A G Thompson, J Tailleur, M E Cates, and R A Blythe. Lattice models of nonequilibrium bacterial dynamics. *Journal of Statistical Mechanics: Theory and Experiment*, 2011(02):P02029, feb 2011.

- [138] C B Thompson. Apoptosis in the pathogenesis and treatment of disease. *Science (New York, N. Y.)*, 267(5203):1456–62, mar 1995.
- [139] D’Arcy Wentworth Thompson. *On Growth and Form*. Cambridge University Press, first edition, 1917.
- [140] Todd Thoresen, Martin Lenz, and Margaret L. Gardel. Reconstitution of Contractile Actomyosin Bundles. *Biophysical Journal*, 100(11):2698–2705, jun 2011.
- [141] A. Y. Ting, K. H. Kain, R. L. Klemke, and R. Y. Tsien. Genetically encoded fluorescent reporters of protein tyrosine kinase activities in living cells. *Proceedings of the National Academy of Sciences*, 98(26):15003–15008, dec 2001.
- [142] Doug Tischer and Orion D. Weiner. Illuminating cell signalling with optogenetic tools. *Nature Reviews Molecular Cell Biology*, 15(8):551–558, aug 2014.
- [143] Sham Tlili, Estelle Gauquelin, Brigitte Li, Olivier Cardoso, Benoît Ladoux, H el ene Delano e-Ayari, and Fran ois Graner. Collective cell migration without proliferation: density determines cell velocity and wave velocity. *Royal Society Open Science*, 5(5):172421, may 2018.
- [144] John Toner and Yuhai Tu. Flocks, herds, and schools: A quantitative theory of flocking. *Physical Review E*, 58(4):4828–4858, October 1998.
- [145] Xavier Trepat, Michael R. Wasserman, Thomas E. Angelini, Emil Millet, David A. Weitz, James P. Butler, and Jeffrey J. Fredberg. Physical forces during collective cell migration. *Nature Physics*, 5(6):426–430, may 2009.
- [146] A. M. Turing. The Chemical Basis of Morphogenesis. *Philosophical Transactions of the Royal Society B: Biological Sciences*, 237(641):37–72, aug 1952.

- [147] Tamás Vicsek, András Czirók, Eshel Ben-Jacob, Inon Cohen, and Ofer Shochet. Novel Type of Phase Transition in a System of Self-Driven Particles. *Physical Review Letters*, 75(6):1226–1229, August 1995.
- [148] A. H. Voie, D. H. Burns, and F. A. Spelman. Orthogonal-plane fluorescence optical sectioning: Three-dimensional imaging of macroscopic biological specimens. *Journal of Microscopy*, 170(3):229–236, jun 1993.
- [149] N. Wang, K. Naruse, D. Stamenovic, J. J. Fredberg, S. M. Mijailovich, I. M. Tolic-Norrelykke, T. Polte, R. Mannix, and D. E. Ingber. Mechanical behavior in living cells consistent with the tensegrity model. *Proceedings of the National Academy of Sciences*, 98(14):7765–7770, jul 2001.
- [150] R C Weisenberg and C Cianci. ATP-induced gelation–contraction of microtubules assembled in vitro. *The Journal of cell biology*, 99(4 Pt 1):1527–33, oct 1984.
- [151] V. Westphal, S. O. Rizzoli, M. A. Lauterbach, D. Kamin, R. Jahn, and S. W. Hell. Video-Rate Far-Field Optical Nanoscopy Dissects Synaptic Vesicle Movement. *Science*, 320(5873):246–249, apr 2008.
- [152] Shunsuke Yabunaka, Philippe Marcq, V. Nier, L. Kocgozlu, S. Thampi, Y. Toyama, P. Marcq, C. T. Lim, J. M. Yeomans, and B. Ladoux. Emergence of epithelial cell density waves. *Soft Matter*, 544:212–216, 2017.
- [153] Daizou Yamada, Tsuyoshi Hondou, and Masaki Sano. Coherent dynamics of an asymmetric particle in a vertically vibrating bed. *Physical Review E*, 67(4):040301, apr 2003.
- [154] M. Yamaguchi, E. Yoshimoto, and S. Kondo. Pattern regulation in the stripe of zebrafish suggests an underlying dynamic and autonomous mechanism. *Proceedings of the National Academy of Sciences*, 104(12):4790–4793, mar 2007.

- [155] Xingbo Yang, Dapeng Bi, Michael Czajkowski, Matthias Merkel, M Lisa Manning, and M Cristina Marchetti. Correlating cell shape and cellular stress in motile confluent tissues. *Proceedings of the National Academy of Sciences of the United States of America*, page 201705921, nov 2017.
- [156] Xingbo Yang and M. Cristina Marchetti. Hydrodynamics of Turning Flocks. page 5, October 2014.
- [157] Steven M Zehnder, Melanie Suaris, Madisonclaire M Bellaire, and Thomas E Angelini. Cell Volume Fluctuations in MDCK Monolayers. *Biophysical journal*, 108(2):247–50, January 2015.
- [158] Steven M. Zehnder, Marina K. Wiatt, Juan M. Uruena, Alison C. Dunn, W. Gregory Sawyer, and Thomas E. Angelini. Multicellular density fluctuations in epithelial monolayers. *Physical Review E*, 92(3):032729, sep 2015.
- [159] Feifan Zhou, Da Xing, Shengnan Wu, Wei R Chen, Lei Liu, and Wei R. Chen. Intravital imaging of tumor apoptosis with FRET probes during tumor therapy. *Molecular imaging and biology : MIB : the official publication of the Academy of Molecular Imaging*, 12(1):63–70, 2010.
- [160] Falko Ziebert, Sumanth Swaminathan, and Igor S Aranson. Model for self-polarization and motility of keratocyte fragments. *Journal of the Royal Society, Interface*, 9(70):1084–92, may 2012.

Michael D Czajkowski

Personal Data

ADDRESS: 241 Physics Building, Syracuse, NY 13244

EMAIL: chigantic@gmail.com

WEBSITE: mdczajko.expressions.syr.edu

Work Experience

AUG 2014 - AUG 2018	RESEARCH ASSISTANT for M. Lisa Manning & M. Cristina Marchetti Syracuse University <i>Soft and Active Matter: theory and simulation of confluent tissue dynamics</i>
JAN - JUNE 2014	RESEARCH ASSISTANT for John W Laiho Syracuse University <i>Theoretical High-Energy Physics: MC simulations of Lattice Quantum Gravity</i>
SUMMER 2014	Instructor for <i>PHY 663: Graduate Problem Solving</i> at SYRACUSE UNIVERSITY
FALL 2012 - SPRING 2014	Teaching Assistant for <i>PHY 212: General Physics II</i> at SYRACUSE UNIVERSITY
SUMMER 2013	Instructor for <i>PHY 212: General Physics II</i> at SYRACUSE UNIVERSITY

Education

AUGUST 2012 - *Present* | Doctoral program in PHYSICS, **Syracuse University**
Focus: Theoretical Physics & Phenomenology
GPA: 3.65/4.0 — 58 completed credit-hours

DECEMBER 2011 | Bachelor of Arts in PHYSICS with Minor in MATHEMATICS
SUNY Geneseo
Graduated as Dean's list full-time student
MAJOR GPA: 3.28/4.0

JUNE 2007 | High-School Regents Diploma
City Honors School at Fosdick-Masten Park, Buffalo, NY